2013

THE PHARMACOKINETICS OF METAL-BASED ENGINEERED NANOMATERIALS, FOCUSING ON THE BLOOD-BRAIN BARRIER

Mo Dan
University of Kentucky, danmo555@gmail.com

STUDENT AGREEMENT:

I represent that my thesis or dissertation and abstract are my original work. Proper attribution has been given to all outside sources. I understand that I am solely responsible for obtaining any needed copyright permissions. I have obtained and attached hereto needed written permission statements(s) from the owner(s) of each third-party copyrighted matter to be included in my work, allowing electronic distribution (if such use is not permitted by the fair use doctrine).

I hereby grant to The University of Kentucky and its agents the non-exclusive license to archive and make accessible my work in whole or in part in all forms of media, now or hereafter known. I agree that the document mentioned above may be made available immediately for worldwide access unless a preapproved embargo applies.

I retain all other ownership rights to the copyright of my work. I also retain the right to use in future works (such as articles or books) all or part of my work. I understand that I am free to register the copyright to my work.

REVIEW, APPROVAL AND ACCEPTANCE

The document mentioned above has been reviewed and accepted by the student's advisor, on behalf of the advisory committee, and by the Director of Graduate Studies (DGS), on behalf of the program; we verify that this is the final, approved version of the student's dissertation including all changes required by the advisory committee. The undersigned agree to abide by the statements above.

Mo Dan, Student

Dr. Robert A. Yokel, Major Professor

Dr. Jim Pauly, Director of Graduate Studies

THE PHARMACOKINETICS OF METAL-BASED ENGINEERED NANOMATERIALS, FOCUSING ON THE BLOOD-BRAIN BARRIER

DISSERTATION

A dissertation submitted in partial fulfillment of the requirements for the degree of Doctor of Philosophy in the College of Pharmacy at the University of Kentucky

By
Mo Dan

Lexington, Kentucky

Director: Dr. Robert A. Yokel, Provost Distinguished Service Professor in The Department of Pharmaceutical Sciences, University of Kentucky
Lexington, Kentucky

2013

ABSTRACT OF DISSERTATION

THE PHARMACOKINETICS OF METAL-BASED ENGINEERED NANOMATERIALS, FOCUSING ON THE BLOOD-BRAIN BARRIER

Metal-based engineered nanomaterials (ENMs) have potential to revolutionize diagnosis, drug delivery and manufactured products, leading to greater human ENM exposure. It is crucial to understand ENM pharmacokinetics and their association with biological barriers such as the blood-brain barrier (BBB). Physicochemical parameters such as size and surface modification of ENMs play an important role in ENM fate, including their brain association. Multifunctional ENMs showed advantages across the highly regulated BBB. There are limited reports on ENM distribution among the blood in the brain vasculature, the BBB, and brain parenchyma.

In this study, ceria ENM was used to study the effect of size on its pharmacokinetics. Four sizes of ceria ENMs were studied. Five nm ceria showed a longer half-life in the blood and higher brain association compared with other sizes and 15 and 30 nm ceria had a higher blood cell association than 5 or 55 nm ceria. Because of the long circulation and high brain association of 5 nm ceria compared with other sizes, its distribution between the BBB and brain parenchyma was studied. The *in situ* brain perfusion technique showed 5 nm ceria (99%) on the luminal surface of the BBB rather than the brain parenchyma.

For biomedical applications in the central nervous system (CNS), it is vital to develop stable and biocompatible ENMs and enhance their uptake by taking advantage of their unique properties. Cross-linked nanoassemblies entrapping iron oxide nanoparticles (CNA-IONPs) showed controlled particle size in biological conditions and less toxicity in comparison to Citrate-IONPs. CNA-IONPs considerably enhanced MRI T2 relaxivities and generated heat at mild hyperthermic temperatures (40 ~ 42°C) in the presence of alternating magnetic field (AMF). Numerous researchers showed mild whole body hyperthermia can increase BBB permeability for potential brain therapeutic application. Compared to conventional hyperthermia, AMF-induced hyperthermia increased BBB permeability with a shorter duration of hyperthermia and lower temperature, providing the potential to enhance IONP flux across the BBB with reduced toxicity.

Overall, ENMs with optimized physicochemical properties can enhance their flux across the BBB into the brain with desirable pharmacokinetics, which provide great potential for diagnosis and therapy in the CNS.

KEYWORDS: Metal-based engineered nanomaterials (ENMs), blood-brain barrier (BBB), ceria ENM, iron oxide nanoparticles, pharmacokinetics

Mo Dan

Author's signature

06/14/2013

Date

THE PHARMACOKINETICS OF METAL-BASED ENGINEERED NANOMATERIALS, FOCUSING ON THE BLOOD-BRAIN BARRIER

By

Mo Dan

Robert A. Yokel, Ph.D.

Director of Dissertation

Jim Pauly, Ph.D.

Director of Graduate Studies

06/14/2013

Date

To my parents, who always encouraged me to be and do my best. Your constant support and encouragement made the difference. I love you both.

ACKNOWLEDGEMENTS

This dissertation benefited greatly from the input and guidance of a number of people. I would like to start my acknowledgements to where it all began with, my master's degree mentor, Dr. Wei Jia. During the two and half years I was in his lab, I truly realized my passion for exploring the unknown world. I was very well trained in his lab on how to do scientific research at the very beginning of my professional career. I learned how to search the literature in his lab and wrote my very first two manuscripts in English and published them on well-recognized journals. I have to say it was a painful process to write the first draft and went through so many revisions before they published. But all these experiences made me a stronger person and helped me find the right path of my research during my PhD training. He also encouraged me to pursue a PhD in the USA. I still remember that the first time I met him with the other three colleagues on 2005. He told me "it will be one of the best experiences in your life to study abroad in the USA". After 8 years, I know it will be one of the best memories in my life.

I would like to thank my doctoral committee for their input and support throughout my dissertation process. I met Dr. Xianglin Shi on my first day of orientation at The Graduate Center for Toxicology and I felt so nervous because I cannot even speak one sentence properly in English. Dr. Shi is such a nice person and told me I can contact him anytime if I need any help. One year later, he became one of my committee members. He has years of research experience on metals. I am doing research on metal-based nanomedicine and Dr Shi gave me suggestions on my research and provided different perspectives during the past four years. Dr. Linda Dwoskin is the only neuroscientist in

my committee. She provided valuable suggestions on the blood brain barrier association of nanoparticles. She is also a role model for all the female PhD students. Even though she is so busy with her research and administration, she is always willing to take time to help me with my research. On 2011, I became a CNTC trainee and I changed my research to cancer therapy using iron oxide nanoparticles. My research would not have been possible without Dr Bae's patience and support. I could not count how many times I stopped by his office to ask questions about my research and he taught me how to use the Zetasizer and asked his postdoc to help me with nanoparticle synthesis. We also wrote a paper together. He was extremely patient to teach me how to organize a paper and describe my data in a better way.

I remembered the first time I talked with Dr. Robert Yokel on 2008 to express my interest to do a lab rotation and potential to join the lab. Our conversation is short and dry because I cannot express myself very well in English at that time. But he still welcomed me with his open arms. After the rotation, I decided to join Dr. Yokel's group because I love the ceria nanoparticles project and working environment. I did not realize it is the best thing happened to me in USA at that time. Dr. Yokel has provided me with great guidance during this journey, quietly nudging me along the right path while providing me with the freedom to go my own way. I am able to poke my head in his office anytime for anything. He encouraged me every time I lost my confidence about my research. I still remembered he took a lead pipe from an old church to teach us heavy metal toxicity in class; he taught me carotid artery cannulation in rats; he set up a 'magic' shaker for my ceria nanoparticle infusion; he made a 37 degree chamber for my hyperthermia study

using a plastic box! I probably can write another dissertation to talk about all the stories between Dr. Yokel and me during the past five years. Dr. Yokel's concern always extended beyond my work in the lab. He is a great mentor and friend throughout this process. He taught me to become a better person, which means more than I can express.

Beyond my committee, so many other people in the National Cancer Institute-Cancer Nanotechnology Training Center support me from 2011. Dr. Tom Dziubla is my co-mentor in the CNTC. Our collaborations have expanded my knowledge and led me to new fields. He has been a great resource for my troubleshooting and was always more than willing to help me when I needed it. My clinical mentor, Dr. Thomas Pittman showed me how to do brain surgery on a human. Dr. Peter Hardy helped me to expend my research to *in vivo* diagnosis using MRI and taught me basic concepts and small animal MRI. Dr. J. Zach Hilt helped me to synthesize my very first batch of iron oxide nanoparticles and shared his years of research experiences on iron oxide nanoparticles and hyperthermia. Dr. John Villano gave me great ideas on brain tumor research from a clinical perspective and was always willing to help me when I needed it. Dr. Brad Anderson challenged my thinking and inspired me to become a better scientist.

The work presented here would not have been possible without the assistance of our collaborators. To chemists Dr. Peng Wu and Dr. Eric Grulke, thanks for the ceria ENMs I used in my study and your help on charactering them. To analytical chemist Dr. Jason Unrine, thanks for analyzing all the samples by ICPMS for me. To histopathologist Dr. Michael Tseng, thank you for all the TEM data you generated for us, which helped us to

understand our results better. To Dr. Robert Macphail, thank you for inspiring me with your passion for science.

I would like to extend a heartfelt thank you to the entire staff at the College of Pharmacy. Tonya Vance, Dimple Hatfield, Todd Sizemore, and Lou Dunn are so helpful every time I needed your help. Special thanks to Catina Rossoll for taking care of all of the little things in the past five years! You are the best!

I would also like to thank all the students and postdocs I have had the opportunity to work with. Dr. Matthew Dickerson and Dr. Daniel Scott provided the nanoparticles I need for my *in vitro* and *in vivo* studies. Rob Wydra helped me to synthesize iron oxide nanoparticles. My collaboration with David Cochran was so enjoyable and fruitful. Dr. Christin Hollis is willing to help me anytime I have questions about my research or any problems I have in my lab. Graduate students in Dr Leggas lab, Dr. Kuei-Ling Kuo, Dr. Eleftheria Tsakalozou and Dr. Tamer Ahmed, taught me everything about cell culture and shared lab space with me and treated me as one of your own. You mean more than you may ever know.

Last but certainly not least, I would like to thank my parents for their love and support. You taught me that I could achieve anything in life if I work hard. You encouraged me to dream big and supported every decision I made. You shared your experiences with me and taught me to become a good person. I always remember you told me "you don't need to be rich or successful. But you should become a useful person." I would never have

made it to this point if I don't have the belief in my mind to become a useful person. I love you. Thank you all!

TABLE OF CONTENTS

LIST OF TABLES

LIST OF FIGURES

Chapter 1 Introduction and Objectives

1.1. Introduction and Statement of the Problem

Rapid expansion of nanotechnology has allowed metal-based engineered nanomaterials (ENMs) to be used with broad application. These applications include drug delivery devices (1), imaging agents (2), catalysts (3) and sensors (4). Metal-based ENMs are very attractive for academia and industry, because of the dramatic increase in human exposure and unusual physicochemical properties such as their size and shape-dependent optoelectronic properties (5). Little is known about metal-based ENM distribution or persistence in the vascular system and their association with biological barriers such as the highly regulated blood-brain barrier (BBB).

Previous studies reported that the blood and biological distribution of metal-based ENMs was size-dependent. For example, after iv injection of gold ENMs (15, 50, 100 and 200 nm), 15 and 50 nm showed higher concentration in the blood and the most widespread organ distribution, including the brain compared with the other sizes 24 hours after injection (6). Our previous research showed that the blood cerium concentration was 0.56 and 1.3 mg/L after a 1 h infusion of 50 or 250 mg/kg of an ~ 30-nm commercial ceria ENM to rats (7). In contrast, 1 h after infusion of 100 mg/kg of an in-house manufactured 5-nm ceria ENM it was 370 mg/L (8), suggesting that the rate of metal oxide ENM clearance from blood was size dependent. However, little is known about the influence of size on the distribution in, and clearance from, blood of metal-based ENMs.

To investigate the persistence and distribution of a model ENM in blood, we utilized ceria (CeO_2, ceric oxide). Numerous studies reported ceria ENM to be neuro- and cardioprotective, suggesting it has therapeutic utility in medical disorders caused by reactive oxygen species (9-17). On the other hand, there are reports of ceria-induced toxicity (toxicity: a cascade of events starting with exposure, proceeding through distribution and metabolism and ending with interaction with cellular macromolecules and the expression of a toxic end point (18)) associated with increased oxidative stress (19-24). Nanoscale ceria is a catalyst, marketed as a diesel fuel additive in the Eolys® system (25). There have been limited studies of the biodistribution of nanoscale ceria (26, 27). Despite what has been done previously, there is a lack of knowledge of the pharmacokinetics of ceria ENMs in blood other than our report that a commercial ~ 30-nm ceria had an initial $t_{½}$ of ~ 0.125 h (7). It is vitally important to understand the pharmacokinetics of ENMs in relation to their potential therapeutic applications and/or toxicity.

How ENMs interact with living tissues, particularly biological barriers including the BBB, after they distribute in the blood will determine their distribution and potential applications in the central nervous system (CNS). The tightly regulated BBB plays a crucial role in safeguarding the brain from endogenous and exogenous compounds circulating in the blood (28). ENMs are being extensively investigated as an approach to deliver drugs to the CNS based on their unique physicochemical properties, such as tight junction disruption, increased retention at the brain capillaries combined with adsorption to the capillary walls and receptor mediated transcytosis (29, 30). Several studies

indicated that metal ENMs altered BBB integrity and increased ENM brain accumulation (6, 7, 31). After oral gavage, 25 nm ceria appeared in the brain 1 day later and was still present in the brain at day 7 (32). Although these studies indicated that some metal oxide ENMs have the potential to cross the BBB, most studies on brain ENM uptake did not separate the capillary endothelial cells from the brain cells, making it difficult to determine whether the ENMs entered the brain or if their distribution was limited to the capillary endothelial cells and blood in the brain vasculature. For drug delivery into the brain, the capability of ENMs across the BBB into the brain will determine whether they can increase the drug in specific brain tissues such as brain tumor. Meanwhile, a better understanding of non-brain targeting ENMs in the BBB and the brain tissue will provide crucial information for their potential side effects in the CNS. In general, for toxicological consideration or biomedical application in the CNS, it is important to understand the distribution of ENMs between the BBB and/or brain tissue.

After studying the pharmacokinetics in blood and interaction with the BBB of ceria ENMs, multifunctional ENMs with desirable physicochemical and pharmacokinetic properties were developed and investigated for potential biomedical application in the CNS. Iron oxide nanoparticles (IONPs) have drawn increasing attention as magnetic resonance imaging (MRI) contrast agents to evaluate blood-brain barrier dysfunction related to tumors and other pathologies in the CNS (e.g. brain tumor, stroke, and carotid atherosclerosis) in clinical and preclinical studies (33, 34). IONPs can also be used as a heating source for hyperthermia as they generate heat in the presence of an alternating magnetic field (AMF: a varying magnetic field. In an AMF, induced currents are

generated in IONPs and as a consequence, heat is generated in the metal (35)) to increase temperature in solutions or localized tissues, thereby killing cancer cells in a controlled manner (36-38). A problem with most metal-based ENMs including IONPs is their tendency to agglomerate in aqueous solutions unless their surface is properly modified, resulting in plasma protein binding *in vivo* and rapid clearance by the mononuclear phagocyte system (MPS) (39). Several studies showed that IONPs, either bare or surface-modified, could cause cell toxicity and oxidative stress *in vitro* and *in vivo* (40-42). Therefore, it is crucial to improve particle stability and biocompatibility of IONPs in biological environments.

In order to prevent agglomeration of IONPs, citric acid and surfactants are frequently used to stabilize IONPs in aqueous solutions (43-45), but these stabilizers often cause problems. For example, our previous study on citric acid-coated-ceria showed that agglomerated ENMs were cleared into and persisted in the MPS, which could potentially cause toxic effects over time (8, 27). Other research on citric acid IONPs demonstrated similar results (46, 47). Biocompatible polymer nanoparticles and water soluble polymers have been used as less toxic and more stable alternatives to these stabilizers (35, 48). Among these polymer-based formulations, polymeric micelles prepared from amphiphilic block copolymers are an attractive choice to develop IONP formulations for cancer imaging and hyperthermia (49, 50). Micelles can embed IONPs and achieve considerable MRI contrast enhancement as a result of the collective effects of IONP clusters (51-53). One of the critical problems associated with conventional polymeric micelles is particle stability, particularly in dilute conditions (e.g. blood and other biological environments)

as polymer micelles can dissociate below the critical micelle concentration (54). To solve these problems, cross-linked nanoassemblies (CNAs) from biocompatible poly(ethylene glycol)-poly(aspartate) [PEG-p(Asp)] block copolymers were used in my study, which have the potential to provide stable nanoparticles that can entrap charged, hydrophobic, and amphiphilic payloads without changing particle sizes optimized for accumulation in certain tissues such as the CNS (55-57).

For CNS application of IONPs, it is important to increase their flux across the BBB and brain entry. Numerous researchers have shown mild whole body hyperthermia can increase BBB permeability, which has potential for therapeutic application in the brain (58). Whole body hyperthermia (42 ºC for 0.5 h) significantly increased adriamycin flux delivered in a temperature sensitive liposome across the BBB *in vitro* and *in vivo* (59). However, whole body hyperthermia led to heat stress *in vivo* and caused toxicity to the CNS such as edema (58, 60). CNA-IONPs provide the potential to serve as a stable and biocompatible IONP delivery system to generate local hyperthermia to increase BBB permeability and brain accumulation for diagnosis and therapy.

1.2. Objectives

The overall objective of this dissertation was to gain a better understanding of the influence of size on the distribution in and clearance from blood of metal-based ENMs, interaction between metal-based ENMs and the BBB and develop a stable and biocompatible magnetic ENM for the controlled delivery of heat to enhance BBB flux of

ENMs. Four projects were involved in this dissertation and the hypotheses of each project are described as follows:

1. "Ceria engineered nanomaterial distribution in and clearance from blood: Size matters"

   Hypotheses:

   a. The fate of a metal oxide ENM in blood is different than its constituent metal
   b. ENM size influences its persistence in and distribution within the major components of blood.

   The cerium ion and four sizes of cubic or polyhedral citrate-coated ceria ENMs will be iv infused into rats. Blood will be repeatedly withdrawn up to 4 h later, and in some cases up to 30 days. An aliquot of each blood sample drawn up to 4 h after ceria infusion will be allowed to clot. By comparison of cerium in whole blood, serum, and the clot we could determine pharmacokinetic parameters of ceria distribution in and clearance from blood. This study informs about the effects of ceria ENM size on distribution and clearance from blood, which cannot be predicted from the cerium ion and size plays an important role on pharmacokinetics and cell associations.

2. " Brain microvascular endothelial cell association and distribution of a 5 nm ceria engineered nanomaterial"

   Hypothesis:

   c. A 5 nm ceria ENM can associate with brain capillary cells and enter the brain.

The *in situ* brain perfusion method will be used to evaluate BBB integrity and determine brain entry rate at different perfusion flow rates, ceria ENM concentrations and perfusion durations. Eight brain regions and a choroid plexus will be collected to test regional differences in BBB integrity and ceria ENM brain entry rate. The capillary depletion method will be used to evaluate ceria ENM distribution between capillary and brain tissues. Light and electron microscopy (LM and EM) will be employed to investigate the localization of ceria nanoparticles. This research will provide the first data on the kinetics of ceria nanoparticle interaction with the BBB and choroid plexus. This information will be important for the design of ceria ENMs as a therapeutic agent as well as for a comprehensive toxicology assessment.

3. "Block copolymer cross-linked nanoassemblies improve particle stability and biocompatibility of superparamagnetic iron oxide nanoparticles"

   Hypothesis:

   d. CNAs containing carboxyl groups in the core would simultaneously create, entrap, and protect IONPs as iron ions (Fe^{2+} and Fe^{3+}) co-precipitate inside the nanoassembly core, thus suppressing IONP agglomeration and improve the biocompatibility of IONPs without losing their superparamagnetic properties.

CNA-IONPs will be developed using the co-participation method. Particle stability and biocompatibility will be determined with or without AMF exposure at room, body, and hyperthermic temperatures. Cytotoxicity of the particles will be investigated using

brain endothelial-derived cells. To evaluate potential imaging applications, T2-weighted MRI enhancement of CNA-IONPs and AMF-induced heating properties of CNA-IONPs will be evaluated. CNAs with a cross-linked anionic core have potential to improve particle stability and biocompatibility of IONPs, which would be beneficial for future MRI and AMF-induced remote hyperthermia applications.

4. "Alternating magnetic field enhanced the blood brain barrier association and paracellular flux of superparamagnetic iron oxide nanoparticles"

   Hypothesis:

   e. AMF-induced hyperthermia would significantly increase the paracellular and/or transcellular flux of IONPs, and influence the BBB cell association with IONPs compared with conventional hyperthermia.

CNA-IONP uptake flux across the BBB, and effects will be evaluated in *in vitro* BBB models at body temperature, conventional hyperthermia, or AMF-induced hyperthermia. The paracellular flux changes induced by conventional hyperthermia or AMF-induced hyperthermia will be monitored by Lucifer yellow (LY), a paracellular flux maker. Using transmission electron microscopy (TEM), the cellular localization of the iron oxide core of the studied nanoparticles will be investigated. Results of this study will provide a better understanding how AMF-induced hyperthermia influences IONP BBB cell association and flux across the BBB, which will be beneficial for IONP future application for the CNS and insight into the difference between conventional hyperthermia and AMF-induced hyperthermia on the BBB permeability and IONP flux.

This dissertation starts with an introduction and objectives in Chapter 1. Chapter 2 contains background on metal-based ENMs, which includes an introduction to metal-based ENMs, a discussion on how their physicochemical properties influence the pharmacokinetics and the BBB association of ENMs, and a review of previous work on ceria and iron oxide ENMs on pharmacokinetics and the BBB association and their problems. Chapters 3, 4, 5 and 6 present the results and discussion for each project described above. Finally the conclusions and future studies are presented in Chapter 7.

Chapter 2 Background

2.1. Metal-based engineered nanomaterials and their biomedical applications

Engineered nanomaterials are normally defined as being smaller than 100 nm on one external dimension or internal structure (62). However defining the size of ENMs is debatable. An ENM has typically been referred as any particle less than 1 μm. Such a small size gives the ENM an unusual surface area, size distribution, surface modification (surface groups, inorganic or organic coatings, surface charge etc.), solubility, shape, and potential aggregation compared to bulk material. The unique physicochemical properties of ENMs provide great potential for biomedical applications.

The application of ENMs is a burgeoning field with immense biomedical potential. In 2006, a global survey on biomedical application of ENMs was conducted by the European Science and Technology Observatory. This survey found that more than 150 companies were developing nanoscale therapeutics; and 24 nanotechnology-based therapeutic products were already approved for clinical use with sales exceeding $5.4 billion (62). Biomedical nanotechnology sales were expected to grow to $70-160 billion by 2015 worldwide (63). Most metal-based ENMs have unique physical properties which can be dictated for certain biomedical applications, giving them a strong potential for diagnosis and therapy. For example, the optical properties of gold nanorods are directly related with their shape and aspect ratio, which were used for contrast imaging and photothermal therapy (64).

Although the concept of metal-based ENMs was introduced in recent years, humans started to synthesize and use metal nanoparticles hundreds of years ago. Gold nanoparticles were used as part of ancient ayurvedic medicine in India 2000 years ago (65). Although previously used, the first scientific study on metal nanoparticles has been credited to English physicist and chemist Michael Faraday in 1857. Faraday studied and reported the size dependent optical properties of gold colloids (66). The application of metal-based ENMs has expanded in recent years as a result of significant developments in the synthesis process. It has become possible to design and engineer metal-based ENMs to produce specific and desired properties for different applications. I summarized the major novel biomedical applications below.

2.1.1 Photothermal therapy

Photothermal therapy has been actively investigated to localize cancer treatment, with promising potential to minimize damage to non-cancerous tissue. Metal-based ENMs can be "tuned" to serve as either strong absorbers or scatters of near-infrared light, which enables their use for photothermal therapy. Gold nanoshells have been extensively studied for this application (67). For example, the therapeutic efficacy of photothermal therapy induced by gold nanoshells was tested in mouse tumors. The gold nanoshell was delivered via tail veil injection and the tumors were irradiated with near infrared (NIR) lasers at 808 nm wavelength at a power of 4 W/cm^2 for 3 min. Several weeks after treatment, all mice in the treatment group were free of tumors. Meanwhile, they also showed that the gold nanoshell showed dramatic contrast enhancement for optical coherence tomography (OCT) imaging (68). Through this study gold nanoshells

demonstrated their effectiveness in imaging and ablating tumors *in vivo*. This could allow integration of gold nanoshells into diagnostic and therapeutic technologies.

2.1.2. Radiotherapy

Metal-based ENMs provide an advantage in radiotherapy because of their optical properties, surface resonance and wavelength tunability. Gold ENMs are the most studied metal-based ENMs for use in radiotherapy. The intrinsic radioactive properties of gold (Au-198 and Au-199) ENMs can be tuned, which make them ideal candidates for radiotherapy (69). Dose and size dependent cytotoxicity of silver and gold ENMs were demonstrated on glioma cells in combination with radiation. And 20 nm silver ENMs and 50 nm gold ENMs showed the most effective radiosensitization at low radiation doses compared with other sizes (70). A recent report studied the radiosensitization application of gold ENMs using a size range of 14-74 nm. They demonstrated that both the size and the amount of uptake of ENMs into cells affect radiosensitization. Their results also showed that 50 nm gold ENMs displayed the utmost enhancement compared to 14 and 74 nm (71). For radiotherapy application, it will be critical to develop ENMs with the desirable size to enhance their radiosensitization ability.

2.1.3. Imaging

Their optical, magnetic, and other properties have made metal-based ENMs very attractive for imaging. Numerous studies have demonstrated that gold ENMs are excellent contrast agents. This is due to the fact that the intensity of absorption and scattering of gold ENMs is significantly higher than most organic dyes (72). The

applications of gold ENMs for *in vivo* imaging can be summarized as: 1) Optical coherence tomography; 2) Two-photon luminescence; 3) Photoacoustic tomography; 4) Surface enhanced Raman scattering; 5) X-ray computed tomography imaging. The details about these five applications were reviewed in 2011(73). Another most investigated and widely used metal-based ENM for MR imaging is IONP, due to their unique magnetic properties. More detail about this application will be reviewed and discussed in 2.5.

2.1.4. Drug delivery

The unique properties of metal-based ENMs have allowed for various controlled delivery systems to be developed such as pulsed laser induced gold-thiol bond cleavage (74) and hyperthermia-triggered release (75). Multifunctional metal-based ENMs were also developed for combination treatment, such as hyperthermia plus chemotherapy or theranostics, by combining drug delivery and imaging (73). For example, tumor necrosis factor alpha (TNF-α) can covalently conjugate to gold ENMs resulting in the combination of TNF-α and gold-induced hyperthermia. This combination of TNF-α therapy with gold hyperthermia resulted in an increase in tumor recession (76). Thermally crosslinked IONPs have been developed for use in drug delivery and MR imaging. The polymeric shell of IONPs loaded with doxorubicin was efficient in detecting Lewis lung carcinoma, and delivering sufficient drug to tumor tissues with lower toxicity in other organs (77). These studies demonstrated that metal-based ENMs can be incorporated in drug delivery systems, which provide the possibility to control drug release and increase efficacy of nanomedicine by combining different therapeutic strategies.

2.2. Effect of size and surface modification on pharmacokinetics of metal-based engineered nanomaterials

There have been several physicochemical candidates identified that influence the pharmacokinetics of ENMs such as chemical nature, size, shape, surface chemistry, charge, presence of surface lattice defects, surface curvature, and the atomic arrangement of the crystalline facets and agglomeration potential (78-80). ENM size plays a very important role in the pharmacokinetics because of their effects on margination dynamics (lateral drifting from the vessel core to the walls), vascular adhesion, protein corona (protein coating) and escape routes from the vasculature (81). In this section, how size influences the pharmacokinetics of metal-based ENMs will be summarized.

Different margination dynamics are desirable for different ENM applications. For tissue targeting ENMs, the fast margination and interaction with the endothelium may be needed to target with selective cells with a high adherence. On the other hand, low margination leads to long circulation without being trapped by cells. Mathematical modeling and experiments *in vitro* demonstrated that certain ENMs within the critical size showed the maximum margination time (82). For different applications, ENMs should have size at the certain critical size range in order to circulate in the blood stream and/or interact with the endothelium cells (83). Adhesion was also studied *in vitro* using different sizes of silica ENMs. The strength of adhesion of the spherical ENMs reduces as their diameter increases (84). Despite these important findings, it is more than likely these previous mathematical modeling and experiments *in vitro* have oversimplified the

vasculature architecture *in vivo*. More studies are needed to define how different sizes of ENMs change their interaction with the vasculature *in vivo*.

It has been shown that different ENMs influence their interactions with proteins in blood both quantitatively and qualitatively. For example, the protein corona changes the half-life and biodistribution of ENMs (82, 85, 86). ENM aggregation was induced by the proteins in blood, which can be trapped in the first capillary bed encountered, such as rat or mouse lung following tail vein injection (82). Furthermore, the protein corona on the surface of ENMs also facilitated recognition and clearance from the blood by circulating phagocytes and macrophages in the hepatic Kupffer cells and the marginal zone and red-pulp macrophages in the spleen (87, 88). A previous study has shown that the size of ENMs changed the protein corona, which influence the ENM's pharmacokinetics in the blood (85).

Normally, ENMs leave blood circulation through opening fenestrations in the organs or some disease conditions such as tumor (89). In the liver, the size of fenestrate can be as large as 150 nm (90). Spleen filtration is also size dependent. ENMs need to be small enough to avoid the splenic filtration process at intercellular slits in the walls of venous sinuses (91). The width of interendothelial cell slits is approximately 200-250 nm, providing a mechanism to target the spleen (92). Alternatively, the size of longer-circulating ENMs should not exceed 200 nm to bypass spleen filtration. Studies have shown that tumors have a characteristic leaky vasculature pore size of 200 nm to 1.2 μm (93). However, the average size recommended for tumor targeting is less than 200 nm to

take advantage of the enhanced permeability and retention (EPR) effect (94, 95). This doesn't mean that the smaller ENMs will have desirable pharmacokinetics. ENMs less than 10 nm can leave the blood circulation through the permeable vascular endothelium in lymph nodes (96, 97). Furthermore, very small ENMs tend to be cleared by glomerular filtration very fast. Quantum dots were used to define the renal filtration threshold in rodents. They showed that when the diameter is less than 5.5 nm, the ENMs were cleared through urinary excretion rapidly (98). In order to target specific tissue or change the ENM's clearance pathway, it is critical to design ENMs with desirable sizes.

Another factor that influences the rate of ENM clearance from blood and their distribution is their surface chemistry, including charge and surface coating. A zeta potential greater than + 30 or less than -30 mV decreases the potential for agglomeration in the medium due to repulsive electrostatic forces (99). ENMs are often coated with polymers such as polyethylene glycol or oxygen-rich ions such as citrate. These coatings increase ENM hydrophilicity and stabilize ENM dispersions through the electrostatic repulsion mechanism, which may reduce their clearance by the reticuloendothelial system (100-103). Citrate, an endogenous molecule present in the blood and an integral component of the tricarboxylic acid cycle, is one of the most commonly used surface coatings to minimize agglomeration. Although citric acid forms a stable chelate with ENMs, it is not sufficient to prevent agglomeration and precipitation in the presence of multivalent counter ions (magnesium or calcium) and serum proteins (104-107). Biocompatible polymer ENMs and water soluble polymers have been used as less toxic

and more stable alternatives to these stabilizers (48, 108). More detail about biocompatible polymer stabilizers will be discussed in 2.3.3.2.

2.3. Effect of physicochemical properties of engineered nanomaterials on their blood-brain barrier association

2.3.1. The blood-brain barrier and the translocation mechanisms to the brain

The microenvironment of the brain is tightly regulated by the BBB. It relies on brain endothelial cells, pericytes, astrocytes and neurons to generate and maintain the unique barrier properties regulating cerebral blood flow and barrier performance. Selected molecules pass the BBB from the bloodstream to the brain by either the passive diffusion pathway or a specific transporter pathway. Lipid-soluble agents and small gaseous molecules enter into the brain through the effective transcellular passive diffusion pathway, but not the paracellular pathway because of the tight junctions between the endothelial cells (109). Carrier-mediated transport systems facilitate transport of nutrients into the brain including glucose, galactose, amino acid, nucleosides, purines, monocarboxylate, choline, vitamins and hormones (29). Glucose transporters (such as GLUT1 and GLUT3) provide the major energy source, glucose, for the brain. Monocarboxylate transporters (MCTs) are responsible for the transport of monocarboxylates (lactate, pyruvate, acetoacetate). MCTs are of great significance for brain energy metabolism (110). Receptor-mediated transport systems can facilitate endogenous proteins and hormones to cross the BBB. The transporters for insulin, insulin-like growth factors, angiotensin II, and transferrin (Tf) have been identified (111, 112). However, under normal physiological conditions, the presence of interendothelial

tight junctions and absence of a vesicular transport system restrict the entry of proteins, ions, lipid insoluble non-electrolytes and circulating hematogenous cells into the brain (113, 114). ATP-binding cassette (ABC) transporters, efflux transporters, are found at the luminal membrane of the brain endothelium. The multidrug resistance transporter P-glycoprotein (P-gp or ABCB1) is an ATP-dependent efflux pump which mediates rapid removal of ingested toxic lipophilic metabolites, such as many amphipatic cationic drugs (115). Other efflux transporters (ASCT2, NET, OAT3) have the potential to work together to reduce penetration of xenobiotics into the brain and increase their efflux from the brain (116). In general, the BBB has not only a physical barrier but also metabolic mechanisms to eliminate the xenobiotics and maintain brain homeostasis.

2.3.2. Conventional strategies to cross the BBB and their limitations

Because of the insufficient delivery of therapeutics into the brain, aggressive research efforts have focused on the development of new strategies to more effectively deliver drugs to the CNS for decades. The major approaches and their limitations are summarized below (117).

Invasive approaches have been used to mechanically breach the BBB to deliver drug to the brain including: 1) Intra-cerebro-ventricular (ICV) infusion: ICV showed pharmacologic effects if the target of the drug is close to the ventricles (118). 2) Convention-enhanced delivery (CED): a small catheter was inserted into the brain parenchyma and infusate is actively pumped into the brain. CED demonstrated promising results recently on animals. However, it is still challenging to place the catheters

precisely and optimize the infusion parameters for delivery (119). 3) Intra-cerebral injection or implants: the drug concentrations in the brain tissue depend on the diffusion principle. The distribution of drugs in the brain by diffusion decreased exponentially with distance (120). 4) Disruption of the BBB: the tight junctions were disrupted to increase the BBB permeability. Osmotic disruption, MRI-guided ultrasound BBB disruption and whole body hyperthermia are commonly used techniques. Hypertonic mannitol solution was used in the clinic to increase drug concentrations in the brain (121). Ultrasound demonstrated the capability to disrupt the BBB in animal models. Numerous researchers have shown that mild whole body hyperthermia can increase BBB permeability (58). However, these approaches are expensive and lead to potential brain toxicity (58, 60).

Medicinal chemistry approaches have been utilized to modify the physicochemical properties of molecules to increase their BBB permeability. The small molecules to enter the brain should have molecular weight less than 500D, low hydrogen bounding capabilities and hydrophobic properties (122, 123). For example, N-docosahexaenoyl can be conjugated with small molecules to increase their BBB permeability (124). However, structure modification has the potential to reduce, or even lose, the central nervous activities of small molecules. Furthermore, hydrophobic molecules serve as good candidates for the efflux pump P-glycoprotein in the BBB (125).

One promising approach to access the brain is to take advantage of the receptors and transporters on the BBB. As I described in 2.3.1, essential substances such as glucose, insulin and growth hormone can be recognized and transported into the brain using the

receptors or transporters on the BBB. For example, transferrin-conjugated therapeutic agents can cross the BBB using receptor-mediated transcytosis (82). The limitation of this strategy is a lack of full understanding of certain transporters and/or receptor-mediated mechanisms to cross the BBB. For example, the transferrin receptor has been the most studied receptor to target receptor-mediated brain uptake (126). Despite this plethora of research on the transferrin receptor, there has been little work done on brain uptake of transferrin-modified agents, and most of the research was focused on the improvement of diagnostic and therapeutic effects (2, 127). Some studies showed that the brain delivery of the transferrin ligand led to limited transcytosis using a healthy animal model (128). In order to take advantage of transporter and receptor mediated mechanisms, a better understanding of these physiological processes is needed.

2.3.3. Engineered nanomaterial translocation into the brain

ENMs have been shown to have multiple mechanisms to cross the BBB and overcome some of the previous limitations mentioned in the above section. Numerous studies have shown that ENM uptake into the brain can occur through a variety of mechanisms (Figure 2.1). 1) Passive diffusion: ENMs adhered to the endothelial cells of brain capillaries, increased the concentration gradient, then were transported by passive diffusion (129). ENMs also can prolong their circulation time in blood and be recognized by the MPS, increasing the passive targeting capability of ENMs (29). 2) Endothelial cell membrane lipid solubilization: surfactant coated ENMs can increase BBB permeability by solubilizing the endothelial cell membrane lipids (130). 3) Open the tight junctions: ENMs open the tight junctions between the brain capillary endothelial cells, and increase

the penetration into the CNS (30). 4) Receptor-mediated endocytosis: Polyether-copolyester-coated nanoparticles are taken up into the brain via clathrin and caveolin mediated endocytosis mechanisms (131). Transferrin-coated ENMs enter the BBB via the caveolae pathway (132) and clathrin-coated pathway (133). Plasma protein, especially apolipoprotein E (Apo-E), coated nanoparticles are mistaken for low-density lipoprotein (LDL) particles by the cerebral endothelium and internalized by the LDL uptake system (134). 5) Inhibition of efflux systems: ENMs can inhibit the drug efflux system, i.e., Polysorbate-coated nanoparticles modulate P-glycoprotein on the BBB, to increase the ENMs flux across the BBB (135). 6) Absorptive transcytosis: positively-charged ENMs interact with the negatively charged plasma membrane surface through electrostatic interaction (136). Because of the unique physicochemical properties of ENMs, they can potentially cross the BBB by multiple mechanisms. That's why nanoparticles are versatile platforms for drug delivery systems with potential to treat brain diseases. It is very important to understand how different physicochemical properties can affect BBB translocation and brain uptake of ENMs. The previous research on how size and surface modification influence ENMs flux across the BBB is summarized below.

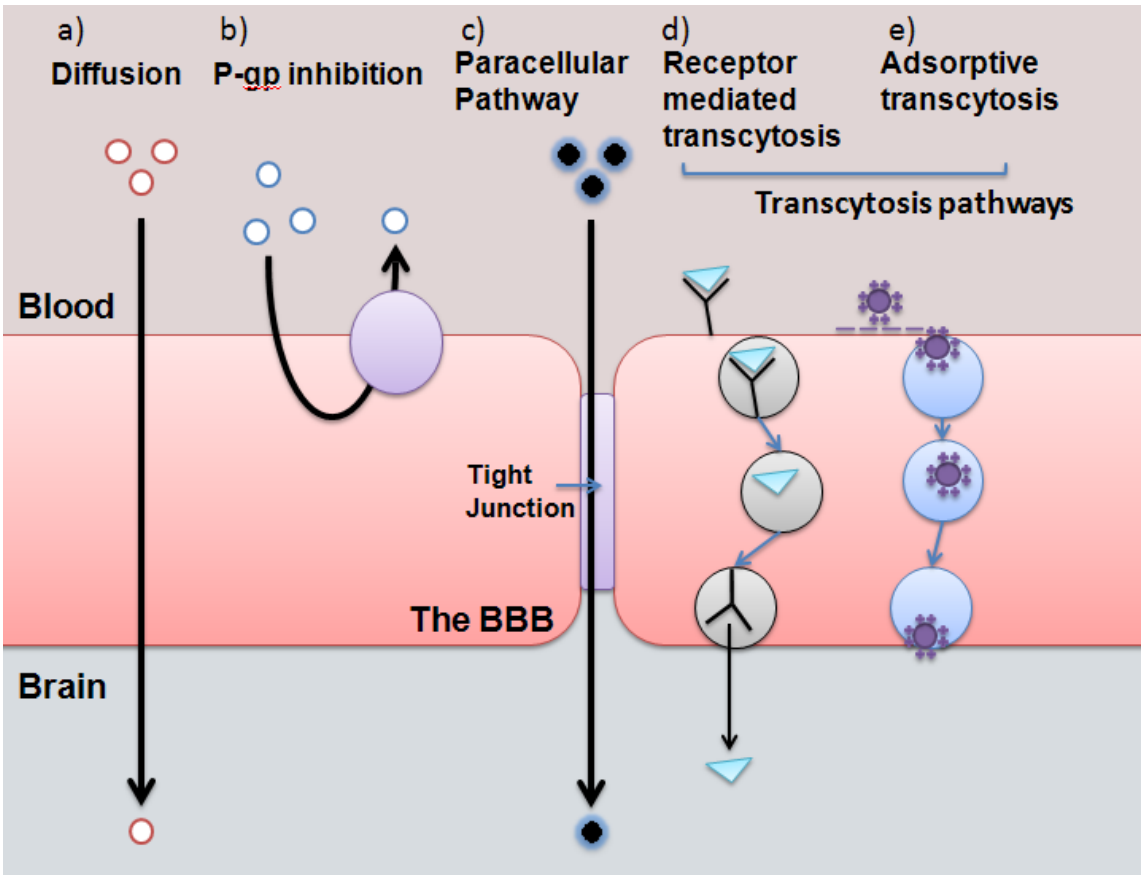

Figure 2.1. A schematic diagram of the main pathways that ENMs have potential to increase the brain uptake of ENMs or drugs. a) ENMs increased passive diffusion by creating a sink condition. b) ENMs inhibit a drug efflux system. c) ENMs open tight junctions. d) ENMs are taken up by receptor-mediated endocytosis and transcytosis. e) Positive charged ENMs are taken up by adsorptive mediated transcytosis. Adapted from (137).

2.3.3.1. Size

The size of ENMs has a profound effect on pharmacokinetics, biodistribution and passive targeting (See Section 2.2.). Tight junctions can block ENMs larger then 4 nm diameter under normal physiological conditions (138). However, except paracellular penetration, endocytosis and transcytosis are important ways to cross the BBB, especially for ENMs. Clathrin and caveolae-mediated endocytosis and adsorptive transcytosis are the main mechanisms for ENM uptake into the BBB (139, 140). Size plays a very important role in

these endocytosis pathways. There are different views on the average size of the endocytic vesicle, 100 nm (141) or 120 nm (142) for clathrin-mediated endocytosis, 50 nm-100 nm (141, 143) or 60 nm-80 nm (142, 144) for caveolae-mediated endocytosis. However, most of this research is focused on fundamental biological processes. The differences between the fundamental biological research and particle uptake research lead to the finding of a difference in optimal size when looking at ENM drug delivery via the endocytosis pathway. Rejman *et al* investigated size-dependent internalization of nanoparticles from 50 nm to 1000 nm. Their results showed that when a diameter was less than 200 nm, clathrin-mediated endocytosis was the dominant pathway. With increasing size, a shift to caveolae-mediated endocytosis was observed, and caveolae-mediated endocytosis became the predominant pathway for 500 nm particles (145). The cell types and their states of differentiation can also determine the choice of pathway (78). Metal-based ENMs have been shown to have the ability to cross the BBB. However, most published studies show indirect evidence of nanoparticle flux across the BBB into the brain by monitoring fluorescent and radioactive drugs (146, 147), or therapeutic efficacy of drugs in animal models of brain tumors (148). A better understanding of nanoparticle association with biological barriers, such as the tightly regulated BBB, and their flux across them, is urgently needed.

Previous research demonstrated that having a optimal particle radius would accelerate wrapping of ENMs and their cell uptake (78). The critical size for ENMs to have properties different from solution and bulk chemistry is ~ 15 to 50 nm. The critical size of ENMs has been studied on cell internalization and their function in biological systems.

Reactive oxygen species (ROS) generation in an acellular system, to which titania ENMs ranging in size from 4 to 195 nm were added, was negligible up to and including 10 nm then increased up to ~ 30 nm when it reached a plateau (149). Gold ENMs with a diameter of 50 nm were taken up by mammalian cells at a rate and concentration that was faster and higher, respectively, than 14, 30, 74, and 100 nm gold ENMs (150). The optimal wrapping of transferrin-coated gold ENMs occurs at about 50 nm and the interaction between the receptor and 50 nm gold ENMs can produce enough free energy to drive the ENMs into the cell (151). It is crucial to design an ENM system within the critical size range for biomedical applications.

Numerous studies have already been done to investigate how crucial the size of metal-based ENMs is to cross cell barriers (150, 152, 153). Size also plays an important role for the translocation of inhaled nanoparticles to the CNS via olfactory neurons (154) and toxicity such as ROS generation (149). However, how size influences the ability of nanoparticles to cross the BBB still hasn't been systematically studied. Even though we could try to predict how size might affect the ability to cross the BBB using results about ENMs, our predictions are limited because the BBB is a tightly regulated special membrane barrier with tight junctions and efflux transporters. More research needs to be done to have a better understanding whether size influences ENM association with the BBB and entry into the brain, not only for drug delivery of ENMs, but also for human risk assessment.

2.3.3.2. Surface modification

Surface coatings are widely used to change the physicochemical properties of metal-based ENMs to cross the BBB and target the brain. Surface modifications can change nanoparticle size, charge and uptake mechanism *etc*, which can lead to a wide variety of biomedical applications. This can also make them hard to investigate due to their complicated system and toxicity issues.

Surface modifications are commonly used in the ENM industry to tailor the dispersion characteristics of the ENMs to specific applications. PEGylation of ENMs has become the most widely used approach to increase the circulation lifetime of ENMs (155). PEGylated conjugated fluorescein-doped magnetic silica ENM (PEGylated FMSNs) could penetrate the BBB and spread into the brain parenchyma. However, FMSNs without PEG were easy to agglomerate, which resulted in a rapid clearance from blood circulation and subsequent capture by the MPS (156). In addition, this increased brain penetration was achieved without modification of the BBB permeability. No toxic effect arising from the PEGylated nanoparticles or from their degradation products has been detected toward the permeability of the BBB (157). Polyether-copolyester (PEPE) dendrimers internalized efficiently into brain vascular endothelial cells utilizing several pathways, but the major contributers were clathrin- and caveolin-mediated endocytosis. The PEPE dendrimers permeated across an *in vitro* BBB model in high amounts without significant disruption of the tight junction properties (131). Trimethylated chitosan (TMC) surface-modified PLGA nanoparticles enhanced the brain uptake of PLGA nanoparticles superior to the PLGA nanoparticles with negligible cytotoxicity (158).

Polysorbate 80-coated nanoparticles with brain diffusion capability were found to induce permeabilization of the BBB, likely due to toxic effects of free polysorbate 80, not the polysorbate 80-coated nanoparticles (157). In general, most of these surface modifications showed that they are promising candidates to increase the stability, change the physicochemical properties, and help to cross the BBB with less toxicity. However, most ENM research has shown indirect evidence of their flux across the BBB by analyzing extractions of the whole brain without excluding the ENMs in the brain vessels and BBB cells, or through therapeutic efficacy of drugs in animal models of brain tumors. There is an urgent need to understand how metal-based ENMs associate with and transcytose across the BBB *in vitro* and *in vivo*. When ENMs enter biological fluid, their surface properties interact with proteins leading to the exposure of new epitopes, altered function, and/or avidity effects (85, 159). By mimicking endogenous molecules we can investigate how surface modifications impact the uptake and fate of ENMs to the CNS.

Endogenous surface modifications are widely used to target specific receptors or translocation mechanisms. Tf-ENMs were found to be highly adsorbed by the BBB cells and endocytosed using an energy-dependent process compared with blank ENMs and BSA-ENMs. Tf-ENMs interact with the cells in a specific manner and enter the BBB via the caveolae pathway. Tf also prevented the aggregation of ENMs with less toxicity compared with chemical stabilizers such as Tween 20 and Tween 80 (132). However, the actual extent of Tf transcytosis is still unknown. Some studies showed that only a miniscule amount of Tf is trancytosed across the brain capillary endothelial cells and accumulated in the brain (160, 161). Albumin ENMs with covalently-bound ApoE were

detected in brain capillary endothelial cells and neurons; whereas, no uptake of ENMs occured without Apo E. Apo-E coated ENMs were taken up into the cerebral endothelium by an endocytic mechanism followed by transcytosis into the brain parenchyma (162). However, binding of apolipoproteins has been shown to correlate with rapid uptake into the liver and the spleen, and clearance of the particles by the MPS, a negative effect if one is attempting to increase circulation and retention time of the ENMs in the body (163). Angiopep-2, one of the peptides derived from the Kunitz domain, targets the low-density lipoprotein receptor-related protein-1 (LRP1). Several studies demonstrated that Angiopep-2 possessed a higher brain penetration capability both in an *in vitro* model of the BBB and *in situ* brain perfusion in mice (164, 165). Angiopep-modified polyamidoamine dendrimers showed higher efficiency in crossing the BBB than unmodified ENMs *in vitro* and *in vivo*. LRP1-mediated endocytosis may be the main mechanism of cellular internalization of angiopep-modified ENMs (166). According to our knowledge from the literature, no significant toxicity of angiopep-2 was reported and Angiochem Inc. has started clinical development with angiopep peptides for the transport of therapeutic agents in two Phase I clinical trials (117). In general, endogenous surface coatings are used as stabilizers to prevent agglomeration, gain functions to target specific targets, and reduce toxicity. We know little about the distribution, stability, and persistence of endogenous surface coated nanoparticles. At the same time, the endogenous surface coating may fall off or cause a loss of function, which may lead to agglomeration or enhance the rate of protein fibrillation (167).

2.4. Ceria ENMs

Ceria ENMs have many current commercial applications and potential therapeutic applications in the CNS, because of their redox capability. Ceria ENM is highly insoluble and can be observed under TEM, which makes it a good model to study particle pharmacokinetics in blood and their distribution. In this dissertation, citrate-coated ceria ENMs were chosen as a metal-based ENM model to study the effect of size on their pharmacokinetics in blood and their blood distribution *in vivo*. Furthermore, the BBB association of ceria ENMs and their flux across the BBB were investigated, which provide important information for their potential CNS applications.

2.4.1. Definition and their applications

Cerium is a lanthanide metal and a member of the rare earth metals. Ceria ENM has multiple commercial applications, such as a diesel fuel catalyst in Envirox® (Oxonica Ltd.) (25). Nanoscale ceria has been nominated by the National Institute of Environmental Health Sciences (NIEHS) for toxicological consideration due to its widespread and expanding industrial uses, limited toxicity data, and lack of toxicological studies (168). Cerium (IV) (stable form) and cerium (III) oxidation states coexist, producing a redox couple that is responsible for catalytic activity (169). The reduction of Ce^{3+} is compensated by a corresponding number of oxygen vacancies. The defect concentrations of Ce^{3+} ion and oxygen vacancies are larger at the surface of ceria than in the bulk (170, 171). Therefore the surface of cerium oxide contains defects, such as, Ce^{3+} ions and oxygen vacancies (172). Ceria ENM has higher Ce^{3+} concentration and enhanced redox activity with respect to larger particles, given the increase in the surface to bulk ratio (172). For these reasons, ceria ENM has been targeted as a potential

antioxidant agent to regenerate the initial oxidation state through redox cycling reactions (173). An autoregenerative mechanism for ceria was demonstrated (Figure 2.2) (174). The anti-oxidative stress ability of ceria ENMs showed a size-dependent pattern. With decreasing ENM size, the anti-radical ability increased, which was consistent with the Ce^{3+} concentration increase on the surface of the ENMs (175). Because of all these properties, numerous studies reported ENM ceria to be neuroprotective, suggesting it has utility in medical disorders caused by ROS (10, 12, 13, 17). The tetravalent state cerium (Ce^{4+}) is more stable than the trivalent state (Ce^{3+}). Meanwhile, a few studies reported that ENM ceria can increase oxidative stress (22, 176). It is very important to know whether the physicochemical properties of ceria ENMs will change their pharmacokinetics, biodistribution or how they interact with the biological barrier such as the BBB, regardless if you want to look at potential therapeutic applications or the toxicity of ceria ENMs.

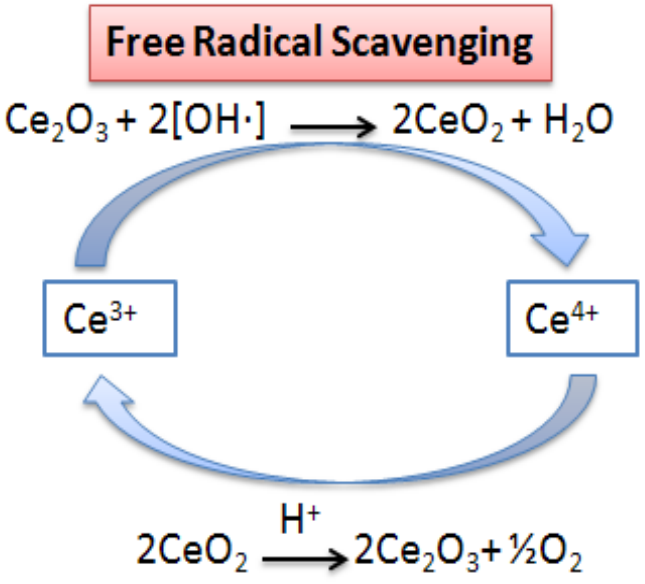

Figure2.2. Schematic Detailing the Regenerative Properties of Ceria ENM and probable mechanism of Cerium oxide nanoparticles' free radical scavenging property and auto-catalytic behavior. Adapted from (174).

2.4.2. Fate of ceria ENMs

The uptake of ceria ENMs of different sizes and concentrations has been previously studied using human lung fibroblasts *in vitro*. The study found that ceria ENMs were contained inside single or multiple lipid bilayer vesicles in the cytoplasm. They also showed that the size of the ceria ENMs affected the cell uptake greatly. With the increase of size, the cell uptake of ceria ENMs was significantly increased. However, small ceria ENMs agglomerated rapidly and cells can absorb agglomerates effectively. Large ENMs agglomerate slowly because of low number densities and can penetrate into the cells much more efficiently (152). This study demonstrated the importance of size on cell uptake of ceria ENMs. Furthermore, it is crucial to develop stable ENMs in the biological relevant system to study their cell association compared to micrometer size agglomerates.

For therapeutic applications, ceria ENMs need to be delivered through systemic administration rather than oral or inhalation *in vivo*. This is due to the fact that ceria ENMs are poorly absorbed through oral or inhalation routes. Twenty-eight days after inhalation a variety of concentrations were detected in various tissues, 1×10^{-5} % of the dose in the brain, 1×10^{-3} % in the kidney, 1×10^{-2} % in the spleen, and 1×10^{-1} % of the dose in the liver (32). A 7 nm ceria (5 mg/kg) was orally administrated. Only ~ 1×10^{-4} % of the dose was detected in the liver and less than 1×10^{-5} % was in the heart, spleen, kidney, brain, testicle, and lung 1 to 7 days later (177). Ceria was found in lung and

spleen, but not brain, heart, kidney, or liver of mice after 5 weekly oral doses of 0.5 mg/kg of a 3 to 5 nm ceria (178). For systemic administration of ceria ENMs, their pharmacokinetics in blood needs to be defined. In this dissertation, it is the first time that the influence of size on the distribution in and clearance from blood of ceria ENMs was investigated.

Our lab studied the biodistribution through iv infusion of 5, 15, 30 and 55 nm citrate-coated ceria. Of the ceria in the blood, brain, liver and spleen, ≥ 98% of the ceria was retained in the liver and spleen 20 h after its iv infusion, from which it was not significantly cleared over 30 days. Electron microscopy revealed only occasional ceria ENM beyond the BBB (179). The reasons for the lack of ceria ENM in the brain were unknown. One possibility is that ceria ENMs were rapidly coated by proteins in the blood that changed their physicochemical properties, resulting in their rapid clearance by the MPS (180, 181). Another possibility is that the ENMs agglomerated very rapidly in the blood or on a biological surface, changing their distribution and cell interaction (78, 182-184), so that the agglomerated ceria became too large or unavailable to penetrate the intact BBB. How ceria ENMs interact with brain capillary endothelial cells is relevant to the therapeutic use and toxicological consideration of ceria ENMs. In this dissertation, 5 nm ceria was used to study its association with the BBB.

2.5. Iron oxide nanoparticles

The pharmacokinetic study of ceria ENMs helped me to have a better understanding of the blood distribution of different sized citrate coated metal-based ENMs and their BBB

association. According the results of the ceria ENM project, I designed a novel IONP which has potential to improve the stability and the biocompatibility of IONPs. And its BBB association and flux across the BBB was tested, which will provide important information for its potential applications in the CNS.

2.5. 1. Definition and their applications

IONPs are superparamagnetic materials, which can be activated only in the presence of an external magnetic field, enabling various bionanomedical applications (185, 186). IONPs can be visualized in T2-weighted MRI sequences as a hypointense signal (negative contrast enhancement), which is the most widely investigated MRI contrast agent (187). IONPs have been approved by the Food and Drug Administration as MRI contrast agents including Lumiren® for bowel imaging (188), Feridex IV® for liver and spleen imaging (26), and Combidex® for lymph node metastases imaging (189). IONPs activated by AMF lead to a localized hyperthermia above 41-42 ºC resulting in cancer cell death (190). The particle sizes of IONPs can be tailored to accumulate in specific organs, contributing to early detection of human malignancies with blood vessel disruption such as brain tumor (191-193).

Numerous studies have shown that multifunctional IONPs can be used for brain tumor diagnosis and therapy. When comparing traditional gadolinium (Gd)-based MRI contrast agents to IONPs, it has been found IONPs are eliminated slower from the circulation (194). IONPs reside within brain tumors much longer than Gd-based agents (the half-life of Gd-DTPA is ~ 20 min in blood (195)) and can be imaged from 24 and 72 h. More

importantly, IONPs have revealed more intense MRI contrast enhancement compared with Gd-based contrast agents (100). Previous research also demonstrated that multifunctional IONPs can conjugate with chemotherapeutic drugs. Such drug-loaded IONPs can accumulated in brain tumors and facilitate monitoring drug delivery via MR imaging (196). Another promising application of IONPs is hyperthermia induced by AMF, which can be utilized for thermotherapy of brain tumors. The first *in vivo* report on IONPs inducing local hyperthermia to kill glioma cells was in 1997 using T-9 glioma cell, injected to Fisher F344 rats (36). After 1997, lots of studies have been done to test IONPs generating hyperthermia on glioma tumors *in vivo* (192). A hydrogel with iron oxide nanoparticles was tested using human glioblastoma cells (M059K). Cell death was observed where hydrogel was applied but not the surrounding region (43). Some studies also investigated the synergistic effects of combined gene and thermal therapy (197, 198). Most of the *in vivo* studies bypassed the BBB to deliver the IONPs to the tumor in the brain by intratumoral injection or implanting the tumor cells outside the brain regions (192). As I described in section 2.3, the BBB is the tightly regulated barrier to eliminate therapeutics from brain. It is necessary to understand whether multifunctional IONPs cross the BBB and increase their brain accumulation for brain tumor therapy.

A major challenge for effective delivery of IONPs to the CNS is the BBB. Many strategies have been developed to increase the flux of ENMs across the BBB as described in 2.3.3. IONPs can generate local hyperthermia by AMF. Mild hyperthermia demonstrated their ability to increase the BBB permeability and drug transport across the BBB (58). For example, previous research showed that the flux of liposomes across the

BBB increased significantly by whole body hyperthermia using 42 ºC water bath for 30 min *in vivo* (59). However, whole body hyperthermia led to potential toxicities to the brain such as edema (58). In this dissertation, I hypothesize that multifunctional IONPs have the potential to generate local hyperthermia to open the BBB and decrease the side effects of conventional hyperthermia by locally using AMF.

2.5.2. Biocompatibility of IONPs

Because of the favorable biocompatibility and biodegradability, IONPs have widespread biomedical applications (199, 200). However, surface modification of IONPs change the toxicity of IONPs dramatically. Bare IONPs led to oxidative stress in the lungs after intranasal instillation using two-sizes of IONPs (22 and 280 nm) (201). After inhalation of bare IONPs, neuron fatty degeneration occurred in the CA3 area of the hippocampus in the CNS (202). However, dextran surface modified IONPs showed no measurable LD50 (200). Even though retention of dextran-coated iron oxide NPs in the liver and spleen was observed in mice, but no histopathology alterations, including damaged cells, were found in the analyzed organs (203). In addition, IONPs are easily oxidized, transforming from magnetite (Fe_3O_4) to maghemite (γFe_2O_3), leading to a broad spectrum of particle size, shape, stability, and magnetic properties (108, 204). Particle stability also influences IONP toxicity and biological applications. For example, surfactants, typically prepared from multivalent polymers, have been developed to stabilize IONPs *in vivo*, yet they can get detached from IONPs due to an unclear mechanism by which ligand exchange occurs in metal chelates (205-207). Importantly, these IONP formulations, which change particle stability over time *in vivo*, could potentially cause toxic effects *in*

vivo (46, 47). Therefore, it is crucial to improve particle stability and biocompatibility of IONPs in biological environments.

Biocompatible polymers improve the stability of IONPs in aqueous solutions and avoid undesirable interactions with cells in the human body. Among these polymer-based formulations, polymer nanoassemblies are promising choices to improve the biocompatibility and stability of IONPs. For MRI contrast application, the signal-to-noise (S/N) ratio of contrast agents is very important for tumor imaging. Polymer nanoassemblies provide a stable nanocarrier without leakage of contrast agents during blood circulation, which leads to less blurring of cancer images (208). Micelles can embed IONPs and achieve excellent MRI contrast enhancement as a clustered IONP (51-53). However, a major disadvantage of self-assembling conventional micelles is their thermodynamic nature, which leads to instabilities, particularly in dilute conditions (e.g. blood and other biological environments) as polymer micelles can dissociate below the critical micelle concentration (54). To solve this problem, cross-links can be used to stabilize conventional micelles. Dr. Bae's lab developed CNAs from biocompatible PEG-p(Asp) block copolymers. They showed improved particle stability in biological related environments. Furthermore CNAs can entrap charged, hydrophobic, and amphiphilic payloads including drugs and contrast agents without changing particle sizes (55). CNAs have the potential to provide a stable and biocompatible platform to deliver IONPs for diagnosis and therapy.

2.6. Summary

The application of metal-based ENMs in medicine is an emerging field and has the potential to revolutionize the development of drug delivery, imaging, and diagnosis in the CNS. A variety of metal-based ENMs have been developed and engineered to cross the BBB for specific applications in the CNS. Because of the inherent complexity of the CNS and the safety concerns of metal-based ENMs, the fundamental understanding on the pharmacokinetics of metal-based ENMs, especially their BBB association will provide critical knowledge for further development of noble metal-based ENMs, which can be tuned to be effective therapeutic and diagnostic agents with low toxicity.

Chapter 3 Ceria engineered nanomaterial distribution in and clearance from blood: Size matters

The hypothesis of the present work is that the fate of a metal oxide ENM in blood is different than its constituent metal and ENM size influences its persistence in and distribution within the major components of blood. The kinetic endpoints include absorption (uptake), distribution, biotransformation (and protein corona), re-distribution (translocation), and elimination. These appear to be greatly influenced by the physicochemical properties of nanoscale materials. As noted in recent reviews of the pharmacokinetics of carbon-based and quantum dot ENMs (209, 210), they are not amenable to classical pharmacokinetic parameter estimations due to their differences from the solution chemistry of their components. In this chapter, we will characterize different sized ceria ENM distribution in and clearance from blood compared to the cerium ion. The results of this study will provide critical knowledge to engineer ENMs with desirable pharmacokinetics.

3.1. Introduction

There has been much research to develop ENMs. Polymer ENMs are being developed as drug delivery systems (211, 212), and some metal and metal oxide ENMs are being developed as therapeutic agents. Human exposure may also come from occupational and environmental sources. Little is known about ENM distribution or persistence in the

vascular system. We were unable to find published studies of the distribution of metal or metal oxide ENMs among blood compartments.

Little is known about the influence of size on the distribution in and clearance from blood of metal and metal oxide ENMs. We found that the blood cerium concentration was 0.56 and 1.3 mg/L after a 1 h infusion of 50 or 250 mg/kg of an ~ 30-nm commercial ceria ENM to rats (7). In contrast, 1 h after infusion of 100 mg/kg of an in-house manufactured 5-nm ceria ENM it was 370 mg/L (8), suggesting that the rate of metal oxide ENM clearance from blood was size dependent. The present study was conducted to test this hypothesis.

The present work was conducted to test the hypotheses that the fate of a metal oxide ENM in blood is different than its constituent metal and that ENM size and shape influence its persistence in and distribution within the major components of blood. We iv infused the cerium ion, four sizes of cubic or polyhedral citrate-coated ceria ENMs, and a mixture of cubic and rod-shaped ceria to rats. Blood was repeatedly withdrawn up to 4 h later, and in some cases up to 30 days. An aliquot of each blood sample drawn up to 4 h after ceria infusion was allowed to clot. By comparison of Ce in whole blood, serum, and the clot we could determine pharmacokinetic parameters of ceria distribution in, and clearance from, blood.

3.2. Materials and methods

3.2.1. Materials

Cerium chloride heptahydrate (Sigma-Aldrich #228931, 99.9% metal basis), cerium nitrate hexahydrate (Sigma-Aldrich # 22350, >99.0%), sodium hydroxide (Fisher #S318-1, certified ACS pellets), ammonium hydroxide (Fisher # 3256, ACS, 28-30%), hexadecyltri-methylammonium bromide (CTAB, Sigma-Aldrich #H9151, ~99.0%), deionized ultra filtered water (DIUF, Fisher #W2-20), and citric acid monohydrate (EMD Chemicals Inc # CX1725-1, GR ACS) were used without further purification.

3.2.2. Ceria ENM synthesis

Five nm ceria ENM was synthesized as described (213). Typically a 20 ml aqueous mixture of 0.5 M (0.01 mol) cerium chloride and 0.5 M (0.01 mol) citric acid was added to 20 ml of 3 M ammonium hydroxide. The latter was in excess of that needed for complete reaction of the cerium chloride to cerium hydroxide. The final product was an un-buffered ceria dispersion with a pH of 8 to 9. After stirring for 24 h at 50°C, the solution was transferred into a Teflon-lined stainless steel bomb and heated at 80°C for 24 h to complete the reaction. The cerium concentration in samples taken from the top and bottom of two ceria dispersion samples that were un-disturbed for > 2 months were within 2.5% of each other, demonstrating dispersion stability. Settling of the 5 nm ceria dispersion was not observed over at least three months and dynamic light scattering estimates of 5 nm ceria particle size distributions were similar to those obtained initially. The dispersed ceria ENM was infused intravenously without any further treatment.

Fifteen nm ceria ENM was synthesized using a hydrothermal procedure (214). In a typical procedure, 2 ml ammonium hydroxide was drop-wise added into 20 ml aqueous

mixture of 1.5 mmol cerium nitrate and 0.5 mmol CTAB and kept stirring for 0.5 h to form a brown emulsion. The emulsion was transferred into a Teflon-lined stainless steel bomb and heated at 120 °C for 24 h to complete the reaction. The fresh product was washed with water three times to remove free cerium, dialyzed three times with fresh citric acid aqueous solution, and dried at 55 °C for 24 h. The final 15 nm citrate-modified ceria powder was re-dispersed into water to prepare a ~5 wt% aqueous suspension. The pH of the resulting un-buffered ceria dispersion was 3.5.

Thirty nm ceria was synthesized using a hydrothermal approach (215). Generally, 20 ml aqueous mixture of 1 mmol cerium nitrate and 105 mmol sodium hydroxide was stirred for 0.5 h to get a milky suspension. The suspension was transferred into a Teflon-lined stainless steel bomb and heated at 180 °C for 24 h. After the hydrothermal treatment, fresh white precipitates were washed with deionized water three times and then ethanol three times to remove the free cerium and organic impurities. Then the wet precipitates were dispersed into 0.05 M citric acid aqueous solution with stirring overnight, followed by washing with water 5 times. The resulting dispersion had a pH of 3.9.

The mixture of 30 nm cubic ceria ENMs with nanorods was synthesized using a hydrothermal method (216). Typically, 0.9 mmol cerium nitrate was dissolved into 15 ml 9 M sodium hydroxide solution with stirring for 0.5 h. The suspension was transferred into a Teflon-lined stainless steel bomb and heated at 140 °C for 48 h. After the hydrothermal treatment, fresh precipitates were separated by centrifugation, and washed with deionized water three times. The wet precipitates were dispersed into 0.06 M citric

acid aqueous solution overnight, washed with water for several times until the final suspension had a pH around 7.

Fifty-five nm ceria ENM was synthesized by a method (217) modified with controlled thermal treatment to achieve the desired ceria particle size (unpublished results). It was re-dispersed in citrate solution and washed three times in doubly distilled water to remove free cerium and citrate. The resulting dispersion had a pH of 7.

3.2.3. Ceria characterization

The morphology, crystallinity, and phase purity of each citrate-coated ceria ENM were determined in our laboratories using high resolution-transmission electron microscopy/scanning transmission electron microscopy and X–ray diffraction (XRD) analyses. Primary particle size distributions were determined by TEM analysis (184). The crystallinity of all ceria ENMs were determined by XRD (Siemens 5000 diffractometer). Particle size distributions in aqueous suspension were determined using dynamic light scattering (90Plus Nanoparticle Size Distribution Analyzer, Brookhaven Instruments Corp, Holtsville, NY). To indicate the stability of the ceria dispersion when infused into the rat, the zeta potential was measured for each ENM (except the mixture of ceria nanoparticles and nanorods) using a Zetasizer nano ZS (Malvern Instruments, Worchestershire, UK). The Zetasizer estimates the surface charge of nanoparticles based on the assumption that the correlations are generated from spheres, but nanorods have an elongated axis and different mobility from spherical nanoparticles; the instrument therefore often fails to provide consistent and accurate estimation for nanorods and

mixtures that include rods. Since all of the ceria ENMs had hydrodynamic diameters < 200 nm, the Hückel approximation was used to calculate zeta potential from electrophoretic mobility. To estimate the extent of citrate surface coating each of the ceria ENMs was washed at least three times with water before drying. As separation of the 5 nm ceria by centrifugation required ~12000 rpm for 12 h due to their small size, they were agglomerated by decreasing the pH to 4, enabling centrifugation. Thermogravimetric analysis (Perkin-Elmer TGA7 Analyzer) was then performed to investigate the weight loss of citrate-coated ceria ENMs over the temperature range of 150 to 300°C under which decomposition of citric acid occurs. The extent of citrate surface coating was estimated based on the assumption that all the ceria NPs were spherical and had uniform size. The free cerium concentration in the ceria dispersions of the unwashed 5 nm ceria and each of the washed ENMs was determined using Amicon Ultra-4 centrifugal 3000 molecular weight cut-off filter devices and centrifugation at 3000 g to obtain filtrate, which was analyzed for cerium by inductively coupled plasma mass spectrometry (ICP-MS).

3.2.4. Animals

Data were obtained from 101 male Sprague Dawley rats, weighing 325 ± 30 g (mean ± SD), that were housed individually in the University of Kentucky Division of Laboratory Animal Resources facility. All animal studies were approved by the University of Kentucky Institutional Animal Care and Use Committee. The research was conducted in accordance with the Society of Toxicology's Guiding Principles in the Use of Animals in Toxicology (http://www.toxicology.org/ai/air/air6.asp).

3.2.5. Cerium ion and ceria ENM administration

Rats were prepared with 2 cannulae, surgically inserted into femoral veins under ketamine/xylazine anesthesia, which terminated in the vena cava, and were connected to infusion pumps via a flow-through swivel. This enabled conduct of the study in the awake, mobile rat. All samples were sonicated to ensure dispersion prior to administration. The day after cannulae implantation the un-anesthetized rat was infused via the longer cannula with cerium ion (as the chloride), a ~ 5% ENM dispersion in water, or water. A pilot study was conducted with the cerium ion and each of the ceria ENMs to determine tolerability following iv infusion. A 100 mg cerium ion/kg infusion was lethal. Rats were infused with ~250 or 175 mg/kg of the 5 nm ceria; 3 of 8 died. A dose of ~250 mg of the 15 nm ceria/kg was tolerated. Infusion of 100 mg/kg of the 30 nm ceria resulted in some evidence of mild distress (tachypnea, skittish behavior, and not resting well). Dyspnea and lethargy were seen in rats given 250, 100 or 78 mg of the 55 nm ceria/kg. Therefore the target doses were 100 mg/kg for the 5, 15, and 30 nm ceria and 50 mg/kg for the 55 nm ceria ENM and the cerium ion. ICP-MS analysis of cerium in replicate samples of the dosed materials showed the doses to be 70 to 100% of the target doses. Each was infused over 1 h, except for the cerium ion that was infused over 2 h. Control rats received water adjusted to the pH of the paired ceria ENM or cerium ion. To compensate for the iv administration of a considerable volume of grossly hypotonic infusion, concurrent iv infusion of an equal volume and rate of 1.8% sodium chloride in water was delivered into the second, shorter, cannula. Each fluid was delivered at ~ 0.6 ml/h.

3.2.6. Sample collection

After the infusion, 0.6 ml blood was withdrawn at 0.167, 0.5, 0.75, 1, 2 and 4 h from the cannula that had not delivered ceria from 3 rats that had received infusion of the cerium ion, 6 that received the 30 nm ceria ENM, and 5 that received the 5, 15, 55 or 30 nm ceria cube + rod ENM. The blood sample was immediately separated volumetrically into two 0.3 ml aliquots to enable determination of Ce in whole blood in one and in the serum and clot fractions of the other. A blood clot is formed by platelets and blood proteins, including fibrin, and traps the blood's red and white cells. It may have some serum trapped in it; therefore the clot fraction may over-estimate the percentage of Ce associated with cells. To determine the distribution of Ce in the serum and clot fractions the 0.3 ml sample of whole blood was allowed to clot at room temperature, the clot given time to contract, and serum withdrawn into a digestion vessel. The clot was withdrawn and placed in another digestion vessel and the remaining serum added to the serum sample. This enabled determination of the mass amount of Ce in the two major compartments of blood; serum and, from the clot fraction, association with the formed elements (red cells, white cells and platelets). This approach was taken to avoid centrifugation to generate the serum sample because we found that centrifugation at 1600 g for 10 min, as used to generate serum, resulted in loss of ~ 75% of a 30-nm ceria ENM from the serum sample (7).

Blood was also obtained from some rats 20, 168 (1 week) or 720 h (30 days) after ceria ENM administration. An equal volume of saline was infused after each blood withdrawal to replace the fluid volume. Blood was obtained at termination of all rats.

3.2.7. Cerium analysis

To determine Ce in whole blood, the sample was transferred into a 55 ml TFM (polytetrafluoroethylene) digestion vessel (CEM) to which 6 ml trace-metal grade nitric acid and 3 ml 30% H_2O_2 were added, digested in a CEM MARS Xpress microwave at 180 °C for 10 min to convert all ceria to dissolved Ce^{4+}, diluted with 18 MΩ water to 50 ml, and subsequently further diluted dependent on the Ce concentration.

Cerium concentration was determined in whole blood, serum and clot by ICP-MS (Agilent 7500cx, Santa Clara, CA, U.S.). Following ceria ENM administration, Ce concentration is believed to reflect the Ce in ceria ENM because ceria ENMs are quite inert and persist as an ENM in the rat for months (27), and the Ce levels in non-Ce treated rats is very low. We determined a method detection limit (MDL) of Ce for blood and serum samples of 0.018 mg/L (7). No samples in this study had Ce concentrations below this MDL. Seven samples, containing whole blood, serum or clot, were analyzed in duplicate and were spiked with 8.3 ng Ce/ml. Results of duplicate analysis showed a range of 0 to 4% between the two determinations. Recovery of the Ce spike ranged from 93 to 114%, averaging 105%.

3.2.8. Data analysis and statistics

Blood, serum and clot Ce concentrations were normalized to an infusion dose of 100 mg ceria/kg for all rats, based on determination of the actual Ce content of the infusions by ICP-MS analysis, and because a few materials were given at doses other than 100 mg/kg, as noted above. This enabled direct comparison of results from the cerium ion, ceria ENM sizes, and shapes. Outliers, identified using the Grubbs test, were not included in the data analysis. Four percent of the 600 whole blood, serum and clot samples were outliers by this test.

Pharmacokinetic modeling. Non-compartmental and compartmental analyses of the whole blood Ce concentration vs. time results were conducted using WinNonLin, a pharmacokinetic analysis program (Pharsight®, St. Louis, Missouri). For non-compartmental analysis, AUC (h*mg/L), C_{max} (mg/L), half life ($t_{1/2}$, h), and mean residence time (MRT, h) were calculated. The squared correlation of distances (Rsq) and correlation between time (X) and Ce concentration (Y) (Corr-XY) were used to measure the goodness of fit. For compartmental analysis, one and two compartments were evaluated to determine the best model fit. AUC (h*mg/L), C_{max} (mg/L), half life ($t_{1/2}$, h), mean residence time (MRT, h), clearance (CL, ml/h/kg) and apparent volume of distribution at steady state (Vd_{ss}) were calculated. Various weightings were evaluated, including 1, 1/y (y: ceria concentration, which weights higher values more heavily), $1/y^2$ (which weights lower values more heavily), 1/predicted concentration (iterative reweighting), and 1/predicted concentration^2. Goodness of fit was based on visual inspection, weighted corrected sum of squares, sum of square residuals, weighted sum of

square residuals, random distribution of residuals, Akaike's information criteria, and Swartz criteria. The initial estimates for model parameters were calculated as below.

The semi-logarithmic plots of blood concentration vs. time data showed the one or two compartment kinetics model as , respectively. represent intercepts on the concentration (Y) axis of the back-extrapolated initial and terminal phases and the initial and terminal slopes. As blood sampling began after completion of the infusion, the iv bolus case was used. ——— was used to correct the infusion intercept values for the one compartmental analysis and ——— and ——— were used in the two compartment model. is the infusion dose, is the infusion rate. —— was used to calculate the volume of the central compartment. The micro rate constants were determined as ——— —; . k_{12} and k_{21} represent the rate constants between central and peripheral compartment, and k_{10} is the elimination rate constant from the central compartment. The elimination half-lives ($t_{1/2}$) were calculated as $t_{1/2\lambda 1} = 0.693/\lambda_1$ and $t_{1/2\lambda 2} = 0.693/\lambda_2$. One-way ANOVA, followed by Tukey's multiple comparison tests (Prism 5.02 software, GraphPad, San Diego, CA), was used to test for significant differences in pharmacokinetic parameters among the 6 treatment groups.

Quality analysis of the WinNonLin coefficients was conducted by determining whether the ratio of the coefficient estimate to its average standard error was greater than the appropriate p value < 0.05, using a two-tailed Student's t-test (3.18 for n = 3, 2.78 for n =

4), Excel and Systat. The results showed that the pharmacokinetic parameter estimations using WinNonLin were acceptable for only the cerium ion and the 5-nm ceria ENM. Two factors contributing to this were 1) that less than 2% of the dose of the other 4 ENMs was circulating in the blood when the first sample to estimate the pharmacokinetic parameters was obtained (0.167 h after completion of the infusion), and 2) the Ce concentration increased in blood from 0.167 to 4 h after infusion of the 15- and 30-nm ceria, which is not the elimination behavior for typical pharmacokinetic models. Therefore, the pharmacokinetic data for ceria ENMs was compared directly to that of the cerium ion, which is known to follow typical pharmacokinetic elimination models.

Ratio of Ce concentration in whole blood following infusion of ceria ENMs vs. the cerium ion. The Ce ratio in ceria ENMs compared to the cerium ion was reported as $R = \frac{[Ce]_{ceria}}{[Ce]_{cerium(ion)}}$, calculated for each of the six sample times. This provided the opportunity to see temporal differences between the ENMs and the cerium ion. The ratio for each ENM was plotted as a function of time from 0 to 4 h. Linear, exponential, power law, and 2nd order polynomial equations were used to evaluate the data over 4 h. Because the linear, exponential, and power law equations required only two parameters for fitting, they could be used to demonstrate common trends for small data sets (usually six points over the 4 h time period). The partition ratio, R, for each ENM was evaluated to determine whether there was a significant trend in the data. This was done by evaluating fits of linear, exponential, and power law equations to the data over the time period, $0 < t \leq 4$ h. Quality of the fitted coefficients was evaluated by using the Student's t-test

criteria. For example, if the exponential factor for the model $R = R^0 \cdot \exp(-\alpha \cdot t)$ met the t-test criterion, then the trend was described by an apparent first order process.

Ce partitioning between serum and clot. The quality of the data describing the partitioning of Ce between the serum and clot fractions was screened using mass balances. The total mass of cerium (or ceria) in the whole blood sample should equal the sum of the cerium masses in the serum and clot phases. The cut-off for mass material balance screening was taken to be ± 30%. If the sum of the masses of Ce in the serum and clot phases was < 70 or > 130% of that in the mass in the whole blood sample, the partitioning data were not used in the analysis or shown in the figure. No other screening analyses, such as outlier evaluation, were applied. The partitioning of cerium was reported as the ratio of cerium in the serum phase to that in whole blood.

3.3. Results

Particle morphologies are shown in Figure 3.1. Panel D in Figure 3.1 is part of a larger image that shows the diameter and length of the rods in the mixture of 30-nm cubic and rod ENMs were ~ 10 nm and 2 µm, respectively. The shape, surface area, zeta potential in water, and estimated extent of the ENM surface that was coated with citrate are shown in Table 3.1. All of the ceria ENMs had face-centered cubic (FCC) crystal structures with the same Miller indices of (111), (220) and (311), and with lesser presence of (200), (222) and (400), based on XRD crystal structure linked to known morphology. The 55 nm ceria had the lowest surface coating of citrate and a lower absolute surface charge (-31.5 mV) than the other ENMs. The unwashed 5 nm ceria ENM had 11.6 ± 0.3% free

cerium in the dispersion. The washed ceria ENMs were found to contain << 1% free cerium.

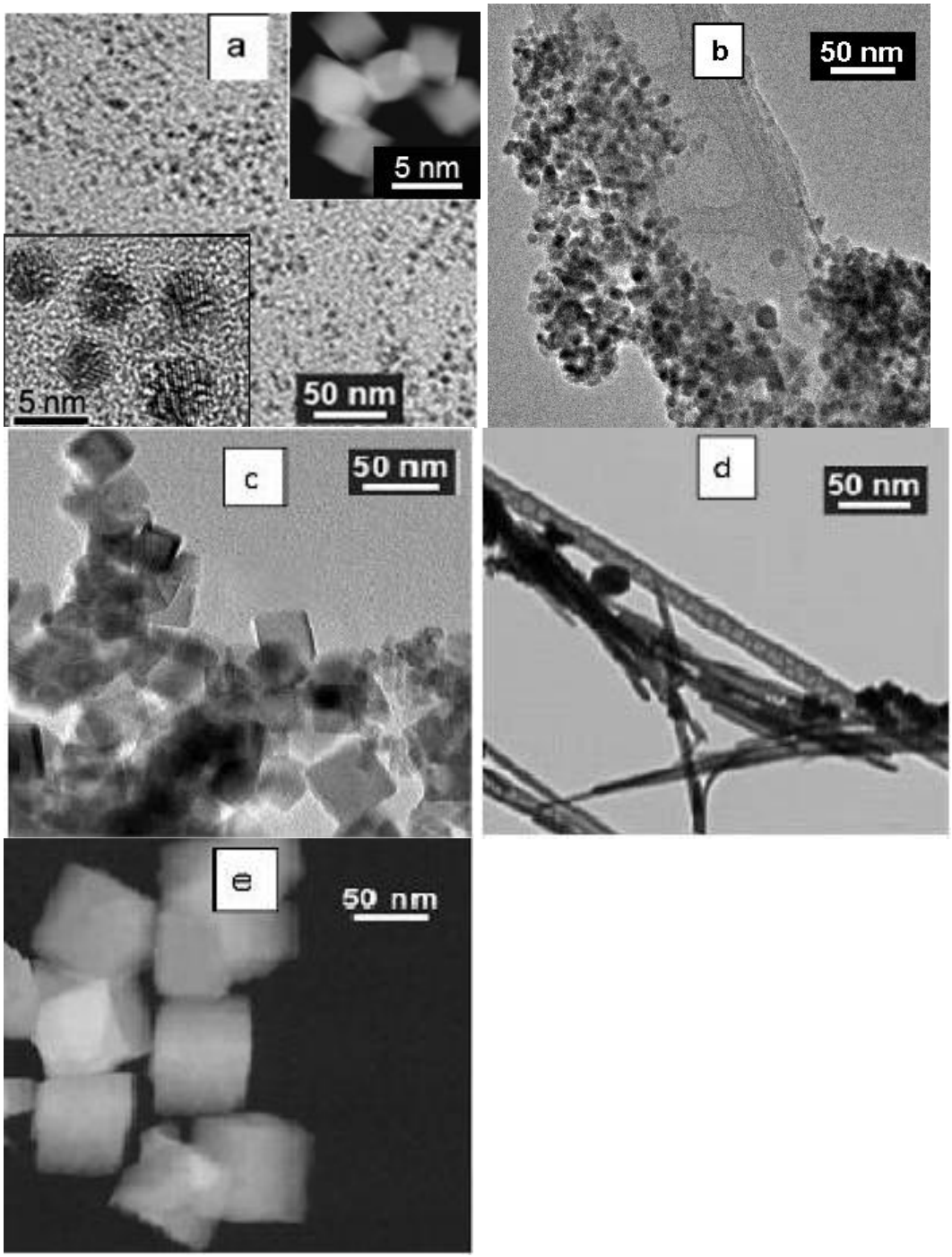

Figure 3.1. HRTEM and STEM images of ceria used in this study: (a) TEM/STEM: 5-nm polyhedral ceria; (b) TEM: 15-nm polyhedral ceria; (c) TEM: 30-nm cubic ceria; (d) TEM: 30-nm cubic and rod ceria; (e) STEM: 55-nm polyhedral ceria.

Table 3.1. Physico-chemical properties of the ceria ENMs. Shape delineation based on TEM data. D_{ave} (average primary particle diameter from number frequency distribution) and standard deviation based on TEM measurements of diameter fitted using lognormal distribution models (n = 100). Citrate loading expressed as % of monolayer coverage (TGA analysis).

Ceria ENM primary size(nm)	shape	$D_{ave,}$ nm (st. dev.) [TEM, Lognormal model]	zeta potential in water at pH~ 7.3 (mV)	extent of surface citrate coating
5	polyhedral	4.6 (0.135)	- 53 ± 7	~ 40%
15	polyhedral	12.0 (0.232)	- 57 ± 5	~ 27%
30	cubic	31.2 (0.478)	- 56 ± 8	~ 18%
55	polyhedral	55 (0.162)	- 32 ± 2*	~ 15%*

* Determinations made on a batch similarly-prepared to that administered to the rats

Ten min (0.167 h) after completion of the cerium ion or 5-nm ceria ENM infusion ~ 14 and 32% of the Ce remained in the circulating blood, respectively. This was calculated from the measured blood Ce concentration compared to the Ce dose, based on the iv infusion of 100 mg ceria/kg into the rat's vascular system (~ 7% of its body volume), which would introduce ~ 1163 mg Ce/l blood. In contrast, the 15-, 30- and 55-nm ceria and mixture of 30-nm cubic + rod ceria were rapidly removed from circulation, so that 0.167 h after their infusion ≤ 2% was in blood (Figure 3.2).

Pharmacokinetic models were constructed using whole blood Ce concentrations from each individual rat's results. Non-compartmental models showed the best fits for the cerium ion (Rsq 0.94 ± 0.08, Corr XY = 0.97 ± 0.04) and 5 nm ceria ENM (Rsq 0.89 ± 0.06, Corr XY = 0.94 ± 0.03). However, 15, 30 cubic, 30 cubic + rods, and 55 nm ceria ENMs were poorly fitted by non-compartmental models. One and two compartment

models showed the Ce concentrations in blood obtained 0.167 h to 1 week after cerium ion infusion and 0.167 h to 30 day following infusion of 5-, 15-, and 30- nm ceria ENMs were best fit by two compartmental models (biexponential decay). For the mixture of 30-nm cubic + rod ceria and the 55-nm ceria ENMs, for which modeling was based on results to 4 h after their infusion, the one compartment model provided the best fit.

Table 3.2 summarizes the pharmacokinetic parameters. Compartmental analysis showed the cerium ion to have a greater AUC than the ceria ENMs, a higher C_{max} compared to the ≥ 15 nm ENMs, and a smaller Vd_{ss} than all of the ENMs. Surprisingly, the 15- and 30-nm cubic ceria materials showed increasing blood concentrations over the period 0 to 4 h after infusion, with estimated half-lives of this process of ~ 4 and 2.7 h, respectively (Figure 3.2). Since conventional elimination models are always monotonically decreasing in solute concentration, the WinNonLin fits were poor and the 15 and 30 nm ceria ENMs model coefficients did not meet the Student's t-test criteria for quality (the average standard error was often larger than the estimated value of the coefficient).

With the exception of the 5-nm ceria ENM, the pharmacokinetic results are based on < 2% of ceria dose that was remaining in the blood 0.167 h after completion of the ceria infusion, therefore the pharmacokinetic parameter estimates describe only a small fraction of the dose of these ENMs. The two-compartment models for each of the rats that received cerium ion or 5-nm ceria ENM infusions fit the data very well based on visual inspection, weighted corrected sum of squares, sum of square residuals, weighted

sum of square residuals, random distribution of residuals, Akaike's information criteria, and Swartz criteria.

Figure 3.3 shows the ratio of the whole blood Ce concentration after infusion of 5-, 15-, 30-, and 55-nm ceria ENMs vs. the cerium ion. The ratio, R, for 5 nm ceria ENM could be modeled either by a power law dependence, $R = R_0 \cdot t^d$ (R_0 is a constant and d is the power exponent for time *t*), or an exponential dependence, $R = R_0 \cdot \exp(d \cdot t)$ (R_0 is the Arrhenius-type factor and d is the process rate constant) for each of three animals. Trend lines are shown for the power law dependence (Figure 3.3, top left panel) with d ~ -0.8. Five-nm ceria ENMs are fitted by two-compartment models and their blood concentrations showed time dependent decreases compared to cerium ion blood concentrations. Over the time period, 0 to 4 h after infusion, it was cleared faster than the free ion. On the other hand, R values for both 15 and 30 nm ceria increased over the 0 to 4 h time period and their exponential coefficients were similar (d = 0.41 h^{-1} and d = 0.45 h^{-1}, respectively). The R value of 55 nm ceria showed no strong trend.

The Ce mass balance for cerium ion, calculated by comparing the cerium in the serum plus clot samples to the cerium in whole blood, averaged 98 ± 7% over all samples. For the 5-nm ceria ENM, the average mass balance was 83 ± 44%; 5 out of the total of 30 values from the 6 sample times were below the cutoff of 70% mass balance. These ranged from 16 to 31% and were obtained 120 or 240 min after the ceria infusion, at a time when Ce concentrations had decreased to an average of 8 and 0.4 microgram Ce in the serum prepared from the 0.3 ml of blood. They were not used in the data analysis. For

the remaining 25 values, recovery was 93 ± 40%. For the 15-, 30-, and 55-nm ceria ENMs, 17, 16 and 11 of the 18 values from 3 of the rats met the material balance quality control criteria and were used in the data analysis, respectively. For the 30-nm ceria cubes and rods mixture, 12 values from 2 rats met the material balance quality control criteria and were used in the data analysis.

Figure 3.4 shows the ratio of Ce distribution in blood serum vs. whole blood from 0.167 to 4 h after completion of the cerium ion or ceria ENM infusions. The ratio of Ce in serum vs. whole blood shows its distribution between blood serum and the clot fraction (associated with the red and white cells and platelets). Blood samples taken from 0 to 4 h after infusion showed that the cerium ion, 5-, and 55-nm ceria ENMs did not preferentially distribute into either the blood serum or clot (containing red, white cells and platelets); there was no consistent time dependence of the ratio for all animals. The 30 nm cubic + rod mixture preferentially distributed to the clot fraction over a similar period, also with no consistent time dependence of the ratio for all animals. However, serum/clot partition data for 15- and 30-nm ceria showed that these ENMs migrated into the clot fraction, and that partition ratio of ceria in the clot increased with time. Two of the rats that received 15 nm and 4 that received 30 nm ceria showed a statistically significant increase of Ce associated with the clot fraction.

Table 3.2. Pharmacokinetic parameters for the cerium ion; 5-, 15-, 30- and 55-nm ceria ENMs; and mixture of 30-nm cubic and rod ceria ENMs and after iv infusion to rats. Values are means ± SD, calculated from results obtained from times shown (after completion of the infusion).

Parameter	0.167 h to 7 days	0.167 h to 30 days			0.167 to 4 h	
	cerium ion (n=3)	5-nm ceria (n=3)	15-nm ceria (n=4)	30-nm cubic ceria (n=5)	30-nm cubic + rods ceria (n=5)	55 nm ceria (n=5)
			Non-compartmental Analysis			
AUC (h* mg/L)	326 ± 102[a]	2264 ± 1284[b]	361 ± 130[a]	2201 ± 1314[b]	25 ± 8[a]	1.5 ± 0.5[a]
C_{max} (mg/L)	163 ± 27[a]	278 ± 215[b]	0.95 ± 0.34[a]	6.5 ± 3.1[a]	20 ± 11[a]	0.78 ± 0.12[a]
$t_{1/2}$ (h)	2.7 ± 0.8[a]	80 ± 25[b]	-	-	26 ± 36[a]	2.2 ± 0.8[a]
MRT (h)	1.5 ± 0.2[a]	7.1 ± 3.0[a]	41 ± 11[b]	15 ± 11[a]	1.6 ± 1.8[a]	1.5 ± 0.1[a]
			Two Compartment Model			One Compartment Model
AUC (h* mg/L)	1377 ± 416[c]	690 ± 181[a]	152 ± 41[b]	561 ± 256[a]	72 ± 39[b]	1.9 ± 0.7[b]
C_{max} (mg/L)	190 ± 29[a,b]	372 ± 317[a]	0.82 ± 0.45[b]	3.5 ± 1.7[b]	12 ± 5[b]	0.88 ± 0.44[b]
$t_{1/2-\alpha}$ (h)	0.57 ± 0.13	0.44 ± 0.27	2.5 ± 2.6	12 ± 17	4.3 ± 1.8	1.9 ± 0.6
$t_{1/2-\beta}$ (h)	16 ± 3[b]	124 ± 53[a,b]	239 ± 56[c]	140 ± 43[a]	-	-
MRT (h)	21 ± 3[c]	92 ± 53[a,c]	343 ± 83[b]	192 ± 57[a]	6.3 ± 2.6[c]	2.8 ± 0.8[c]
CL (L/h/kg)	0.078 ± 0.028[a]	0.15 ± 0.04[a]	0.71 ± 0.24[a]	0.22 ± 0.11[a]	1.4 ± 1.0[a]	46 ± 30[b]
Vd_{ss} (L/kg)	1.7 ± 0.8[a]	15 ± 12[a]	240 ± 8[b]	38 ± 12[a]	9.6 ± 3.9[a]	130 ± 42[c]

AUC, area under the concentration–time curve; $t_{1/2-\alpha}$, first half-life; $t_{1/2-\beta}$, second half-life; C_{max}, peak concentration; CL, Clearance; MRT, mean residence time; Vd_{ss}, volume of distribution at steady state.

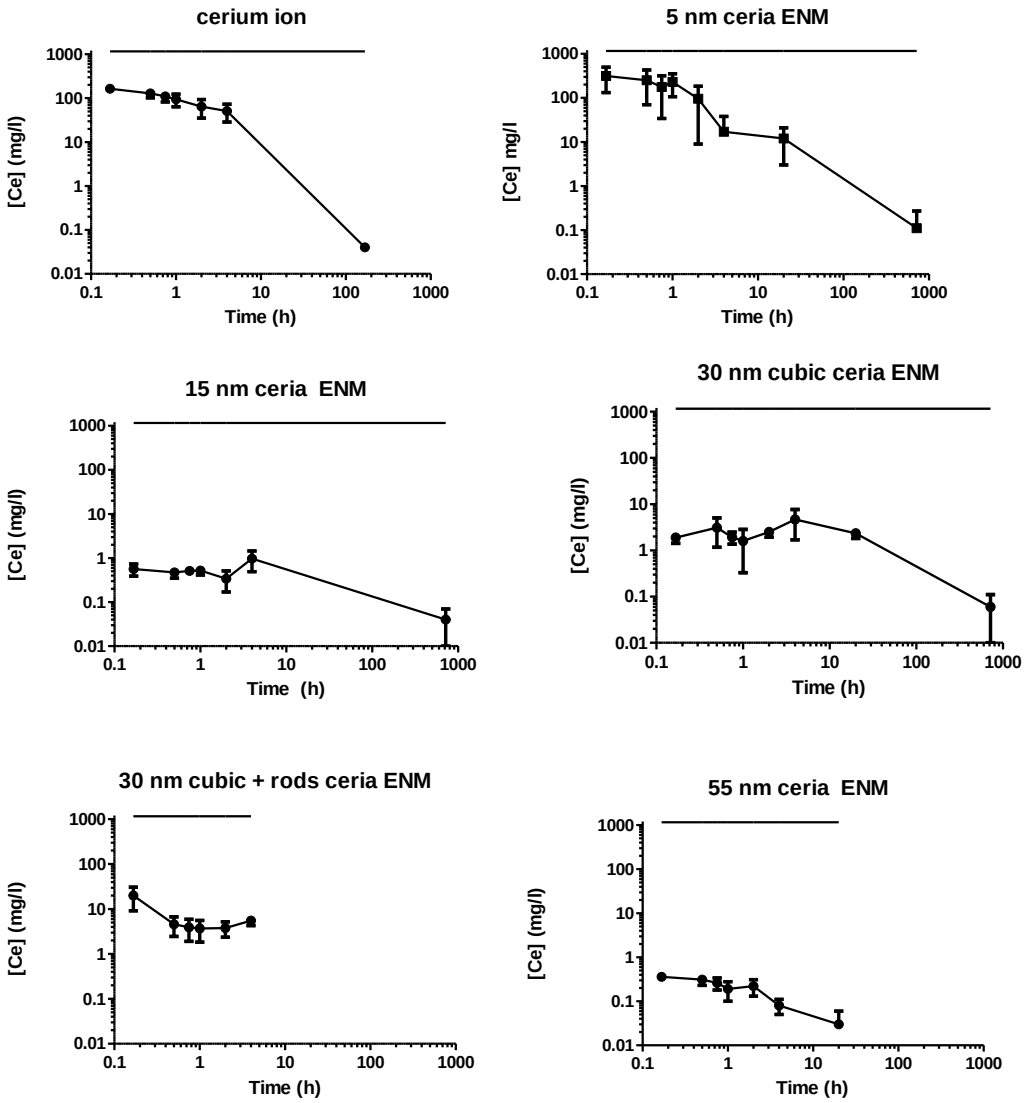

Figure 3.2. Whole blood Ce concentration after completion of iv infusion of the cerium ion, 5, 15, and 30 ceria ENM, a mixture of 30-nm ceria cubes and rods, and 55-nm ceria ENM. All values are normalized to an equivalent dose of 100 mg ceria/kg. Results are mean ± S.D. from 5 rats at each time point, except for cerium ion, where n = 3 for 5 nm ceria ENM where n = 9, 10, 21, 10, 12, and 7 rats at 0.167, 0.5, 1, 2, 20 and 720 h; for 15 nm ceria ENM where n = 10 rats at 0.167, 0.5, 1, 2, and 4 h; for 30 nm ceria ENM were n = 6 for all times except 1, 20 168 and 720 h where n = 10, 8, 3 and 11; and for the 55 nm ceria ENM were n = 10 and 7 at 1 and 20 h, respectively. The horizontal line at the top of each graph shows the calculated cerium concentration in blood representing 100% of the dose.

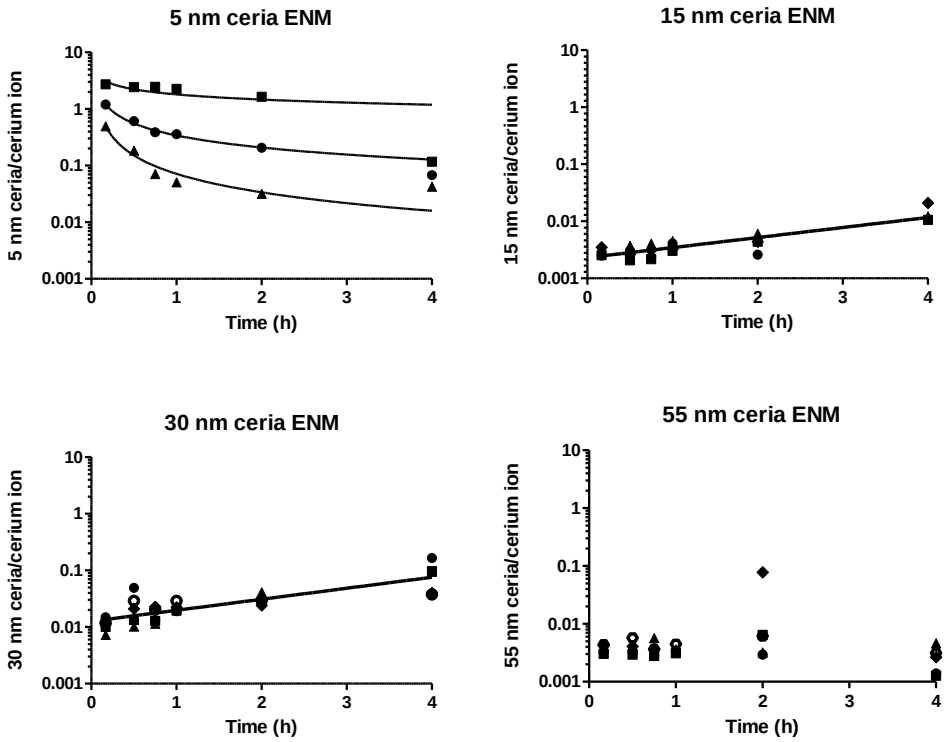

Figure 3.3. The ratio of Ce concentration in whole blood following iv infusion of 5-, 15-, 30- and 55-nm ceria ENMs from 0.167 to 4 h after their infusion, compared to the cerum ion concentration. Each symbol represents a different rat.

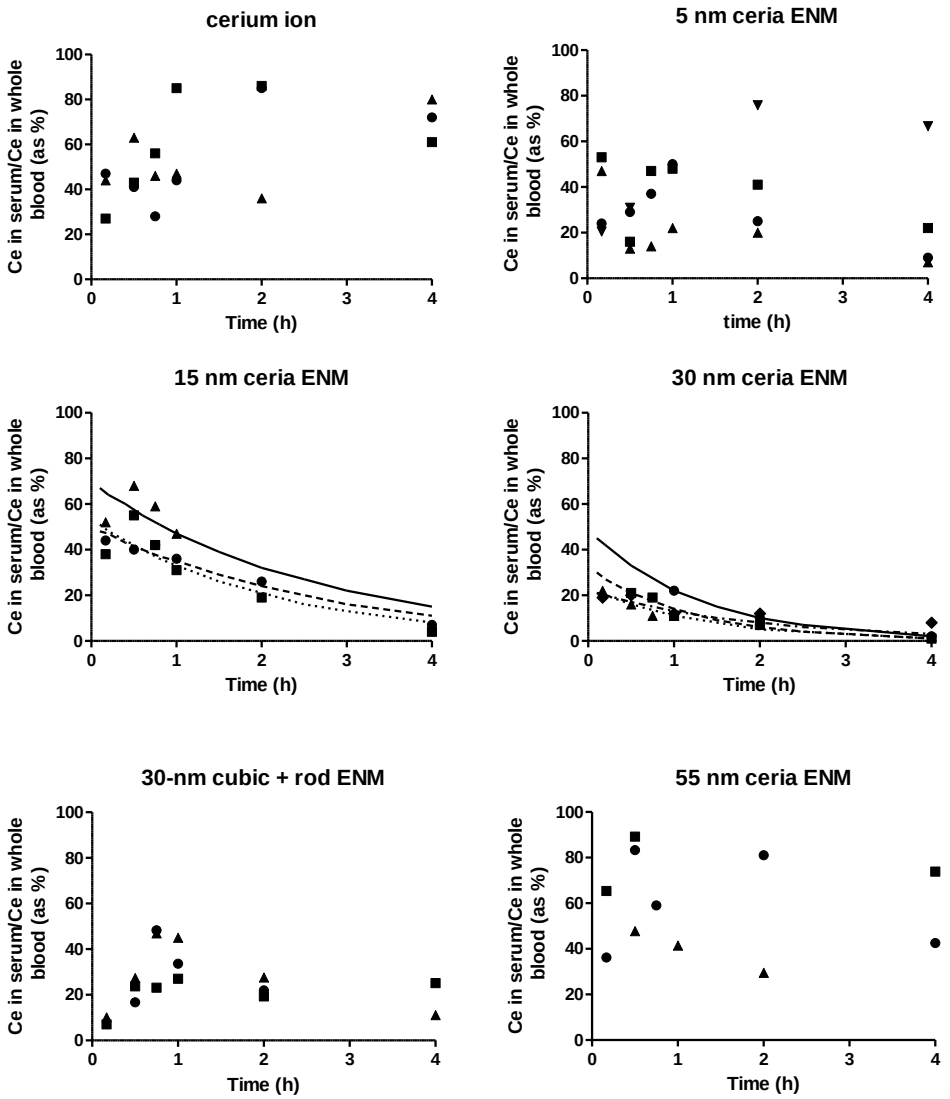

Figure 3.4. The ratio of cerium in serum to whole blood (as %), following iv infusion of the cerium ion; 5-, 15-, and 30-nm ceria ENMs; mixture of 30-nm cubic + rod ceria ENMs; and 55-nm ceria ENM. Each symbol shows results from a different rat. For the 15-nm ceria ENM the solid curve is the model for the rat shown by the open circle, dashed line for rat shown by the closed square, and double curve for rat shown by the closed diamond. For the 30-nm ceria ENM the solid curve is the model for the rat shown by the closed square, dashed line for rat shown by the open circle, double curve for rat shown by the closed diamond, and long dash dot curve for rat shown by the open triangle.

3.4. Discussion

The crystal structure of the ceria ENMs was as expected because the fluorite structure is the only one for crystalline CeO_2. The citrate coating was least dense on the 55 nm ceria, suggesting it would be the most likely of the ENMs tested to agglomerate in aqueous dispersion; a problem that was observed during its administration requiring frequent agitation of the dispersion to prevent it from occluding the infusion line. Although nearly 12% of the total cerium in the 5 nm ceria ENM was free cerium in the aqueous phase, comparison of the results after infusion of the 5 nm ceria ENM, the cerium ion, and the other ceria ENMs shows the free cerium cannot account for the differences between the 5 nm and the larger ENMs.

In the present study ~ 14% of the cerium ion remained in the blood 0.167 h after completion of a 1 h iv infusion. In a previous report Ce was determined in blood from 1 h to 3 days following its iv administration as the chloride to mice and rats; however, the author did not conduct a pharmacokinetic analysis of the results (218). Using WinNonLin to conduct pharmacokinetic analysis, non-compartmental and compartmental calculations of the Bjondahl results (218) showed similar AUC, MRT, C_{max}, and CL results. The non-compartmental half-life (10 h) was the same as the terminal half-life obtained with a two compartment model, which best fit the data for compartmental analysis. The initial half-life of the Bjondahl results (~ 3 h) was longer than we obtained (0.6 h) because our study included samples taken as early as 10 min, whereas the first sample in the Bjondahl study was obtained at 1 h.

Ten min after completion of the iv infusion of ceria ENMs, ~ 32% of the 5-nm ceria but < 2% of the larger ceria ENMs were present in the blood. The greater extent of citrate coating on the 5-nm ceria (and therefore its greater hydrophilicity) may have contributed to this. However, we do not know how long the citrate persisted on the surface of the ceria ENM or if was covered (opsonized) by proteins. The rapid clearance of metal/metal oxide ENMs from blood has been reported previously.

Little has been reported about the fate of systemic cerium, other than it is very slowly eliminated, primarily in bile, resulting in prolonged retention in mammals, primarily in the liver and skeletal system (219, 220). Our pharmacokinetic results showed that the cerium ion had a smaller Vd_{ss} than the 5-nm ceria ENM. It also showed less retention in reticuloendothelial tissues, but more in the lung (27). All the ceria ENMs showed a large Vd_{ss} indicating great distribution in tissues, consistent with the intracellular agglomerations we have seen, especially in reticuloendothelial cells (179). Ceria ENMs have been seen in the cytoplasm of brain cells, phagosomes of macrophages, vesicles of lung fibroblasts, spleen red pulp, Kupffer cells, hepatocytes and mesangial cells (7, 71, 221-224). Thirty days after ceria ENM infusion the greatest concentration was seen in the reticuloendothelial tissues, including liver and spleen (7, 32, 224). It was reported that lung, heart, and brain cerium did not decrease over 6 months following iv ceria ENM dosing (221). A study with the 30-nm ceria ENM used in the present study showed no significant decrease of ceria in 14 tissues up to three months after iv administration. The highest concentrations were in reticuloendothelial tissues (spleen, liver and bone marrow), followed by the lung, then other sites (27). We are not aware of any reports of

ceria uptake into red or white blood cells or platelets other than our prior finding suggesting a small amount of a 30 nm ceria ENM might have entered red blood cells after 1 h *in vitro* (7). It is unclear if the ceria ENMs would ever reach a constant blood level. Up to the times studied in the present report, there was generally a decrease of blood cerium. Given the persistence of ceria in the rat, one might expect a steady state to be reached. However, 90 days after ceria infusion blood cerium concentration was higher than earlier times (27).

The cerium ion was equally distributed between serum and clot fractions. A previous study reported that 2 h after iv cerium ion administration ~ 28% of the cerium in the blood was in cells and 72% in serum (225), similar to results in the present study that showed ~ 70% in the serum fraction at 2 h. The distribution of ceria ENMs between serum and clot varied with size and surface chemistry. The 5-nm ceria was evenly distributed within the serum and clot fractions. We previously observed small agglomerations of the 5-nm ceria in serum, presumably associated with proteins, and agglomerations associated with the extracellular side of the erythrocyte cell membrane after 1 h of incubation of the ceria in blood (224). The ability of ENMs to enter erythrocytes, a non-phagocytic cell, has been observed for 78 nm polystyrene, 25-nm gold, and 22-, 25- and 80-nm titania ENMs (226-228). However, we are not aware of any studies of ceria ENM or other metal/metal oxide ENMs entry into white blood cells or platelets.

Although the extent of citrate coating might be expected to influence the fate of ceria ENMs *in vivo*, the present results show no clear trends between the extent of citrate surface coating and ceria ENM distribution between serum and the clot fraction initially, or over time. For the cerium ion, and 5- and 55-nm and the mixture of 30-nm cubic + rod ceria ENMs, we were unable to identify any trends in the percentage of Ce in the serum vs. time.

The blood levels of the 15- and 30-nm ceria ENMs increased over the 4 h after their infusion. As they were given by the iv route, this suggests a re-distribution of the ENM over time. Re-distribution of ENMs has been previously recognized and discussed, e.g. (229). An increase of ENM in blood within the first 2 h after iv administration has been reported, although the increases appear to be within the variability of the reported measure of the quantum dots in plasma or blood and neither report discusses the increase (230, 231). The increase we saw may be influenced by protein corona and/or distribution into and out of a non-central compartment, such as the lymphatic system, as noted by (232). We also observed that the distribution of the 15- and 30-nm ceria ENMs within blood compartments changed over the 4 h after completion of their infusion, when they became more associated with the cells in the clot fraction. These results suggest their surface chemistry changed during that period, which may be due to dissociation of the citrate, association with proteins or blood cells, and/or cell entry and release. Nanoscale materials are rapidly coated with plasma proteins and other circulating substances, which create a corona around the ENM, increasing their hydrodynamic size (163, 180). It has been shown that citrate-coated ENMs bind to the surface of cells (102) and can become

opsonized with albumin (233). We speculate that the increase of the 15- and 30-nm ceria ENMs in circulating blood and migration toward the clot fraction during the first 4 h after their iv infusion is due to distribution out of, then back into, circulating blood, perhaps associated with protein corona. This might be due to initial accumulation in blood vessels or adsorption onto the luminal surface of vascular endothelial cells, followed by protein modification and re-circulation in blood. However, we would not anticipate extensive accumulations of ceria blocking the vasculature in the absence of cardio- and cerebrovascular incident (MI and stroke) which we have not observed in these rats that generally tolerated the target doses well. Or the ceria ENMs may have distributed outside of the vascular compartment, such as entrapment by reticuloendothelial organs followed by their release back into blood, or entry into the lymphatic system, that drains into the cardiovascular system. Particles up to 50 nm are able to rapidly enter the lymphatic system (234, 235). From the results of the present study we do not have evidence of the origin of the ceria ENMs that re-entered circulating blood during the first 4 h after their infusion. However, we have seen a net migration of Ce following 30-nm ceria ENM administration from liver to spleen from 1 to 20 h after its infusion (181) and into lung over 90 days, consistent with re-distribution of this ENM over time (27). As > 98% of the ceria dose was no longer in circulating blood when we started blood sampling 10 min after completion of the ceria infusion, the long terminal half-life and MRT and large Vd_{ss} for the 5, 15 and 30 nm ceria ENMs, based on blood levels to 30 days, may describe the very small fraction of the ENMs that had not yet distributed out of blood and/or ceria re-distributing among storage sites. This speculation is based on the retention of a very large percentage of the ceria ENM dose for a long time in the rat and evidence

we (and others) have of re-distribution among sites over time. Similarly, there may have been some re-distribution of the 5 nm ceria which was not seen above the much higher level of ceria remaining in blood from the infusion during the first 4 h after its infusion.

The non-compartmental analysis could not estimate some of the pharmacokinetic parameters for the 15 and 30 nm ceria ENMs probably because of the ceria concentration increase at the first 4 h. Due to the lack of prior studies of metal and metal oxide ENMs in blood, further studies of citrate-coated ceria ENMs are necessary to better understand their fate in the vascular compartment, including the stability of the citrate coating; their interaction with cell membranes; and the rate, extent and character of protein association.

The mean residence time (MRT) typically indicates the average time molecules stay in the body. In our study, the MRT indicated how long ceria ENMs remained in blood, not in the tissues, because MRT is derived from measurement of ceria (as Ce) in blood (236). It has been previously noted that the blood half-life of an ENM may be short despite prolonged body persistence, due to reticuloendothelial system entrapment and other processes not typical of small inorganic and organic molecules (209). Non-compartmental and compartmental analyses produced quite different MRT results, although the trends among the tested materials are similar across analysis. The lower MRT values with the non-compartmental analysis may be due to its tendency to underestimate MRT (237). Knowing that there are persistent accumulations of ceria ENMs in multiple organs suggests the MRT results from the compartmental analysis more closely reflects the whole body residence time of ceria ENMs. The results of the

present pharmacokinetic calculations that one can have the most confidence in are those obtained following infusion of the cerium ion and the 5-nm ceria ENM, due to the very rapid clearance of the larger ENMs from circulating blood and the rise in Ce concentration over 4 h following 15- and 30-nm ceria ENM infusion. Although the results obtained with the cerium ion and 5, 15 and 30 nm ceria ENMs clearly show two compartments, the values for the second compartment do not have a high degree of precision due to the limited number of data points on which they are based.

It has been previously noted that some of the properties of ENMs, e.g., protein coating, adhesion, and phagocytic uptake, may differ from small organic molecule disposition for which pharmacokinetic modeling programs such as WinNonLin were created (209). Pharmacokinetic and PBPK approaches have been used to model ENM distribution among tissues and blood (232, 238). Most nanomaterials do not exhibit ADME profiles typical of drugs (239), e.g. they are rapidly cleared from the blood, not metabolized, and not rapidly eliminated, unless small enough to be filtered by the renal glomerulus. It has been recognized that the toxicokinetics of ENMs are unlikely to follow the "rules" of current approaches (240, 241). Further work is needed to develop a pharmacokinetic model to predict the time-dependent changes of ceria ENM distribution in tissues and blood.

There is considerable literature on the pharmacokinetics of polymer ENMs due to the extensive research in developing them as drug delivery systems. Much less is known about the pharmacokinetics of metal and metal oxide ENMs; particularly their

distribution, residence time, and rate of clearance from the vascular compartment. The present study informs about the effects of ENM physicochemical properties on distribution and clearance from blood. The results show ceria ENMs have a biodistribution and clearance pattern which cannot be predicted from the cerium ion. This may be due to the very different physicochemical properties of the cerium ion and ceria ENMs.

3.5. Conclusions

To better understand the fate of ceria as a model ENM we compared the distribution within, and rate of clearance from, blood of four different sizes of cubic or polyhedral ceria nanoparticles, a mixture of cubes and rods, and the cerium ion after iv infusion into rats. Table 3.3 summarizes the main findings of the present study. The kinetics and distribution of the cerium ion did not predict those of the ceria ENMs. A 5-nm ceria ENM, which was very resistant to agglomeration and settling *in vitro*, was cleared much more slowly from blood than larger ceria ENMs, presumably because it was too large to be cleared by glomerular filtration and perhaps too small or too hydrophilic to be readily recognized by the reticuloendothelial system. Ceria ENMs larger than 5 nm were very rapidly cleared from circulating blood. All the ceria ENMs had a much greater Vd_{ss} than the cerium ion, consistent with their extensive distribution and prolonged retention throughout the rat. The 15 and 30 nm ceria ENMs showed concentration ratios increasing vs. cerium ion over 4 h after infusion. The distribution of ceria ENMs between serum and the blood clot was size dependent. The citrate-coated 30-nm ceria showed the greatest distribution in the clot fraction. The fraction of 15 and 30 nm-ceria ENMs in the clot fraction increased over 4 h, suggesting a change in their surface properties, perhaps

due to protein corona. A further understanding of the rate and nature of ceria ENM association with blood proteins and cells, and the process(es) of their clearance from blood, is needed to fully interpret their fate in the vascular compartment.

Table 3.3. The whole blood compartment model, serum and clot partitioning, and ceria ENM vs. cerium ion ratio results of the six materials studied.

Material	**Compartment modeling**	$R = \frac{[Ce]_{ceria}}{[Ce]_{cerium(ion)}}$	**Serum/whole blood partitioning**
Cerium ion	Fits the two compartment model	Not applicable	No strong trend
5 nm ceria	Fits the two compartment model; longer persistence in the second compartment than the cerium ion	Time-dependent reduction in [Ce] relative to the ion; 1st order or other process possible	No strong trend
15 nm ceria	Rapid loss during infusion; Apparent re-distribution to blood in 2-4 hours	Increase relative to $[Ce]_{ion}$; 1st order process	Reduction in serum levels with time; 1st order process (protein corona?)
30 nm ceria	Rapid loss during infusion; Apparent re-distribution to blood in 2-4 hours	Increase relative to $[Ce]_{ion}$; 1st order process	Reduction in serum levels with time; 1st order process (protein corona?)
Cubic + rod ceria	Loss during infusion; Apparent redistribution to blood in 2-4 hours	No strong trend	No strong trend; less than 50% in serum
55 nm ceria	Rapid loss during infusion; No apparent re-distribution to whole blood in 2-4 hours	No strong trend	No strong trend

3.6. Unsolved problems

This study gave us a better understanding of pharmacokinetics of different sized ceria ENMs in blood. Traditional pharmacokinetic modeling showed the best fit for 5-nm ceria ENM and the cerium ion. Ceria ENMs larger than 5 nm were rapidly cleared from blood. After initially declining, whole blood 15- and 30-nm ceria increased; results not well-described by traditional pharmacokinetic modeling. One possibility is that ceria ENMs associated with the blood vessel and dissociated over time due to protein corona. Following the distribution in and clearance from blood, the ceria ENM blood vessel association and moving out of the vascular compartment will be the next crucial step influencing their fate in biological systems. In the next chapter, the BBB was chosen to investigate the association and flux of ceria ENMs across this biological barrier using the *in situ* brain perfusion method.

Reproduced with permission from Dan M, Wu P, Grulke EA, Graham UM, Unrine JM, Yokel RA. Ceria engineered nanomaterial distribution in and clearance from blood: Size matters. Nanomedicine, 2012, 7(1), 95-110. Copyright © Future Medicine Ltd. Dan M and Yokel RA drafted the published paper. Author's contributions: Dan M did the most of pharmacokinetic studies including modelling and animal studies. Wu P synthesized and characterized the ceria ENMs except 55 nm ceria. Grulke EA helped with the pharmacokinetics model and revised the paper critically. Graham UM synthesized the 55 nm ceria. Unrine JM analyzed all the samples using ICP-MS.

Chapter 4 Brain microvascular endothelial cell association and distribution of a 5 nm ceria engineered nanomaterial

In this chapter, we will test our hypothesis that a 5 nm ceria ENM can associate with brain capillary cells and enter the brain. The study will provide important information on how ceria ENMs associate with endothelial cells, which is the first step for its cell uptake or redistribution back into circulating blood. This is the first report on how ceria ENMs distribute between the BBB and the brain parenchyma. The results will show the potential biomedical applications in the CNS and provide explanation for the nontraditional pharmacokinetics profile of ceria ENMs.

4.1. Introduction

Our previous findings showed 5 nm ceria ENM agglomerates in the brain capillary lumen. Electron microscopy did not reveal ceria ENM inside microvascular endothelial or brain cells. Ceria ENMs did not produce profound pro- or anti-oxidant effects in the brain 1 or 20 h after a one h systematic intravenous infusion (8). The reasons for the lack of ceria ENM in the brain were unknown. One possibility is that the protein corona in the blood that changed ceria ENMs physicochemical properties, resulting in their rapid clearance by the MPS (180, 181). Nanoparticles agglomerated very rapidly in the blood or on a biological surface, changing their distribution and cell interaction (78, 182-184), so that the agglomerated ceria became too large or unavailable to penetrate the intact BBB. The present study utilized a controlled system to better understand how ceria

ENMs interact with brain capillary endothelial cells. The results are relevant to the therapeutic use and toxicological consideration of ceria ENMs.

The objective of this study was to investigate the brain capillary cell association and brain entry rate of a 5 nm ceria ENM. We used the *in situ* brain perfusion method to evaluate BBB integrity and determine brain entry rate at different perfusion flow rates, ceria ENM concentrations and perfusion durations. Eight brain regions and a choroid plexus were collected to test regional differences in BBB integrity and ceria ENM brain entry rate. The capillary depletion method was used to evaluate ceria ENM distribution between capillary and brain tissues. The localization of ceria nanoparticles was investigated by LM and EM.

4.2. Materials and Methods

4.2.1. Materials

The chemicals used to prepare the ceria ENMs have been described (242). Cerium chloride heptahydrate (Sigma-Aldrich #228931, 99.9% metal basis), ammonium hydroxide (Fisher # 3256, ACS, 28-30%), deionized ultra filtered water (Fisher #W2-20), and citric acid monohydrate (EMD Chemicals Inc # CX1725-1, GR ACS) were used without further purification. All other chemicals were purchased from Sigma-Aldrich (St. Louis, MO) unless otherwise noted.

4.2.2. Ceria ENM synthesis

Synthesis of the 5 nm ceria ENM was described (224). It was synthesized using a hydrothermal method (213) that produces monodisperse nanoparticles directly in the reactor. Typically, a 20-ml aqueous mixture of 0.5 M (0.01 mol) ceria chloride and 0.5 M (0.01 mol) citric acid was added to 20 ml of 3 M ammonium hydroxide. The latter was in excess of that needed for complete reaction of the cerium chloride to cerium hydroxide. After stirring for 24 h at 50 ºC, the solution was transferred into a Teflon-lined stainless steel bomb and heated at 80 ºC for 24 h to complete the reaction. Ceria ENM was citrate coated (capped) to improve their dispersity in water to stabilize dispersion through electrostatic repulsion to prevent the agglomeration seen with uncoated ceria that occurs in high ionic strength solutions, such as blood (102, 103, 243). Citrate was selected because it is a commonly used surface coating agent for ENMs to inhibit agglomeration (e.g., NIST's reference materials 8011, 8012 and 8013), is a component of blood (present at ~ 100 µM in humans), might coat bare ENMs circulating in blood, has been shown to have no effect on erythrocyte response to a silver ENM, and citrate-coated ENMs interact strongly with proteins, resulting in the rapid protein corona that occurs when ENMs enter blood (233, 244, 245).

4.2.3. Ceria ENM characterization

The physico-chemical properties of the ceria ENMs were determined in our laboratories. Most of the methods have been reported (242). Primary particle size distributions were determined by TEM and scanning transmission electron microscope (200-keV field emission analytical transmission electron microscope, JEOL JEM-2010F, Tokyo, Japan). From the individual primary particle sizes measured from TEM images, number

frequency cumulative distributions were constructed. These cumulative distributions were best described by log-normal distribution models, characterized by a sample mean and its standard deviation. All of these data sets were well-described by a single mono-modal distribution, that is, one continuous distribution was observed, and no significant secondary or tertiary peaks were noted. The reported 'average' diameter of each sample was $D_{ave} = \exp(\mu)$, where μ is the mean of the log-normal probability distribution, and the reported 'standard deviation (S.D.)' is the value from the fit of the log-normal distribution to the data. For each sample, number-based differential frequency distributions were constructed using the model coefficients. The particle size distributions (PSDs) for each batch of as-synthesized ceria aqueous dispersion were determined using dynamic light scattering (DLS; 90Plus NanoParticle Size Distribution Analyzer; Brookhaven Instruments Corporation, Holtsville, NY). Zeta potential of the ceria ENMs dispersion as infused into the rat was estimated from electrophoretic mobility measurements using a Zetasizer nanoZS with a typical ceria concentration ~0.02 wt% (Malvern Instruments, Worchestershire, UK). Because the particles had hydrodynamic diameters < 200 nm, the Hückel approximation was used to calculate zeta potential from electrophoretic mobility. The surface area of the dried powder was determined using a BET surface area analyzer (Micromeritics Instrument Corporation, Norcross, GA, USA). Thermogravimetric analysis (Perkin-Elmer TGA7 Analyzer) was then performed to investigate the weight loss of citrate-coated ceria NPs over the temperature range of 150 to 300°C under which decomposition of citric acid occurs. The extent of citrate surface coating was estimated based on the assumption that all the ceria NPs were spherical and had uniform size.

4.2.4. Nanomaterial

The 5 nm ceria ENM was synthesized using a previously reported method (8). The physico-chemical properties of the ceria ENMs were determined in our laboratories. Free cerium in the ceria ENM dispersion was removed by ultrafiltration using 3 kDa molecular weight cutoff regenerated cellulose centrifugal filtration devices (Amicon Ultra-4, Millipore). The 5 nm ceria (3.5 ml) was added to the Amicon Ultra Filter unit. The unit was centrifuged at 4800 g for 35 min to obtain 3 ml filtrate and 0.5 ml concentrated ceria ENM. The 3 ml filtrate (containing free cerium) was removed from the centrifuge tube. Three ml sodium citrate (0.17 M) solution was added to the filtration device to disperse the ceria ENM. After conducting this washing procedure 3 times, sodium citrate solution (3 ml; 0.17 M) was added to the filtration device which was bath sonicated for 15 min to redisperse the ceria ENM. The Ce concentrations of the 5 nm ceria ENM dispersion and free cerium in the ultrafiltrate were analyzed by ICP-MS (8, 242).

4.2.5. Perfusate for in situ brain perfusion

The perfusate contained 30, 100 or 500 µg/ml ceria ENM in a solution of Na^+ (153 mM), K^+ (4.2 mM), Ca^{2+} (1.5 mM), Mg^{2+} (0.9 mM), Cl^- (162 mM) and glucose (9 mM). Gadolinium-diethylenetriaminepentaacetic acid (Gd-DTPA) (1 mM) was added to determine BBB integrity. Gd-DTPA, a marker for vascular space, has been shown to not significantly cross the intact BBB because of its charge and high molecular weight (246). A significant increase of Gd-DTPA in brain samples indicates BBB damage. Following

at least 1 h incubation at 37°C, the perfusate was bubbled for 2 min with 95/5 air/CO_2 and adjusted to pH 7.4 prior to its use (247).

4.2.6. Ceria ENM stability in the perfusate

Ceria ENM stability in the perfusate was determined from 1 to 230 min (after addition to perfusate) using dynamic light scattering (DLS) (90Plus Nanoparticle Size Distribution Analyzer, Brookhaven Instruments Corp, Holtsville, NY). The intensity-weighted hydrodynamic diameter in the perfusate was measured at 1000 µg/ml at 37 ºC, and then converted to number- and volume-weighted averages.

4.2.7. Animals

This study used 55 male Sprague-Dawley rats, weighing 330 ± 35 g (mean ± SD), that were housed individually prior to study in the University of Kentucky Division of Laboratory Animal Resources Facility. Animal work was approved by the University of Kentucky Institutional Animal Care and Use Committee (Protocol 2008-0272). The research was conducted in accordance with the Guiding Principles in the Use of Animals in Toxicology.

4.2.8. *In situ* brain perfusion methods

We employed the modification of the brain perfusion technique that we previously reported (247-249). Briefly, the rat was anesthetized under ketamine/xylazine anesthesia (75 and 5 mg/kg), and its left carotid artery exposed. Following ligation of the external carotid, occipital and common carotid arteries, PE60 tubing containing heparin (100

U/ml, in 0.9% NaCl) was inserted into the common carotid. We used the heart-cut modification of this technique and increased the perfusate flow rate to 20 ml/min (250). The rat was decapitated to end the perfusion. The brain was harvested and cleaned of meninges and surface vessels. Brain tissue (~ 20 mg from each brain region except the choroid plexus, which averaged 0.9 ± 0.4 mg) was collected from the frontal cortex, parietal cortex, occipital cortex, thalamus/hypothalamus, midbrain/colliculus, striatum, cerebellum, hippocampus, and choroid plexus from the left hemisphere for measurement of Gd-DTPA (as gadolinium) and ceria ENM (as cerium) by ICP-MS. Cerebrovascular washout of perfusate was conducted to test the influence of ceria concentrations in the vascular space on the brain uptake space. The cerebrovascular space was washed at the same perfusion rate (n = 4 rats) for 20 s with ceria-free perfusate immediately following 100 µg ceria ENM/ml perfusion for 120 s at 20 ml/min. The results were compared to those obtained without cerebrovascular washout using a two-way ANOVA. The brain uptake space in the washout and non washout conditions did not show significant differences after correcting for the vascular volume. Therefore, the rest of the studies did not conduct washout except the capillary depletion experiment and 3 rats perfused for LM and EM examination.

Flow-rate dependent uptake is a property of some carrier-mediated uptake systems, but is not a property of diffusion (247). Therefore, to examine the effect of perfusion flow rate on influx rate and the vascular and brain extracellular fluid volumes, 15 and 20 ml/min flow rates (100 µg ceria ENM/ml) were tested in 4 and 5 rats, respectively. To determine whether ceria ENM brain entry is concentration dependent, 3 ceria ENM concentrations

(30, 100 and 500 µg/ml) were investigated using a perfusion rate of 20 ml/min and duration of 120 s (n = 4, 6 and 5 rats, respectively). Ceria ENM brain entry during different perfusion durations was investigated to determine how fast ceria ENM associates with brain capillary cells or enters the brain. Perfusion durations of 20, 60 and 120 s, using a rate of 20 ml/min, and 30 µg ceria ENM/ml were studied in 4 treated animals and 3 control animals in each group. Three animals were prepared for LM and EM after perfusion with 100 µg ceria ENM/ml, 20 ml/min for 120 s, followed by 20 s washout with ceria-free perfusate.

4.2.9. Capillary depletion method

The capillary depletion method was used to separate brain parenchyma from capillary tissue (247, 251). After a 30 µg/ml, 120 s, 20 ml/min ceria ENM perfusion, a 20 s washout was conducted. The forebrain from perfused hemisphere was isolated from 10 rats (2 control and 8 treated) and the lateral ventricle choroid plexus in the perfused hemisphere was removed. The tissue was homogenized in 3.5 ml physiological buffer containing 141 mM NaCl, 4 mM KCl, 2.8 mM $CaCl_2$, 1 mM NaH_2PO_4, 1 mM $MgSO_4$, 10 mM glucose and 10 mM HEPES at pH 7.4. Dextran (70,000 g/mol) was then added to 18% (w/v) and the sample further briefly homogenized. After centrifugation at 5400 x g for 15 min at 4 ºC, the supernatant (brain rich fraction) and pellet (capillary rich fraction) were carefully separated for measurement of ceria ENM by ICP-MS. The percentage of the forebrain ceria ENM in the capillary rich fraction = mass amount of cerium in the capillary rich fraction / mass amount cerium in the capillary rich fraction plus brain rich fraction. The percentage of the ceria ENM dose in the capillary rich fraction = mass

amount of cerium in the capillary rich fraction / mass amount cerium in the total ceria ENM dose

4.2.10. Cerium and gadolinium analysis

Cerium and gadolinium were analyzed by ICP-MS (Agilent 7500cx, Santa Clara, CA, USA) as previously described (7, 224). The method detection limits of Ce and Gd in tissue were 0.013 mg Ce/kg and 0.0004 mg Gd/kg, respectively.

4.2.11. Light and electron microscopy

Rats were decapitated at the end of the in situ-washout perfusion for brain removal. After bisection, each hemisphere was immediately immersed in a fixative containing 2% paraformaldehyde-2% glutaraldehyde in 0.1 M cacodylate buffer for 24 h at 4 ºC. Tissue samples from pituitary gland, hippocampus, and choroid plexus were identified with the aid of a dissecting microscope, and stored in 0.1 M cacodylate buffer. Samples were cut to approximately 3 mm^3 before being dehydrated in ascending concentrations of ethanol and embedded in Araldite 502. After polymerization, blocks were sectioned at one micron thickness, toluidine blue stained for screening, and selected blocks sectioned at 80 nm thickness for TEM viewing in a Philips CM 10 electron microscope operated at 80 kV.

4.2.12. Data and Statistical Analysis

The distribution volume, or uptake space (Q), derived from the *in situ* brain perfusion results, is the amount of brain tissue into which the substrate distributes during a given perfusion duration. $Q_{\text{ceria total}}$ (ml/g) = ceria ENM in tissue (µg/g) / ceria per volume of perfusate (µg/ml) (252). The mass amount of ceria ENM per gram of brain (µg/g) was also calculated in order to compare the results of perfusion of the 3 ceria ENM concentrations. Gd-DTPA uptake space (vascular and extracellular space) was used to correct the ceria ENM brain uptake space results (247). $Q_{\text{Gd-DTPA}}$ = Gd-DTPA in tissue (µg/g) / Gd-DTPA per volume of perfusate (µg/ml). Corrected brain $Q_{\text{ceria ENM}} = Q_{\text{ceria total}} - Q_{\text{Gd-DTPA}}$. The corrected mass amount of ceria ENM per gram of brain (µg/g) = $(Q_{\text{ceria total}} - Q_{\text{Gd-DTPA}})$ (ml/g) X ceria per volume of perfusate (µg/ml). Grubbs' test was used to determine outliers. Bartlett's was used to test if samples have equal variances. Two - way ANOVA followed by Bonferroni multiple comparisons was used to test for significant differences among Gd-DTPA concentrations at 15 ml/min and 20 ml/min (treated and control) flow rates and among the nine regions. Two - way ANOVA followed by Bonferroni multiple comparisons was also used to test for significant differences among three concentration groups of ceria ENMs and the nine regions or among three infusion times of ceria ENMs and the nine regions (GraphPad Prism Version 3.00 for Windows, GraphPad Software, San Diego, CA). The results of the statistical analysis for two-way ANOVA will be reported as F(df (degrees of freedom) effect, df error) = F-value and P-value. The percentage of the capillary surface area that would be covered by ceria ENMs was calculated as = (the number of ceria ENM particles in the perfused hemisphere X one ceria particle cross sectional area)/the rat brain capillary endothelial cell surface area.

This was based on the ceria average diameter, the ceria density = 7.132 g/cm^3 and the rat's capillary surface area = 140 cm^2/g brain (253). All results are reported as mean ± SD.

4.3. Results

4.3.1. Nanoparticle characterization

The ceria ENM was polyhedral. The X-ray diffraction pattern showed the ceria to be highly crystalline. It was face centered cubic with corresponding Miller indices of the most common faces of (111), (220), and (311). Evaluation of a number of TEM images (Figure 4.1A) showed that D_{mean} (average primary particle diameter from number frequency distribution) and standard deviation based on TEM measurements of diameter fitted using lognormal distribution models was 4.6 ± 0.1 nm. DLS results of a representative batch of as-synthesized ceria dispersion showed that 98 percent of the particles were in the range of 6.7 - 8.2 nm (Figure 4.1B). Zeta potential was -53 ± 7 mV at pH ~ 7.35 in water. The ceria ENM surface area was 121 m^2/g. The extent of surface citrate coating was ~ 40% (8). Five percent free cerium ions were in the as-synthesized ceria ENM. After the 3 filtrations, less than 0.05 % of the ceria ENM perfusate was free cerium ions. Ceria ENM was stable in the perfusate at 37 ºC: no apparent agglomeration was observed from 1 to 230 min. The particle size of the ceria ENMs was within +/- one standard deviation after addition of the ceria ENM to the perfusate (Figure 4.2). The stability of the ceria ENM in the perfusate is crucial for this experiment to understand how the ceria ENM interacts with capillary cells and brain tissue.

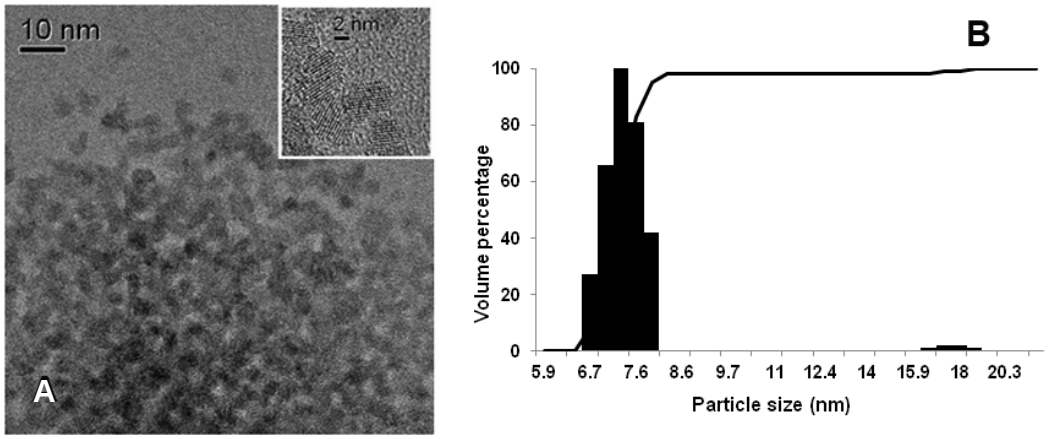

Figure 4.1. Ceria ENM morphology. **(A)** Ceria ENM imaged using TEM. The insert at the top right shows the crystallinity of the ceria ENM. **(B)** Volume-based particle size distribution for ceria ENM of a representative batch of as-synthesized ceria aqueous dispersion.

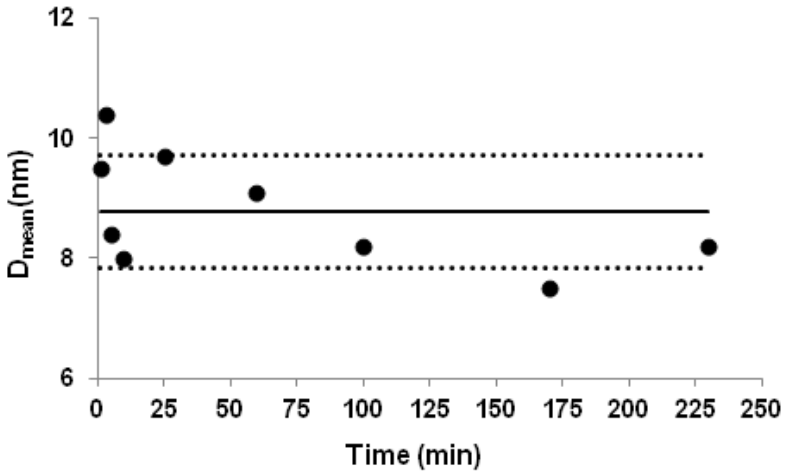

Figure 4.2. Ceria ENM hydrodynamic diameter in perfusate. Hydrodynamic diameter (intensity weighted average) of ceria ENM in the *in situ* perfusate from 1 to 230 min (1000 µg/ml at 37 ºC) after ceria was added to the perfusate. Solid circles are DLS data and black solid line is the average of all the data. Dotted lines represent the position of average diameter +/- one standard deviation.

4.3.2. Flow rate dependency

Comparison of uptake space ($Q_{ceria\ ENM}$) using 15 and 20 ml/min flow rates did not show a significant flow rate effect on brain ceria ENM uptake in any of the 8 brain regions or

the choroid plexus. Furthermore, there was no significant difference in the vascular space with these 2 flow rates or between control and treated groups. However, the choroid plexus showed a significantly higher vascular space than the 8 brain regions ($F(8,144) = 12$, $P < 0.0001$) (Figure 4.3). The brain vascular space results were similar to those we measured using [^{14}C]-sucrose (247). A 20 ml/min flow rate was used for the rest of study.

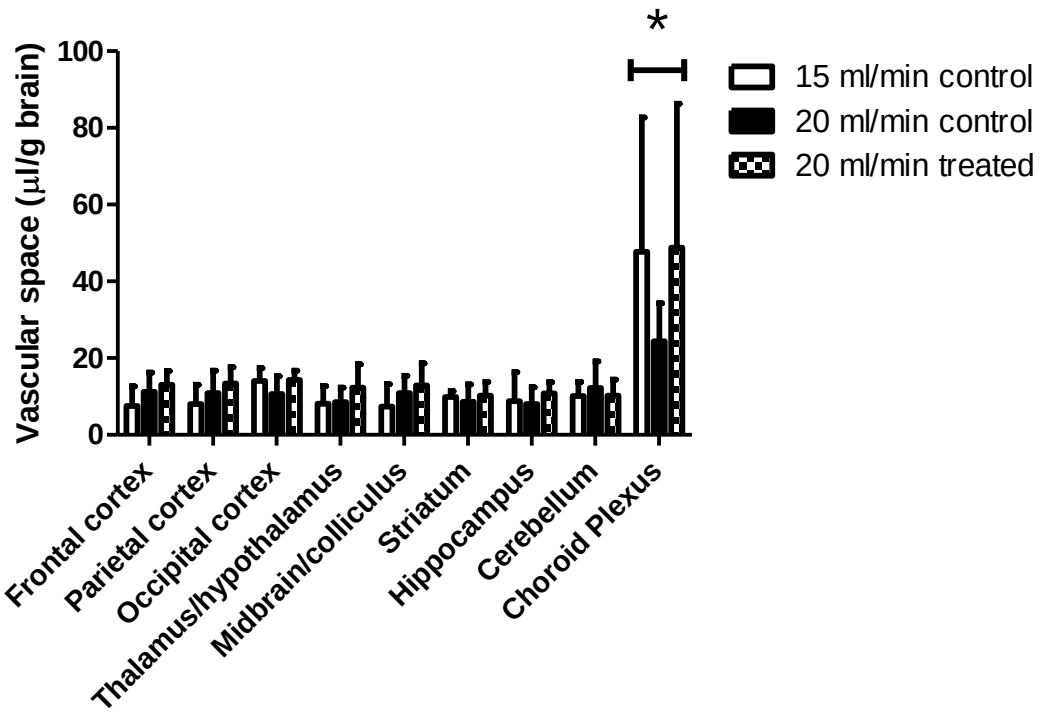

Figure 4.3. Vascular space of the brain as measured by Gd-DTPA at 15 (n=4) and 20 (n=5) ml/min flow rate in control rats and 20 (n=10) ml/min flow rate in 5 nm ceria treated rats.
* Significantly different from 8 brain regions, $F(8,144) = 12$, $P < 0.0001$.

4.3.3. Ceria ENM uptake

To investigate the 5 nm ceria brain entry rate, its uptake space ($Q_{ceria\ ENM}$) was determined for each brain region for each of the 3 ceria perfusate concentrations. Figure

4.4A shows the uptake space significantly decreased with the increase of ceria ENM concentration in the perfusate ($F(2,108) = 118$, $P < 0.0001$). In the 30 µg/ml group, there were no significant differences among the nine regions. However, in the 100 and 500 µg/ml groups, choroid plexus uptake space was significantly higher than in the 8 brain regions. In order to compare ceria ENM uptake among the three concentrations, we calculated the mass amount of ceria uptake into the brain as µg/g (Figure 4.4B). There were no significant differences among the 3 treatment concentrations. The mass amount of ceria in the choroid plexus uptake space was significantly higher than in the 8 brain regions and also significantly higher in the 100 and 500 µg/ml groups compared to the 30 µg/ml group. The average mass amount of ceria per brain hemisphere (0.85 g) (excluding choroid plexus) was 4.2 ± 0.7 µg. To verify whether the uptake space of ceria ENM rapidly saturates ceria uptake space was determined for 30 µg ceria ENM/ml for 20, 60 and 120 s perfusion durations. There were significant increases of uptake space to multiple brain regions from 20 to 60 s ($F(2,81) = 9$, $P < 0.0004$) but no differences between 60 and 120 s, suggesting the uptake space of this ceria ENM saturated between 20 and 60 s (Figure 4.4C). The increased uptake space of the 5 nm ceria ENM showed that the ceria ENM either associated with capillary endothelial cells or entered the brain. In the next step, ceria ENM distribution between cerebral capillary cells and brain parenchyma was determined.

4.3.4. Isolation of cerebral capillaries

Cerebral capillaries were isolated from brain parenchyma to investigate the distribution of ceria ENMs between these two fractions. Less than 0.4% of the perfused ceria ENM

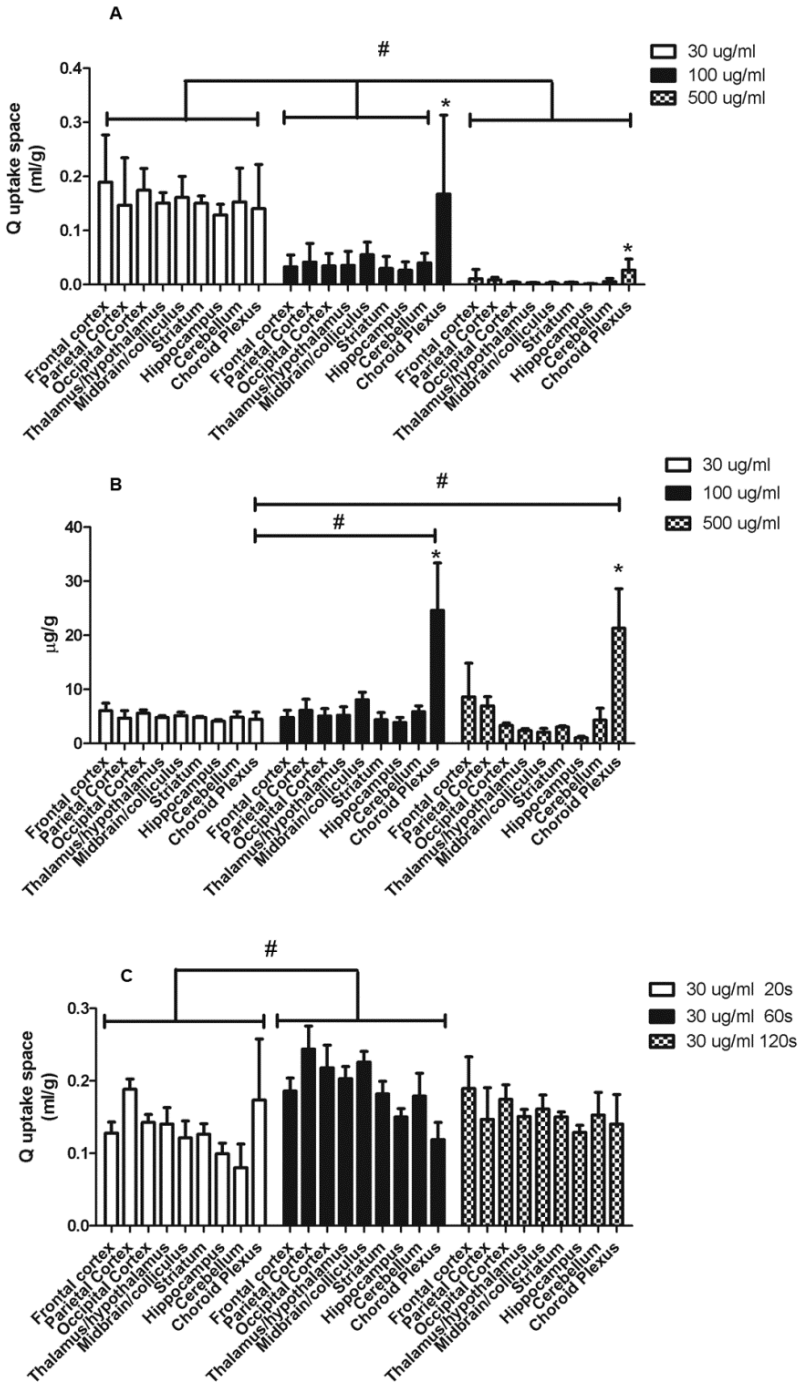

Figure 4.4. Ceria ENM uptake space at three concentrations and perfusion duration times. Effect of ceria ENM concentration and perfusion duration on its uptake. **(A)** Q uptake space (ml/g) of a 5 nm ceria ENM in 8 brain regions and the choroid plexus for 3

concentrations, at a flow rate of 20 ml/min, and 120 s perfusion duration. **(B)** Mass amount (µg/g) of 5 nm ceria ENM in 8 brain regions and the choroid plexus after brain perfusion with 3 ceria concentrations, at a flow rate of 20 ml/min, and perfusion duration of 120 s. **(C)** Q uptake space (ml/g) of 5 nm ceria ENM in eight brain regions and choroid plexus after 20, 60 and 120 s perfusion at 30 µg/ml, at a flow rate of 20 ml/min. Figure 4.4A, # = significantly different among three concentration groups, $F(2,108) = 118$, $P < 0.0001$; * = significantly different compared to the 8 brain regions at the same concentration, $P < 0.05$. Figure 4.4B, # = significantly different compared to 30 µg/ml concentration group; * = significantly different compared to the 8 brain regions, $P < 0.05$. Figure 4.4C, # = significantly different between 20s and 60s perfusion duration groups, $F(2,81) = 9$, $P < 0.0004$.

dose associated with cerebral capillaries and brain parenchyma. This separation revealed that a great majority of the ceria ENM (99.4% ± 1.1% of the total ceria ENM in both the capillary rich fraction plus brain rich fraction) was associated with the capillary endothelial cells. Less than 0.003% of the ceria ENM dose was associated with the brain tissue rich fraction (Figure 4.5). These results suggest that most of the 4.2 ± 0.7 µg ceria ENM in the perfused brain hemisphere was associated with the capillary endothelial cells and very little ceria ENM passed through the endothelial cells into brain extracellular fluid or brain cells.

4.3.5. Ceria ENM localization using LM and EM

LM and EM were used to confirm BBB integrity and determine the localization of ceria ENM in the endothelial cells and/or brain tissue. Light microscopic examination of choroid plexus revealed the presence of a cuboidal epithelial cell layer surrounding a core of capillaries with some surrounding loose connective tissue. There appeared to be no

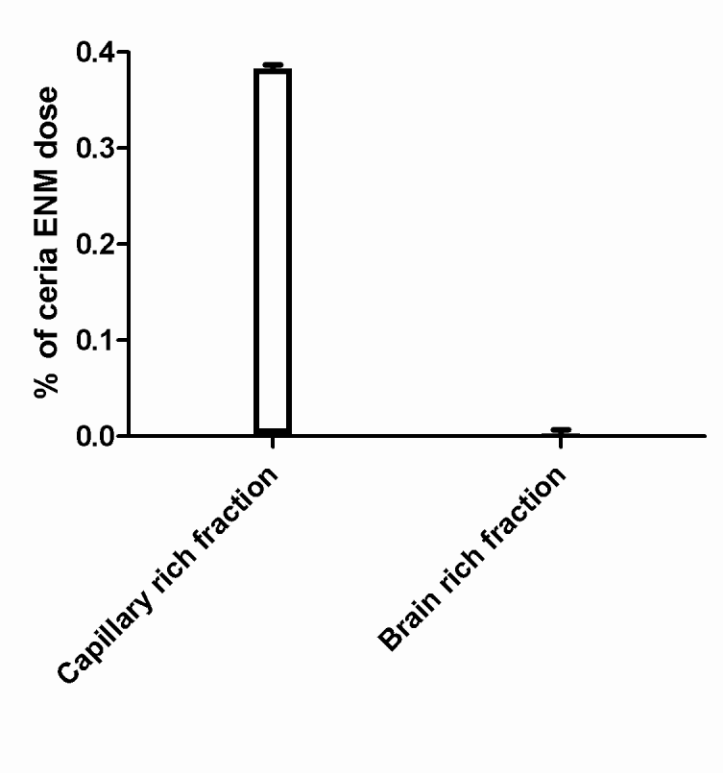

Figure 4.5. Capillary depletion results. The percentage of the ceria ENM dose in the capillary rich fraction and brain rich fraction for 100 µg/ml, at a flow rate of 20 ml/min, 120 s perfusion duration, followed by 20 s washout.

physical injury from the exposure to the high perfusate flow rate (Figure 4.6A). A capillary in the mid-CA1 region of the hippocampus is shown in Figure 4.6B. The pyramidal cells appeared unaffected by in *situ* perfusion. In the posterior pituitary, capillaries were not affected by the high perfusate flow rate (Figure 4.6C). At the ultrastructural level, the endothelial lining of the choroid plexus appeared intact (Figure 4.7A). The adjacent ependymal cell layer was lined by tightly adhering cells with well developed surface microvilli creating frond-like processes projecting into the ventricles.

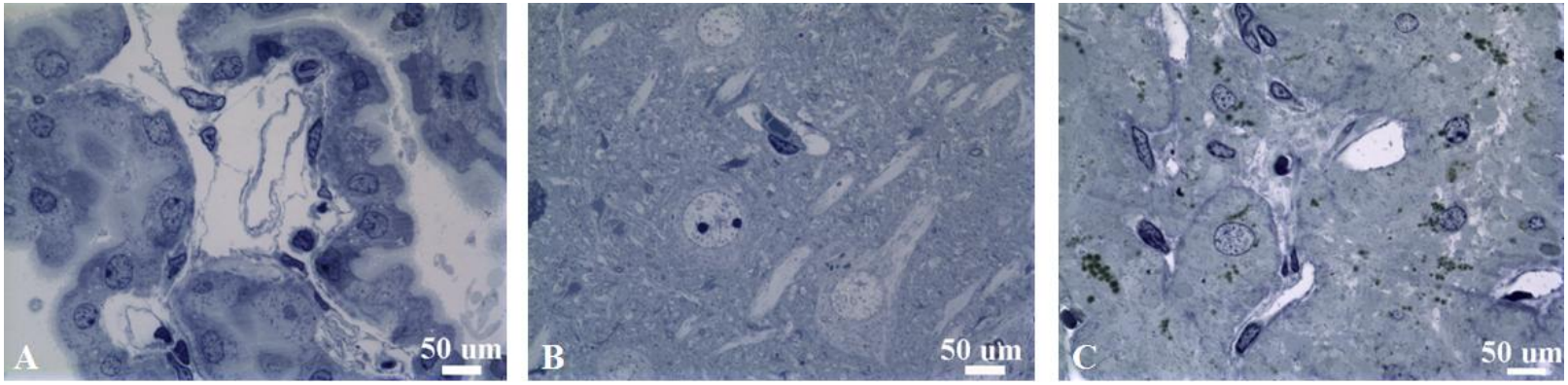

Figure 4.6. The capillaries in the choroid plexus **(A)**, hippocampus (mid-CA1 region) **(B)** and pituitary **(C)** were not affected by the high perfusate flow rate. Rats perfused with 100 µg ceria ENM/ml, at a flow rate of 20 ml/min, and perfusion duration of 120 s.

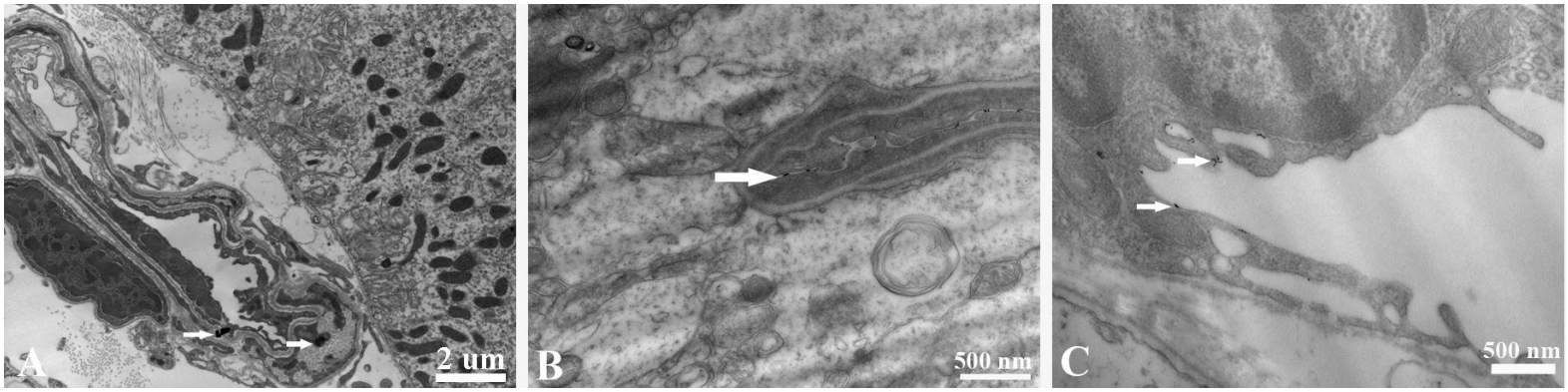

Figure 4.7. A capillary with intact endothelial lining in the choroid plexus containing two ceria ENM agglomerates (arrows) **(A)**. A vessel in the hippocampus **(B)** and a vessel from the pituitary gland **(C)** associated with fine ceria ENM (arrows). Rats perfused with 100 µg ceria ENM/ml, at a flow rate of 20 ml/min, and perfusion duration of 120 s.

Consistent with the high ceria concentration in the choroid plexus, electron dense ceria ENM agglomerations were observed on the endothelial lining (Figure 4.7A). Meanwhile, electron dense nonagglomerated ceria ENM particles adhered to the endothelial lining in the hippocampal vessels (Figure 4.7B) and the pituitary gland vessels that lack a BBB (Figure 4.7C). Ceria ENM associated with the surface of brain capillary endothelial cells. No ceria ENM was observed in any brain tissue, consistent with our capillary depletion results. The ultrastructural data lend support to the calculation that 2.4 ± 0.4 % of the luminal surface area of the capillary endothelial cells would be occupied by the 4.2 ± 0.7 µg ceria ENM per hemisphere measured in our uptake study.

4.4. Discussion

The results demonstrate that this ceria ENM did not influence BBB integrity. Perfusate flow rate and ceria ENM concentration did not influence ceria ENM uptake to brain parenchyma, providing evidence for a non-diffusion mechanism. The uptake space of the 5 nm ceria ENM did increase compared to the vascular space, leading to the conclusion that the 5 nm ceria ENM either associated with capillary endothelial cells or entered the brain. The capillary depletion method showed that most of the ceria ENM associated with the capillary cells. Association of the ceria with the brain endothelial cells was a very rapid process that saturated between 20 and 60 s using a flow rate of 20 ml/min and ceria ENM concentration of 30 µl/ml. Electron microscopy revealed the ceria ENM was associated with the capillary luminal wall and was not seen inside the brain capillary endothelial cells.

Prior to the present studies how metal or metal oxide ENMs interact with or cross the brain capillary endothelial cells was poorly understood. One of the issues relevant to how nanomaterials interact with biological membranes is that "what the cell sees" may not be the same as the ENM introduced into the study preparation (e.g., cells in culture, intact mammal in this study). Several researchers showed that ENMs agglomerate in cell culture media (22, 182). In blood, plasma proteins rapidly adsorb to nanoparticle surfaces, to form a protein corona which can change the physicochemical properties and influence the fate of ENMs (232, 254, 255). It is hard to interpret some *in vitro* and *in vivo* nanoparticle studies because of their agglomeration in cell culture media and development of the protein corona in blood. In our studies, we used a technique that does not allow the nanoparticles to mix with blood. We determined the size distribution and stability of our ceria ENM in the perfusate from 1 to 230 min. The results did not show agglomeration, which was supported by EM images that did not show significant ceria ENM agglomeration in rat brain. This is the first report of ceria ENM interaction with the BBB *in vivo* under conditions that control ENM chemistry. This research helps us to understand citrate-coated 5 nm ceria brain capillary cell association, potential brain entry and redistribution. The *in situ* brain perfusion technique is a good experimental method to investigate how the different physicochemical properties of ENMs interact with or cross the BBB in the absence of major agglomeration and a protein corona. The research will help us understand how certain physicochemical properties influence the ability of ENMs to associate with or cross the BBB for therapeutic application.

Our results showed that most of the ceria ENMs are associated with brain capillary cells rather than brain cells. Several studies showed that metal and metal oxide ENMs cross the BBB (7, 31, 256). However, without separating brain capillary cells from brain cells, it is very possible that the ENMs in those studies were associated with endothelial cells rather than entering brain parenchyma. For example, based on ICP-MS results of brain metal content, bovine serum albumin-coated silver ENM was in the brain, compared with control. Signs of silver-induced brain damage were observed. However, EM did not reveal silver ENMs in the brain (257). It is possible that the silver ENMs associated with the BBB and released silver ions to produce the toxicity rather than being an effect of silver ENMs. A previous study using the *in situ* brain perfusion method reported that polymer-based nanoparticles entered the central nervous system within 60 s without influencing BBB integrity. However, the researchers did not separate the capillary cells from the brain parenchyma. They showed an uptake space similar to results we obtained at 20 and 60 s. Capillary association may also contribute to their brain uptake space (258). Our previous studies showed only 0.02% of a 5 nm ceria dose in the brain 1 h after iv infusion. However we didn't observe any 5 nm ceria ENM in brain tissue (8). In light of the results in this paper, the 0.02% ceria in the brain may be ceria ENM in blood and associated with capillary cells. In this study, brain association (0.386% of the ceria ENM dose) using *in situ* perfusion is 19 times higher than our previous report (0.02% of the ceria dose) 1 h after iv infusion. The different timelines (in the prior study brain samples were obtained 1 h after completion of a ceria infusion; in the present immediately after completion of ceria perfusion) and routes (intravenous vs. intra-carotid artery) may contribute to the ceria ENM brain capillary association differences. In the present studies

using *in situ* brain perfusion ceria ENM did not mix with blood and avoided first pass clearance. After intravenous administration ceria ENM agglomerated in the blood and protein corona formation changed its physicochemical properties, resulting in rapid clearance by the mononuclear phagocyte system (181, 259) . Ceria ENM may associate with brain capillary cells at 120 s perfusion and dissociate over time. The above reasons may explain the high brain capillary ceria ENM association compared with our previous iv infusion study.

Our EM results showed that most of the ceria ENM is on the luminal surface of brain capillary cells rather than inside these cells. Brain capillary cell association with this negatively charged ceria ENM is in agreement with a previous kinetic study that reported a negatively charged nanoparticle associated with the cell surface within seconds by Langmuir adsorption through electrostatic interaction (260). After surface adsorption, the next step may be dissociation and redistribution or cell internalization. The time course of cell internalization of metal oxide nanoparticles is still under investigation. Anionic iron oxide ENMs attached onto the cell membrane of Hela cells immediately after ENM introduction to the cells. Early endocytic coated vesicles were observed at 10 min (260). Most of the literature we are aware of showed cell line- and material-dependent ENM internalization half lives more than a few min *in vitro* and *in vivo* (151, 260-263). Fourteen, 50 and 74 nm gold nanoparticles had uptake half lives more than 1 h in three different cancer cells (151). Flux of cationic arginine-vasopressin nanoparticles across the BBB started at 15 min though absorptive-mediated endocytosis in mice (262). Because of the nature of the *in situ* perfusion technique, perfusion duration in the present study

was not greater than 120s (252). More research will need to be done to understand what happens after the ceria ENMs interact with brain capillary cells. However, no matter what does happen, it is very important to know the rate and extent of cell surface adsorption; because it is the initial step for ENM cell uptake and potential redistribution back into blood.

In this study, capillary depletion results showed ceria ENM associated with brain endothelial cells. Electron microscopy failed to find any 5 nm ceria in brain tissue, however, nonagglomerated ceria ENM was observed to associate with the luminal wall of brain capillary endothelial cells. Assuming all of the ceria associated with the capillary surface without any agglomeration and based on the mass of ceria ENM we observed in rat brain after arterial ceria ENM perfusion, our calculation showed that 2.4 ± 0.4 % of the brain capillary surface area might be covered by the ceria ENM. We think that the 4.2 ± 0.7 μg of ceria ENM per brain hemisphere seen in the present study might contribute to ceria ENM redistribution or sustained release back to blood. Ceria ENM dissociation from the brain capillary lumina over time may provide an explanation for findings in our pharmacokinetic study where the circulating blood level of two sizes of ceria ENMs increased from 2-4 hours after completion of their iv infusion, which cannot be explained using conventional pharmacokinetics (259). A similar increase of ENM in blood within the first 2 h after its intravenous administration has been reported for quantum dots, however explanation of the increase was not discussed in these reports (230, 231). ENMs that associate with, and subsequently disassociate from, the vascular wall might provide an explanation. Another study showed that 100-200 nm ceria ENMs (primary size 3-5

nm) were observed on the luminal surface of mice tail vein 30 days post intravenous injection (223). It is not known if these agglomerated ceria nanoparticles were from original association with the blood vessel or from redistribution over time. In general, our results showed that ENMs can associate with capillary cells which may contribute to nanoparticle redistribution back into the blood.

This is the first report that a ceria ENM has a higher concentration in the choroid plexus compared with brain regions. Our vascular space results measured by Gd-DTPA showed that the choroid plexus has a larger vascular space than brain tissues. The choroid plexus showed a significantly higher uptake space compared with brain regions in the 100 and 500 μg/ml concentration groups rather than 30 μg/ml group. The uptake space of choroid plexus did not change between 100 and 500 μg/ml concentration groups. Little is known about how metal oxide nanoparticles interact with the choroid plexus. The choroid plexus has larger surface area per weight, a leaky epithelial barrier, and different junction proteins and transport protein expression compared to cerebral endothelium (264, 265). The fundamental differences between the choroidal epithelium and the cerebral endothelium may influence the ceria ENM association sites and determine the ceria ENM saturation concentration. Ceria agglomerates (Figure 4.7) were observed in the choroid plexus compared to fine primary ceria ENM on the surface of the brain endothelial cells, providing evidence that ceria ENM may associate with choroid plexus differently than the BBB, leading to higher concentrations in the choroid plexus. Previous research showed that the choroid plexus sequesters metal ions rapidly and that their concentrations were more than 10 times higher than other brain regions (247, 266). Some polymer

nanoparticles showed similar results as the present study. Poly (d,l-lactide-co-glycolide) nanoparticles showed a high concentration in the choroid plexus (158). The choroid plexus is considered to be a potential region to retain nanoparticles (267) and a pathway to enter the CNS (158, 268). Our results provide the first evidence that ceria ENMs interact significantly with the choroid plexus. Our data showed high variability in choroid plexus. The choroid plexus in rats only weigh 1-2 mg, which might contribute for the high variability. However, this results provides initial evidence of high ceria ENMs association with choroid plexus, which is very important for toxicity concerns and therapeutic application.

4.5. Conclusion

Brain uptake of a 5 nm ceria ENM was flow rate and perfusion concentration independent, showing diffusion was not mediating its association with brain tissue. The ceria ENM concentration was significantly higher in the choroid plexus than in 8 brain regions. Brain ceria ENM association was a very rapid process that reached saturation between 20 and 60 s. The capillary depletion method showed that the ceria ENM was predominately associated with the brain capillary cells rather than brain parenchyma. Furthermore, EM showed most of the ceria ENM associated with the luminal surface of brain endothelial cells, rather than entering the cells. This research provides the first data on the kinetics of ceria interaction with the BBB and choroid plexus. Ceria ENM capillary cell surface association also provides a site from which it can dissociate, redistribute or enter the capillary cells. This information will be important for design of ceria ENMs as a therapeutic agent as well as for a comprehensive toxicology assessment.

4.6. Unsolved problems

This study showed that the brain entry of ceria ENMs is very limited. However, ceria ENMs can associate with the BBB, which provides the possibility to enter the BBB for therapeutic applications. Chapters 3 and 4 demonstrated that it is very important to design biocompatible and stable metal-based ENMs for biomedical applications. Furthermore, different strategies should be used to increase metal-based ENMs flux across the BBB. In chapters 5 and 6, we designed CNA-IONPs which have the potential to improve the biocompatibility and stability of IONPs and enhance IONP flux across using AMF-induced local hyperthermia compared to conventional hyperthermia.

Chapter 5 Block copolymer cross-linked nanoassemblies improve particle stability and biocompatibility of superparamagnetic iron oxide nanoparticles

As I described in 2.5.2, IONPs tend to agglomerate in aqueous solutions unless their surface is properly modified, resulting in plasma protein binding *in vivo* and rapid clearance by the MPS (39). Several studies showed that IONPs, either bare or surface-modified, could cause cell toxicity and oxidative stress *in vitro* and *in vivo* (40-42). Therefore, it is crucial to improve particle stability and biocompatibility of IONPs in the biological environment. In this chapter, we hypothesized that CNAs containing carboxyl groups in the core would simultaneously create, entrap, and protect IONPs as iron ions (Fe^{2+} and Fe^{3+}) co-precipitate inside the nanoassembly core, thus suppressing IONP agglomeration and improve the biocompatibility of IONPs without losing their superparamagnetic properties. CNA-IONPs would be beneficial for future MRI and AMF-induced remote hyperthermia applications.

5.1. Introduction

Aggregation of IONPs leads to altered magnetic properties or even complete loss of magnetism (48). In addition, IONPs are easily oxidized, transforming from magnetite (Fe_3O_4) to maghemite (γFe_2O_3), leading to a broad spectrum of particle size, shape, stability, and magnetic properties (35, 204). Numerous efforts have been made to suppress agglomeration and retain the superparamagnetic properties of IONPs for a prolonged time (269-271). Citric acid is commonly used to stabilize IONPs in aqueous solutions (43, 45, 272). Although citric acid forms a stable chelate with iron oxide, it is

not sufficient to prevent agglomeration and precipitation in the presence of multivalent counter ions (magnesium or calcium) and serum proteins (105-107, 273). Importantly, these IONP formulations, which change particle stability over time *in vivo*, could potentially cause toxic effects *in vivo* (46, 47).

To solve these problems, we recently developed CNAs from biocompatible PEG-p(Asp) block copolymers, which provided stable nanoparticles that can entrap charged, hydrophobic, and amphiphilic payloads without changing particle sizes optimized for tumor accumulation (< 100 nm) (55-57). We hypothesized that CNAs containing carboxyl groups in the core would simultaneously create, entrap, and protect IONPs as iron ions (Fe^{2+} and Fe^{3+}) co-precipitated inside the nanoassembly core, thus suppressing IONP agglomeration (Figure 5.1). In this study, we tested our hypothesis and confirmed that IONPs incorporated into CNAs improve their particle stability and biocompatibility in aqueous solutions without compromising paramagnetic properties.

Particle stability and biocompatibility were determined with or without 30 min AMF exposure in water, PBS, and a cell culture medium with 10% FBS at 22, 37, and 43 °C, respectively. Cytotoxicity of the particles was investigated using a mouse brain endothelial-derived cell line (bEnd.3). T2-weighted MRI enhancement of CNA-IONPs was tested in water, PBS and a cell culture medium. AMF-induced heating properties of 1, 2.5 and 5 mg/mL CNA-IONPs were also evaluated in a cell culture medium for future hyperthermia applications. Conventional citrate-coated IONPs (Citrate-IONPs) were used

as control. Results of this study provide insight into potential applications of CNA-IONPs, integrating MRI diagnosis and thermal therapy.

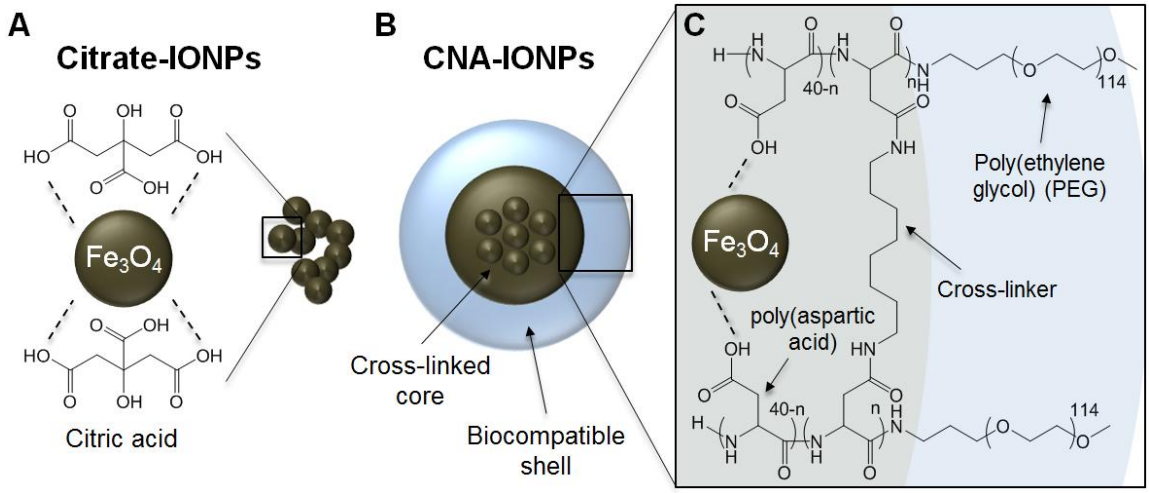

Figure 5.1. Citrate-coated iron oxide nanoparticles (Citrate-IONPs) and cross-linked nanoassemblies entrapping IONPs (CNA-IONPs). (A: A chelate is formed between citric acid and Fe_3O_4 iron oxide; B: CNA-IONPs entrap Fe_3O_4 in the core to protect the iron oxide from agglomeration and protein binding; and C: Fe_3O_4 IONPs are stabilized in the cross-linked core of CNAs.)

5.2. Materials and methods

5.2.1. Materials

N,N′-Diisopropylcarbodiimide (DIC), N-hydroxysuccinimide (NHS), 4-(dimethylamino)pyridine (DMAP), β-benzyl L-aspartate, triphosgene, hexane, benzene, tetrahydrofuran (THF), dimethyl sulfoxide (DMSO), ferrous chloride tetrahydrate ($FeCl_2{\cdot}4H_2O$), ferric chloride hexahydrate ($FeCl_3{\cdot}6H_2O$), ammonium hydroxide (NH_4OH), citric acid monohydrate, and ethanol (100%) were purchased from Sigma-

Aldrich (St. Louis, MO, USA). α-Methoxy-ω-amino poly(ethylene glycol) (PEG, 5 kDa) was purchased from the NOF Corporation (Tokyo, Japan). Cell culture medium Dulbecco's Modified Eagle Medium (DMEM), regenerated cellulose dialysis bags with 6 ~ 8 kDa molecular weight cut off (MWCO), sodium hydroxide (NaOH), and hydrochloric acid (HCl) were purchased from Fisher Scientific (USA). FBS was purchased from Atlanta Biologicals (Lawrenceville, GA, USA) and penicillin-streptomycin (Pen-Strep) was purchased from Invitrogen (Grand Island, NY, USA).

5.2.2. Synthesis of CNAs

CNAs were prepared by cross-linking poly(ethylene glycol)-poly(aspartate) [PEG-p(Asp)] block copolymers as previously reported with slight modification (55). Briefly, β-benzyl-L-aspartate N-carboxy anhydride (BLA-NCA) monomers were prepared by reacting β-benzyl-L-aspartate with triphosgene (1.3 equivalent) in dry THF at 45°C until the solution became clear. Anhydrous hexane was added to the BLA-NCA, which was subsequently recrystallized at -20°C. As shown in Figure 5.2, BLA-NCA monomers were polymerized using amino-terminated 5kDa PEG as a macroinitiator in DMSO (50 mg/mL) at 45°C under dry nitrogen for 48 h to synthesize PEG-poly(β-benzyl L-aspartate) (PEG-PBLA). PEG-PBLA was collected from the reaction solution by precipitation in diethyl ether and freeze drying from benzene. ^{1}H-NMR (400 MHz, Varian) spectra from PEG (3.5 ppm) and benzyl groups (7.3 ppm) was used to determine the block copolymer composition. PEG-PBLA with 40 aspartate repeating units was used for this study. The benzyl groups of PEG-PBLA were removed by 0.1 N NaOH. The benzyl alcohol byproducts and excess NaOH were removed through dialysis, followed by

desalination of the aspartate through the addition of HCl to the dialysis solution to yield PEG-p(Asp). To prepare CNAs, PEG-p(Asp) was dissolved in DMSO to a final concentration of 75 mg/mL followed by the addition of DIC, NHS, and DMAP (in a molar ratio of 4:4:0.2, respectively) to the aspartate units of PEG-p(Asp). A 0.5 molar equivalent of 1,8-diaminooctane was added to the reaction solution, which was placed at 50°C for 72 h. The CNAs were dialyzed against 100% DMSO, 50% DMSO, and finally deionized water to remove impurities, followed by freeze drying. CNA purity was characterized with gel permeation chromatography (GPC, Shimadzu LC20, Japan), which was equipped with refractive index (RI) and ultraviolet (UV) detectors. PEG standards were used to establish a calibration curve for molecular weight determination (Mn = number molecular weight).

5.2.3. Preparation of Citrate-IONPs and CNA-IONPs

Citrate-IONPs were prepared by co-precipitating iron oxides and citric acid in an aqueous solution as previously reported (186). As shown in Figure 5.2B, ferric chloride hexahydrate (Fe^{3+}) and ferrous chloride tetrahydrate (Fe^{2+}) were dissolved in deionized water (Fe^{3+} Fe^{2+} = 2:1), followed by adding ammonium hydroxide dropwise under an N_2 atmosphere at 85 ºC. Citric acid (2 equivalent) was then added to prepare Citrate-IONPs. After 1 h, the solution was placed on a magnet to collect black brown particles, which were washed repeatedly using pure ethanol (274, 275). Citrate-IONPs were dried overnight in a vacuum drying oven.

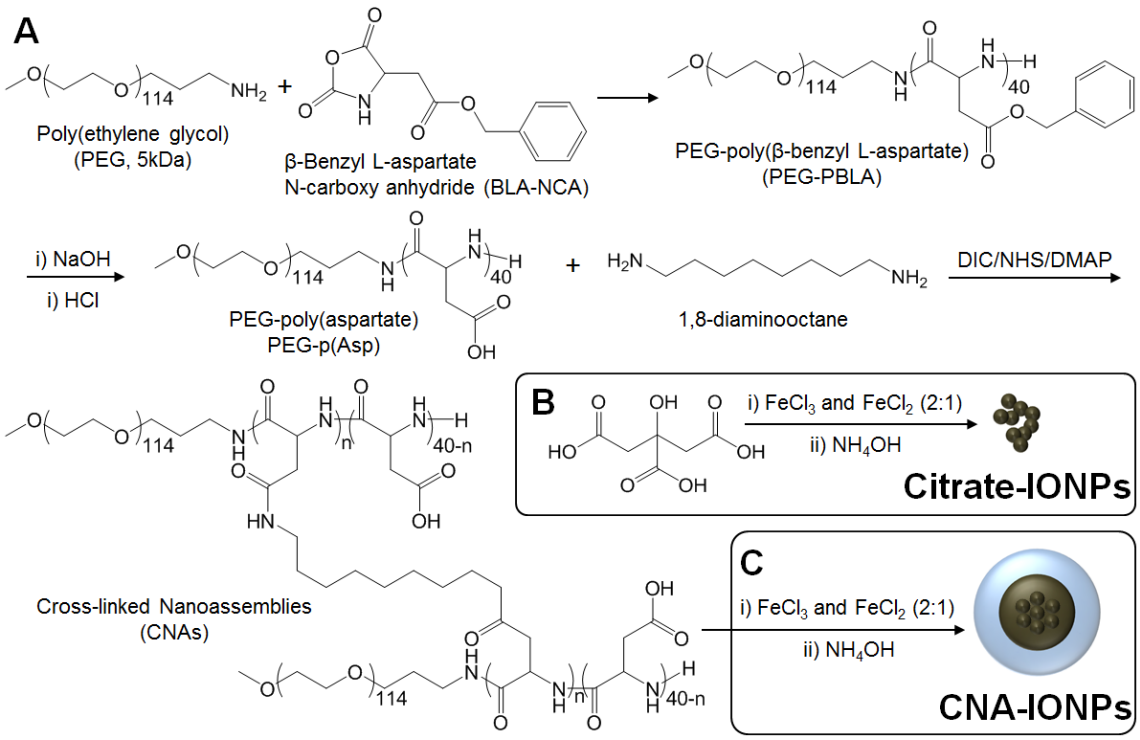

Figure 5.2. Synthesis schemes for empty CNAs (A), Citrate-IONPs (B), and CNA-IONPs (C).

CNA-IONPs were prepared similarly by mixing ferric and ferrous salts at a 2:1 molar ratio with CNAs in deionized water (Figure 5.2C). The total iron ions and the carboxyl groups of CNAs were adjusted in a molar ratio of 1:2. Ammonium hydroxide was added to this mixed solution dropwise under nitrogen atmosphere and the reaction was allowed to proceed at 85°C for 1 h. The solution was centrifuged at 3,000 g for 5 min to remove precipitates and other water-insoluble impurities. CNA-IONPs in the supernatant were dialyzed (MWCO 6 ~ 8 kDa), filtered (0.22 μm syringe filters), and collected by freeze drying.

5.2.4. Particle characterization

The particle size distribution was determined by DLS analysis (90Plus NanoParticle size distribution analyzer, Brookhaven Instruments, Holtsville, NY, USA). Zeta potential was measured with Zetasizer Nano ZS (Malvern Instruments, Worcestershire, UK). The IONP loading content for CNA-IONPs was quantified by thermal gravimetric analysis (TGA, Perkin-Elmer TGA7 Analyzer, Waltham, MA, USA) and inductively coupled plasma mass spectrometry (ICP-MS, Agilent 7500cx, Santa Clara, CA, USA). TGA and ICP-MS determined the amount of iron remaining from CNA-IONPs, following thermal decomposition (100 ~ 600 ºC) and chemical digestion (HNO_3:H_2O_2 = 2:1) of CNAs, respectively.

5.2.5. Particle size and stability evaluation in aqueous media

Particle size and stability of Citrate-IONPs and CNA-IONPs (0.1 mg/mL, based on IONP content) were first observed by dissolving the particles in water, PBS, and DMEM with 10% FBS and 1% Pen-Strep, using 1.5 mL microvials. Aqueous solubility, particle size, and stability of Citrate-IONPs and CNA-IONPs were further characterized under various media: in water at 1 mg/mL, 22 °C, for 30 h; in water at 1 mg/mL, 37 °C, for 30 h; in cell culture medium at 1 mg/mL, 37 °C, for 30 h; and in cell culture medium at 1 mg/mL, 43 °C, for 30 h, as discussed in detail in the Results and Discussion section. DLS was used to monitor time-dependent changes in particle size of all samples.

5.2.6. Cytotoxicity assays

A mouse brain endothelial cell line (bEnd.3) was obtained from American Type Culture Collection (CRL-2299). The cells were cultured in a humidified incubator (37 ºC and 5% CO_2) and used from passages 5 through 10. Cells were seeded on 96 well plates (4,000 cells/well) and incubated with DMEM supplemented with 10% FBS and 1% Pen-Strep for 24 h. These cells were treated with Citrate-IONPs (0, 0.002, 0.02, 0.05, 0.1, and 0.2 mg/mL) and CNA-IONPs (0, 0.2, 0.5, 1, 5, and 10 mg/mL). Citrate-IONP and CNA-IONP concentrations were based on cytotoxicity observed in preliminary experiments. The cells were incubated with Citrate-IONPs or CNA-IONPs for 0.5, 3, 6, 12 and 30 h, followed by washing the cells with PBS three times. After additional 24 h incubation in fresh cell culture media, cell viability was determined using the resazurin dye assay. Resazurin in PBS was added to the cell-containing wells to a final concentration of 100 µM. Cell plates were incubated for an additional 3 h as non-fluorescent resazurin was converted to fluorescent resorufin by live cells (276, 277). Resorufin signals were measured at λ_{ex} 485 nm and λ_{em}530 nm. Cell viability was reported as % of control at the same time.

5.2.7. Magnetic resonance imaging

Citrate-IONPs and CNA-IONPs were dispersed in water, PBS, and cell culture media with two-fold serial dilutions ranging from 0.02 to 2.5 mg/mL (based on IONP content). Citrate-IONP and CNA-IONP solutions (150 µL) were placed in a 96 well plate and imaged on a 3.0 Tesla MR imager (Siemens Tim Trio, Erlangen, Germany) using a 10 cm diameter surface coil to enhance the received signal. Multiple, T2-weighted fast spin echo

images of all samples were acquired with different echo time (TE), to visualize the dependence of the T2 relaxation time on the particle composition and dispersing media. From the multi echo T2 images acquired at different echo times, we used a custom-developed software code to derive T2 on a pixel-by-pixel basis. From these images we estimated the average T2 within the wells of CNA-IONPs in the three media as a function of particle concentration.

5.2.8. Evaluation of AMF-induced heating profiles and particle stability after AMF exposure

The heating profiles of CNA-IONPs were evaluated in cell culture media (1, 2.5, and 5 mg/mL) under AMF induced by a Taylor Winfield induction power supply (Taylor-Winfield Technologies MMF-3-135/400-2, Columbus, OH, USA) equipped with a 15 mm diameter, 5 turn solenoid. The AMF field parameters were set to 59.3 kA/m at 300 kHz for 30 minutes. The temperature of the medium was measured every 0.25 seconds for 30 minutes using a Fluoroptic® thermometer (LumaSense Technologies, Santa Clara, CA, USA). The initial medium temperature was 37 ºC. The CNA-IONP particle stability was monitored in cell culture media (1, 2.5, and 5 mg/mL) for 30 h after 30 min AMF using DLS.

5.2.9. Statistical analysis

One-way ANOVA followed by Tukey's test was used to test for significant differences on particle sizes of the samples with 37 and 43 °C incubation temperatures for 30 h (1 mg/mL) or different concentrations (1, 2.5 and 5 mg/mL) for 30 h after 0.5 h AMF

compared to the particle size of sample at time 0 with 22 °C incubation temperatures (1 mg/mL). Two-way ANOVA followed by Bonferroni multiple comparisons was used to test for significant differences among different concentration groups and times (GraphPad Prism Version 3.00 for Windows, GraphPad Software, San Diego, CA). The results of the statistical analysis for one-way ANOVA and two-way ANOVA will be reported as F(df effect, df error) = F-value and P-value. Statistical significance was accepted at a level of $p < 0.05$. All results are reported as mean ± standard deviation (SD).

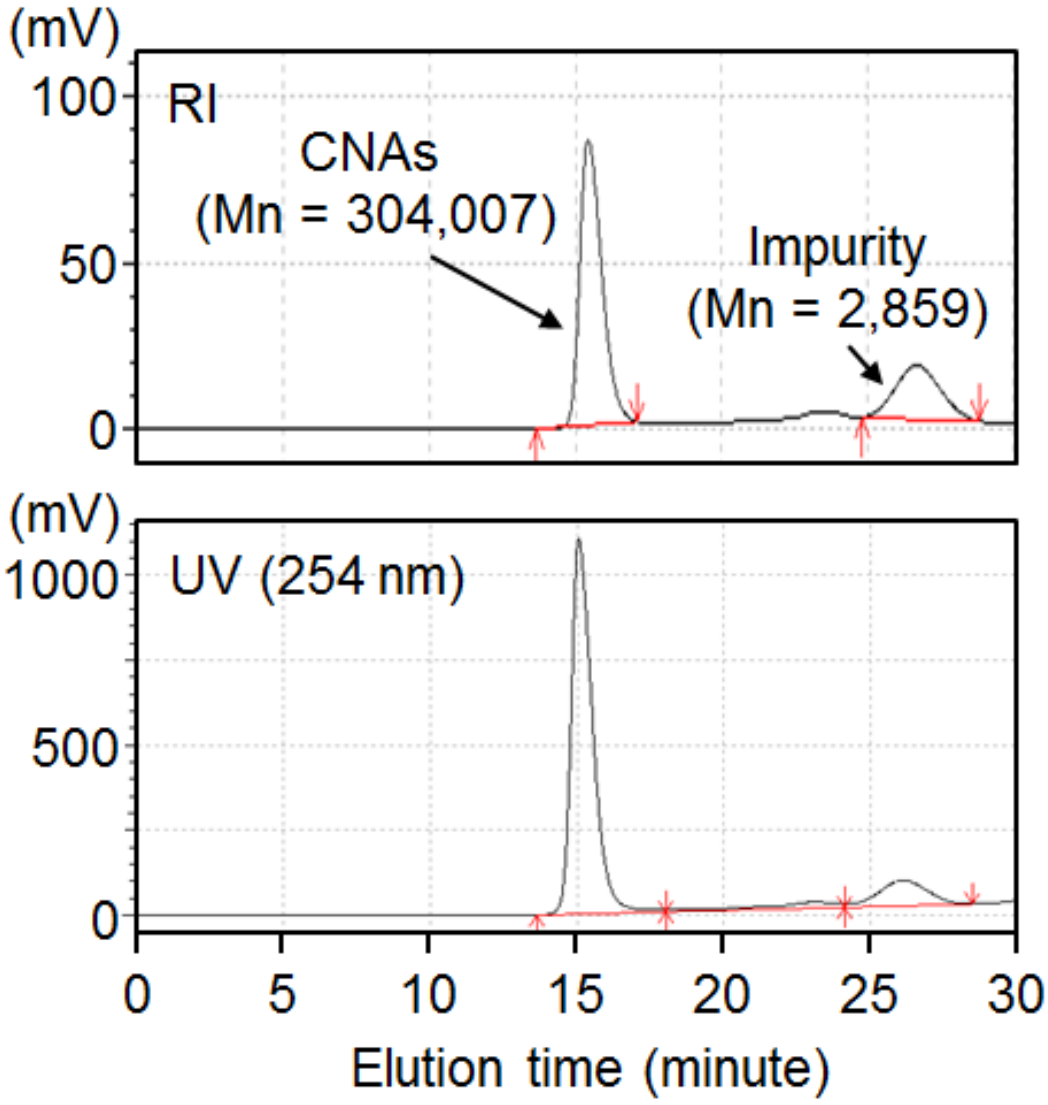

Figure 5.3. Gel permeation chromatography (GPC) spectra of CNAs.

5.3. Results and discussion

5.3.1. Preparation and characterization of Citrate-IONPs and CNA-IONPs

GPC analyses confirmed that CNAs were successfully formed with narrow dispersity (Figure 5.3). Molecular weight of CNAs was 304,007 Da, indicating that approximately 32 PEG-p(Asp) block copolymer chains formed an individual CNA particle. No free PEG-p(Asp) block copolymers (Mn = 9,600 Da) were seen after CNA synthesis, although small molecular weight impurities (Mn = 2,859 Da) were observed. The particle size of empty CNAs was 36 ± 5 nm. These results were consistent with our previous observations for other CNAs (55, 56). The solution containing IONPs formed dark brown precipitates immediately after NH_4OH was added in the presence of either citric acid or empty CNAs. In comparison to Citrate-IONPs, CNA-IONPs remained soluble in aqueous solutions even after centrifugation. As a result, unreacted iron ions, aggregated IONPs, and other impurities were readily removed from CNA-IONPs. Subsequent DLS measurements showed that CNA-IONPs were 25 ± 3 nm, similar to empty CNAs, indicating that the cross-linked core of CNAs effectively suppressed the growth of IONPs inside the nanoassemblies, preventing aggregation. Citrate-IONPs were initially 90 ± 10 nm in water at 200 μg/mL, but their particle sizes varied as agglomeration and precipitation occurred (discussed in detail in *Particle stability* section). CNA-IONPs showed 25 ± 3 and 25 ± 1 % (wt%) IONP loading, determined by TGA and ICP-MS analyses, respectively. Zeta potentials of Citrate-IONPs and CNA-IONPs in PBS at pH 7.4 were -29.5 ± 3.6 and -5.0 ± 0.6 mV, respectively. These results suggested that CNA-IONPs effectively protected IONPs inside the carboxyl-rich nanoassembly core, shielding the electric charge of IONP chelates with CNAs.

5.3.2. Particle stability

Citrate-IONPs and CNA-IONPs were first dispersed in water, PBS, and cell culture media at 0.1 mg/mL for solubility testing (Figure 5.4). Citrate-IONPs dispersed partially in aqueous solutions, but the solutions were turbid (Figure 5.4A), forming precipitates (Figure 5.4B, blue box). On the other hand, CNA-IONPs were stable in all aqueous solutions: the letters 'IO' can be seen clearly through the brown solution in Figure 5.4A and no precipitates are seen in Figure 5.4B (red box). Interestingly, Citrate-IONPs remained at around 400 nm in the serum-containing cell culture medium at 37 ºC for 3 h, but they ultimately precipitated in water, PBS, and DMEM (Figure 5.5A). It is surmised that Citrate-IONPs in the cell culture medium might have bound to bovine serum albumin (BSA) from 10% FBS, forming 400 nm complexes that dispersed in the solution as previous studies reported that BSA stabilized metal oxide nanoparticles (278-280). Nevertheless, rapid agglomeration in the cell culture medium to > 400 nm will still likely limit biomedical applications of Citrate-IONPs. Previous research demonstrated that IONPs smaller than 50 nm had a longer circulation time in blood than larger IONPs that were rapidly cleared by the MPS (281).

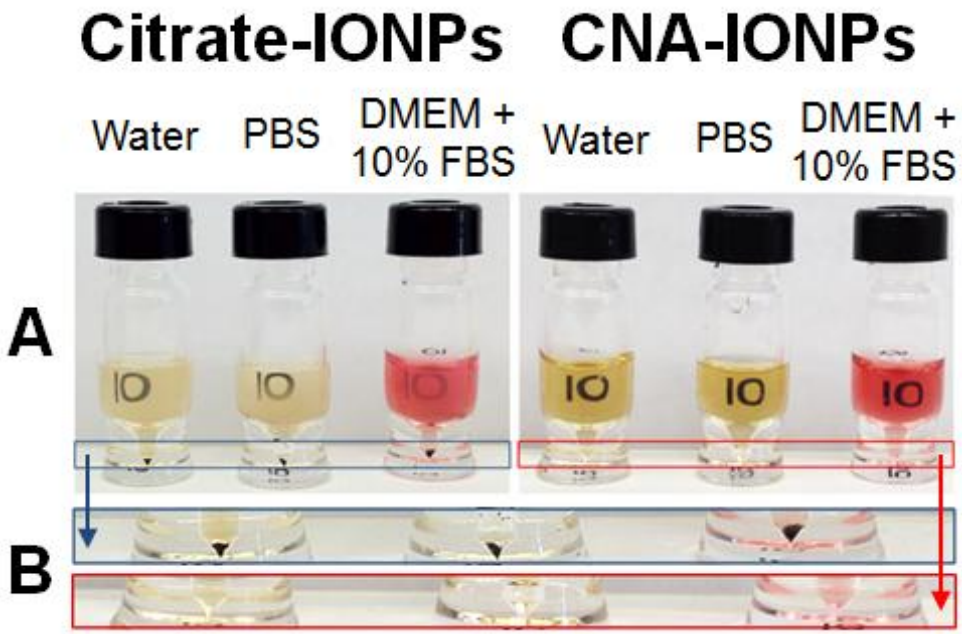

Figure 5.4. Citrate-IONPs and CNA-IONPs in aqueous solutions. (A: Turbidity of sample solutions at 0.1 mg/mL; and B: Enlarged images of the bottom of a 1.5 mL glass vial showing precipitates of Citrate-IONPs [blue box] but not CNA-IONPs [red box])

CNA-IONPs were stable in water and cell culture media at 22, 37, and 43 ℃ for 30 h, and particle size remained unchanged between 25 ~ 29 nm in diameter (Figures 5.5A and 5.5B). There were no significant changes in the particle size of CNA-IONP from 1 to 5 mg/ml (Figure 5.5C). A previous study showed that the magnetic property of IONPs is size-dependent and that the particle size is linearly correlated with the saturation

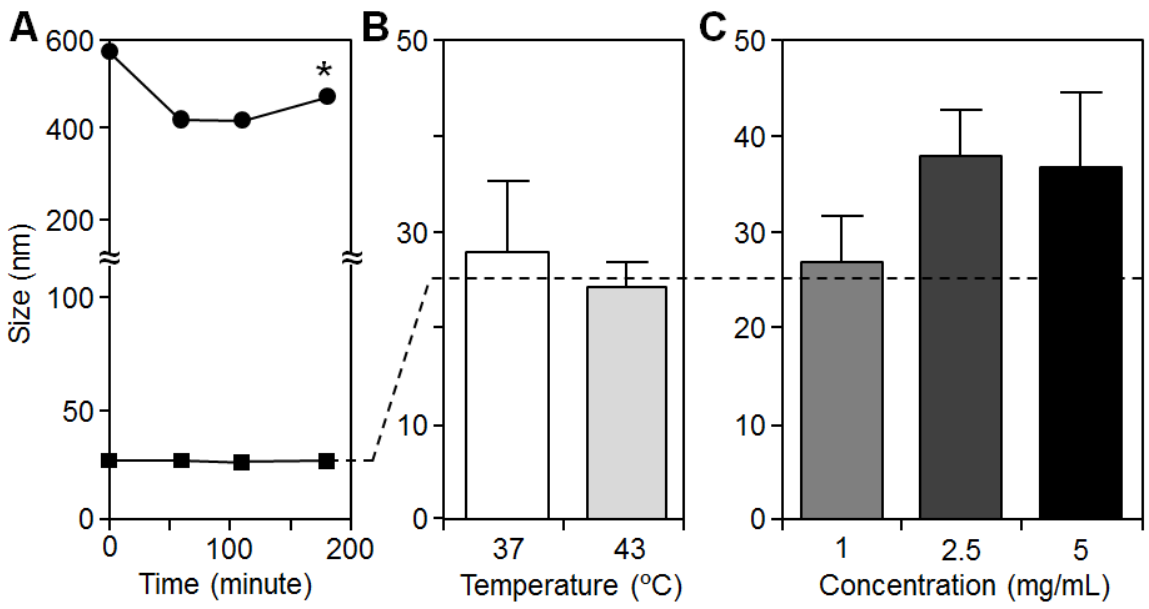

Figure 5.5. Particle stability characterization results. Samples were incubated in DMEM cell culture media with 10% FBS. (A: Time-dependent changes of particle sizes for Citrate-IONPs [circles] and CNA-IONPs [squares] incubated at room temperature. The asterisk (*) indicates that Citrate-IONPs started precipitating; B: Temperature effects on particle sizes for CNA-IONPs incubated for 30 h (n = 6); and C: Concentration effects on particle sizes of CNA-IONPs following 30 min AMF (n = 4))

magnetization of IONPs (282). As mentioned above, IONPs below 50 nm can circumvent the MPS and have a longer circulation time (281). Several researchers demonstrated plasma proteins rapidly bound to nanoparticle surfaces, forming a protein corona which can change nanomaterial physicochemical properties and influence their fate in vivo (232, 254, 283). In this study, the presence of 10% FBS in cell culture medium produced no significant change in the particle size of CNA-IONPs over 30 h in a biologically-relevant medium compared with their size in water. In general, the small particle size that remained constant for > 30 h is favorable for in vivo applications using CNA-IONPs because particle size-induced changes in IONPs magnetic properties and biodistribution will be minimal. Therefore, these results suggested that CNA-IONPs would be stable in

blood in vivo, which will be beneficial especially for increasing their blood retention time, and thus potentially improving blood-tumor barrier penetration for diagnosis and therapy of tumors located away from the body surface such as brain (284).

5.3.3. Cytotoxicity of Citrate-IONPs and CNA-IONPs

Time-dependent cytotoxicity of Citrate-IONPs and CNA-IONPs was tested in a murine brain endothelial cell line (bEnd.3) as shown in Figure 5.6. Citrate-IONPs caused a significant decrease in cell viability at concentrations greater than 0.05 mg/mL, and cell viability dropped rapidly at 0.1 mg/mL after 3 h (Figure 5.6A). This is consistent with previous reports showing IONPs caused serious cytotoxicity in cells, limiting their applications as imaging contrast agents (41), and significantly increased reactive oxygen species (> 0.025 mg/mL) (285). Even FDA-approved MRI contrast agents, such as Endorem® and Sinerem® (derivatized dextran coated IONPs), are reported to cause cell growth inhibition over a 24 h period at 0.05 mg/mL (286), similar to the Citrate-IONPs cytotoxic concentration in this study. Previous studies showed that IONP toxicity in vitro was highly dependent on size, surface modification, charge, and cell type (287). However, most IONPs started to show toxicity above 1 mg/mL in vitro despite their size, surface modification, charge, or the cell type (41). On the contrary, CNA-IONPs caused no cell death up to 10 mg/mL and 30 h exposure (Figure 5.6B). These results demonstrate that CNA-IONPs significantly improved biocompatibility of IONPs entrapped inside the nanoassemblies as opposed to citrate-IONP formulations.

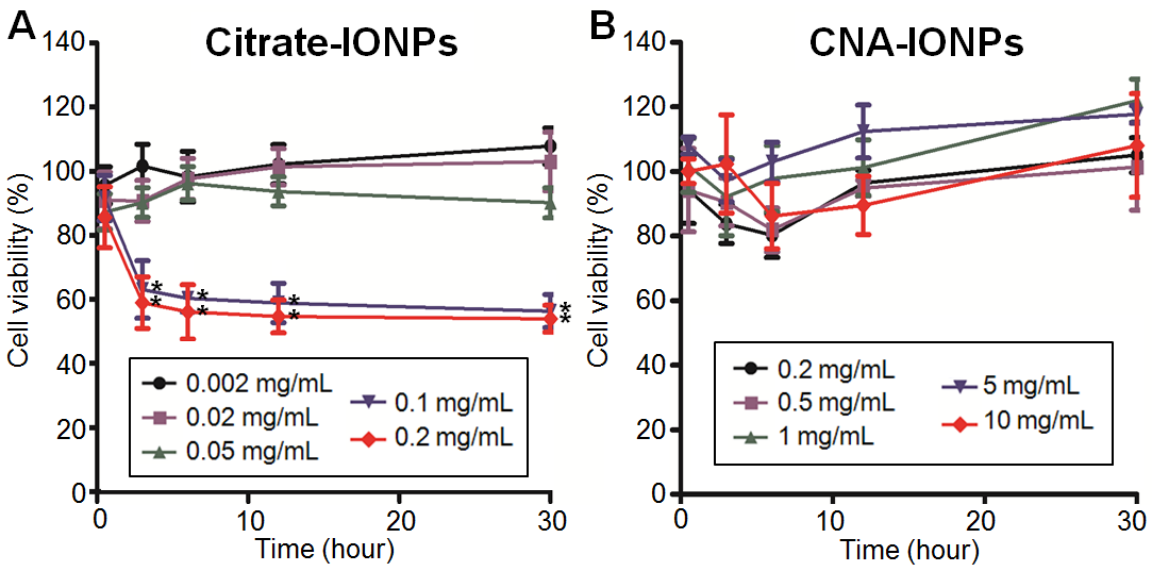

Figure 5.6. Biocompatibility characterization results. A mouse brain endothelial cell line (bEnd.3) was incubated with either Citrate-IONPs (A) or CNA-IONPs (B) at different concentrations and times (n = 4). The asterisks (*) indicate significant differences ($F(4,75) = 150$, $p < 0.0001$) from the three lower concentrations (0.002, 0.02, and 0.05 mg/mL).

5.3.4. MRI of Citrate-IONPs and CNA-IONPs

Citrate-IONPs and CNA-IONPs showed concentration-dependent changes on T2-weighted MR images (image darkening) (Figure 5.7). Citrate-IONPs showed contrast patterns similar to CNA-IONPs in water, but Citrate-IONPs dispersed initially yet agglomerated gradually in PBS and cell culture media, forming agglomerates on the bottom of wells when placed in the magnetic field of the MR imager. Images acquired transverse to the wells showed that Citrate-IONPs precipitated at the bottom of wells producing zones of intense signal loss on T2 images (side-view images in Figure 5.7). Citrate-IONPs showed a dark signal on the T2 images above 0.16 mg/mL in water. Citrate-IONPs were observed to agglomerate faster in cell culture medium than PBS at the same concentration (data not shown), and showed dark images above 0.63 mg/mL.

On the contrary, CNA-IONPs were stable in water, PBS and cell culture media (Figure 5.4B, red box), showing concentration-dependent T2-weighted MRI contrast (Figure 5.7). CNA-IONPs produced dark MR images as low as 0.04 mg/mL in water and 0.02 mg/mL in cell culture medium. CNA-IONPs evenly distributed in the solution and produced homogenous MR images. The average T2 within the wells of CNA-IONPs in water, PBS and cell culture medium as a function of their concentration were estimated from these images. Plots of relaxation rate (i.e. 1/T2) versus CNA-IONP concentration showed a linear dependency with correlation coefficients nearly 1 in all three media (data not shown). From the slope of 1/T2 vs particle concentration curves, we estimated CNA-IONP relaxivities to be 70, 63 and 73/s/mM Fe in water, PBS and cell culture medium, respectively. Previous research showed that IONPs have T2 relaxivities around 30 /s/mM Fe (1, 39, 52). Contrast efficiency was considerably enhanced by CNA-IONPs compared with Citrate-IONPs. We tried to estimate relaxivities for the T2* relaxation rates (1/T2*, s^{-1}) measurements in a similar way. However, the T2* was so low for the samples that the measurements were not reliable. Nevertheless, the ratio of T2* relaxivity and T2 relaxivity (R2*/R2, $mM^{-1}s^{-1}$) would be high, indicating the potential of the CNA-IONPs to strongly influence the contrast on either T2* or T2 weighted MRI. Previous clinical investigation showed that IONPs with diameters less than 40 nm can accumulate at the margins of human brain tumors resulting in improvement of their delineation on MRI (73). Therefore, CNA-IONPs are expected to significantly improve contrast efficiency and serve as excellent T2 contrast agents in future in vivo applications.

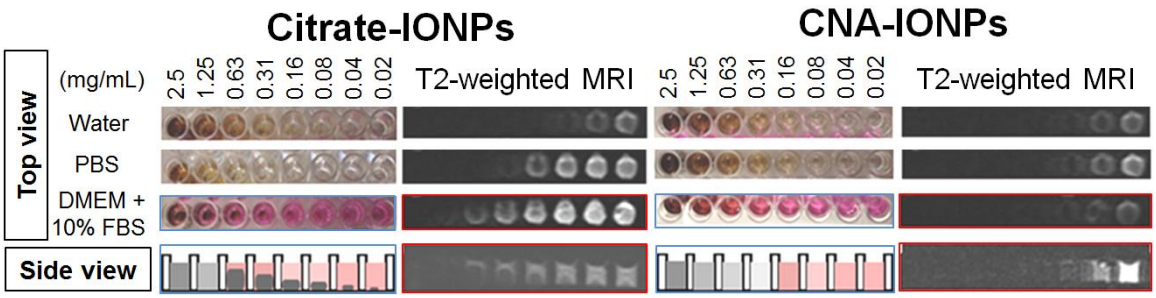

Figure 5.7. Visual images and T2-weighted MRI of Citrate-IONPs and CNA-IONPs. Serial dilutions of the samples were prepared on a 96-well plate, containing water, PBS, and DMEM with 10% FBS. Side view images of transverse plane MRIs show dispersion and precipitation of the Citrate-IONPs and lack of CNA-IONP precipitation in DMEM with 10% FBS.

5.3.5. AMF-induced heating profiles and particle stability after AMF exposure

Another exciting application of IONPs is AMF-mediated remote heating hyperthermia. CNA-IONPs in cell culture media generated heat in response to AMF, increasing the solution temperature in a concentration-dependent manner (Figure 5.8). The solution temperature reached equilibrium in 10 min at 40, 41 and 42 °C with 1, 2.5 and 5 mg/mL CNA-IONPs, respectively. This temperature range is promising because previous results demonstrated that cancer cells were susceptible to > 40 ºC and IONP-induced local hyperthermia appeared effective to kill glioma T-9 cells in Fisher F344 rats (288, 289). CNA-IONPs in cell culture media exposed to AMF for 30 min were subsequently incubated for 30 h at 37 ºC, yet the AMF caused no adverse changes in particle sizes of CNA-IONPs (Figure 5.5C). Although no large aggregates were formed, the particle sizes of CNA-IONPs increased slightly at 2.5 and 5 mg/mL, following 30 minute AMF exposure and subsequent 30 h at 37 ºC. Such an increase was not shown in 1 mg/mL CNA-IONPs. We found that the particle sizes were consistent for all 1 mg/mL CNA-IONPs incubated at 22, 37, and 43 ºC for 30 h continuously or after 30 min AMF exposure. These results suggested that the increase in particle sizes of 2.5 and 5 mg/mL

CNA-IONPs following 30 min AMF exposure might be attributed not to interparticular aggregates during AMF-induced heat generation but to molecular vibration of IONPs entrapped in CNAs, causing relaxation and rearrangement of block copolymer segments in the CNA core. Despite the slight increase in the particle size, CNA-IONPs were always smaller than 40 nm after 30 h at 37 ºC in cell culture media regardless of AMF exposure, indicating that IONPs can remain entrapped stably inside CNAs without compromising AMF-responsive magnetic properties. These results suggested that CNA-IONPs would be a promising nanoscale tool to achieve localized hyperthermia in vivo, an elegant thermal therapy that invokes little damage to critical organs or tissues such as the central nervous system compared with whole body hyperthermia, which often leads to potential toxicities to the brain (58), or to develop a multifunctional nanoparticle for theranostic applications by delivering IONPs in combination with various therapeutic agents (33, 190).

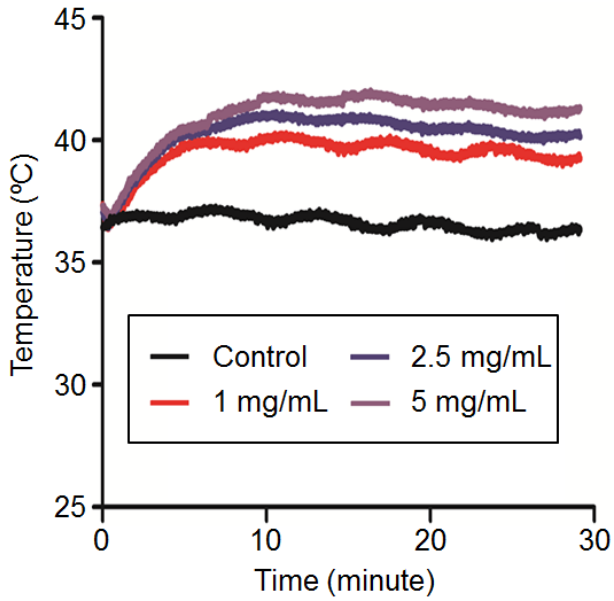

Figure 5.8. Representative heating profiles of CNA-IONPs in the presence of AMF. Three concentrations (1, 2.5, and 5 mg/mL) were tested for fine-tuned remote heating

with 30 minute applications of AMF. Control indicates the initial temperature of cell culture medium containing no CNA-IONPs (37 ºC).

5.4. Conclusions

CNA-IONPs, block copolymer cross-linked nanoassemblies entrapping superparamagnetic Fe_3O_4 iron oxide in a cross-linked core, showed controlled particle size in biological conditions and less toxicity without loss of magnetic properties in comparison to Citrate-IONPs, conventional iron oxide formulations stabilized with citric acid. CNA-IONPs did not agglomerate in water, PBS, or cell culture media, maintaining a clinically-relevant particle size (< 40 nm), suggesting that such stable and small CNA-IONPs may achieve preferential accumulation in tumors and reduced macrophage uptake in vivo. Cytotoxicity of CNA-IONPs was significantly lower than that of Citrate-IONPs, causing no cell death up to 10 mg/mL using a murine brain endothelial cell line (bEnd.3). For MRI contrast agent application, CNA-IONPs showed concentration-dependent T2-weighted MRIs with correlation coefficients nearly 1 between CNA-IONP concentrations and T2-weighted MRIs. CNA-IONPs considerably enhanced the T2 relaxivities compared to Citrate-IONPs. CNA-IONPs retained the magnetic properties of IONPs, which generated heat at mild hyperthermic temperatures (40 ~ 42°C) in the presence of AMF. In conclusion, CNA-IONPs significantly improved particle stability and biocompatibility of IONPs, and thus provide a promising iron oxide nanoparticle formulation for MRI and AMF-induced remote hyperthermia with low toxicity and high efficiency.

5.5. Unsolved problems

In the studies reported in this chapter, we successfully developed stable and biocompatible CNA-IONPs, which showed their potential for MRI diagnosis and therapeutic applications in the CNS. For biomedical application in the brain, whether CNA-IONPs can cross the BBB needs to be determined. Furthermore, mild whole body hyperthermia can increase BBB permeability, which provide the potential for IONPs to cross the BBB using AMF-induced hyperthermia (58). Whether the flux of CNA-IONPs across the BBB can be enhanced by taking advantage of unique properties of IONPs such as AMF-induced hyperthermia need to be defined. In the next chapter, we will investigate whether AMF-induced hyperthermia enhance the paracelullar and transcelullar flux of CNA-IONPs across the BBB.

Reproduced with permission from Dan M, Scott DF, Hardy P, Wydra RA, Yokel RA, Hilt JZ, Bae Y. Block copolymer cross-linked nanoassemblies improve particle stability and biocompatibility of superparamagnetic iron oxide nanoparticles. Pharmaceutical Research 2013, 30(2):552-61. Copyright © 2013 Springer Science+Business Media, LLC. Author's contributions: Dan M synthesized and characterized Citrate-IONPs and CNA-IONPs and tested their stability and toxicity. Dan M and Bae Y drafted the manuscript. Yokel RA revised the manuscripts critically. Scott DF carried out preparation and characterization of CNAs and drafted the CNAs method section. Hardy PA carried out MRI and drafted the method and results section of MRI. Wydra RJ and Hilt JZ developed Citrate-IONPs synthesis method and supervised the synthesis of Citrate-IONPs.

Chapter 6 Alternating magnetic field enhanced the blood brain barrier association and paracellular flux of superparamagnetic iron oxide nanoparticles

The hypothesis of this chapter is that AMF-induced hyperthermia would significantly increase the paracellular and/or transcellular flux of IONPs, and influence the BBB cell association with IONPs compared with conventional hyperthermia. We investigated the effect of conventional hyperthermia and AMF-induced hyperthermia on BBB permeability using two *in vitro* BBB models, bEnd.3 and Madin-Darby canine kidney (MDCKII) cells. Results of this study will give us a better understanding how AMF-induced hyperthermia influences IONP association with BBB cells and flux across the BBB, which will provide important information for the future application of IONP in the CNS and insight into the difference between conventional hyperthermia and AMF-induced hyperthermia on the BBB permeability and IONPs flux.

6.1 Introduction

The BBB's tight junctions and drug efflux transporters play a crucial role in safeguarding the brain from endogenous and exogenous compounds, including most therapeutics circulating in the blood (28). One of the most promising approaches to overcome limited drug flux to the CNS is the employment of multifunctional nanoparticles (290). However, most published studies showed indirect evidence of nanoparticle flux across the BBB into the brain by monitoring fluorescent and radioactive drugs (146, 147) or therapeutic efficacy of drugs in animal models of brain tumors (148). A better understanding of

nanoparticle association with and flux across biological barriers including the highly regulated BBB is urgently needed.

One type of multifunctional nanoparticle, IONPs, has multiple bionanomedical applications, such as diagnosis and therapy for the CNS (291). IONPs can be activated by an AMF to generate controlled local hyperthermia (292). IONPs can also be used as T2 MRI contrast agents for pathologies in the CNS such as brain tumors (34). To achieve CNS applications, the ability of IONPs to cross the BBB needs to be better understood. A recent study evaluated the uptake and transport of different surface modified IONPs by human-derived endothelial cells; no IONP flux across the BBB was observed under normal conditions (293). However, the influence of AMF-induced local hyperthermia on BBB permeability and IONP flux across the BBB has not been reported.

Numerous researchers showed mild whole body hyperthermia can increase BBB permeability, which has potential for brain therapeutic application (58). However, whole body hyperthermia led to heat stress *in vivo* and caused toxicity to the CNS such as edema (58, 60). An IONP nanocarrier system can generate a local hyperthermia to increase BBB permeability and brain accumulation of IONPs for diagnosis and therapy in the CNS.

In the previous chapter, we developed CNA-IONPs, which are stable in cell culture medium with and without AMF for at least 30 h. They produced no observed cytotoxicity in bEnd.3 cells when exposed up to 10 mg/mL for 30 h (292). CNA-IONPs

significantly improved particle stability and biocompatibility of IONPs compared to citrate-coated IONPs, and thus provide a promising iron oxide nanoparticle formulation that retain paramagnetic properties for AMF-induced hyperthermia and T2 MRI enhancement. We used CNA-IONPs as a IONP nanocarrier model to investigate our hypothesis that AMF-induced hyperthermia would significantly increase the paracellular and/or transcellular flux of IONPs, and influence the BBB cell association with IONPs compared with conventional hyperthermia.

In this report the objective of the study was to elucidate the potential and mechanism of AMF-induced hyperthermia to increase IONP flux across the BBB. We evaluated CNA-IONP flux across, and effects on two *in vitro* BBB models (bEnd.3 and MDCKII cell lines) at 37 °C, conventional hyperthermia at 43 °C (0.5 h) or AMF-induced hyperthermia at 41 °C (0.5 h). The paracellular flux changes induced by conventional hyperthermia at 43 °C up to 4 h were monitored by LY, a paracellular flux maker. Using TEM, the cellular localization of the iron oxide core of the studied nanoparticles was investigated. Conventional citrate-IONPs were used as a control.

6.2. Methods

6.2.1. Lucifer yellow flux and transendothelial electrical resistance

To monitor flux through the paracellular pathway, Lucifer yellow (100 µM) (Sigma-Aldrich, St. Louis, MO), which fluxes across cells via this pathway, was added to the medium on the donor side of the cells. Samples (100 µL) of the medium from the donor chamber were collected at time zero and from the receiving chamber at different time

points for LY concentration analysis. Fluorescence was determined in a SpectraMax M5 Multi-Mode Microplate Reader (Molecular devices, Sunnyvale, CA) at $\lambda_{ex}\backslash\lambda_{em}$ = 450/530 nm and compared with a standard of Lucifer yellow in Dulbecco's Modified Eagle Medium (DMEM, Mediatech, Manassas, VA) or minimum essential medium with Earle's salts (MEM, Mediatech, Manassas, VA) depending on cell lines and cell culture conditions (Appendix B) (294). Transendothelial electrical resistance (TEER) of bEnd.3 or MDCKII Transwell® models was measured every other day using a RMA321-Millicell-ERS voltohmmeter (Millipore Corp, Billerica, MA).

6.2.2. Evaluation of AMF-induced heating profiles and particle stability after AMF exposure

The heating profiles of CNA-IONPs induced by AMF-activation of CNA-IONPs were evaluated in cell culture media (2.5 mg/mL) in the Transwell® cell model under AMF induced by a Taylor Winfield induction power supply (Taylor-Winfield Technologies MMF-3-135/400-2, Columbus, OH) equipped with a 15 mm diameter, 5 turn solenoid. The AMF field parameters were set to 33.4 kA/m at 300 kHz for 0.5 h. The temperature of the medium in the Transwell® donor chamber was measured every 0.25 seconds for 0.5 h using a Fluoroptic® thermometer (LumaSense Technologies, Santa Clara, CA). The initial medium temperature was 37 ºC. CNA-IONP stability was monitored for 30 h after 0.5 h at 37 ºC, 43 ºC and AMF using DLS analysis (90Plus NanoParticle size distribution analyzer, Brookhaven Instruments, Holtsville, NY).

6.2.3. Effects of AMF on CNA-IONP and Citrate-IONP cell association and flux using bEnd.3 and MDCKII *in vitro* BBB models

Citrate-IONPs (0.05 mg/ml) or CNA-IONPs (2.5 mg/ml) were introduced into the donor chamber at 37ºC or 43ºC or exposed to AMF for 0.5 h. All were then maintained at 37 ºC for 30 h. Most clinical research showed conventional hyperthermia between 41 and 45 °C can induce tumor cell death (190). Conventional hyperthermia at 43 °C was chosen to compare with AMF-induced hyperthermia. AMF was induced by the Taylor Winfield induction power supply described above. The AMF field parameters were set to 33.4 kA/m at 300 kHz. Samples (100 µL) were collected from the donor chamber at time 0 and from the receiving chamber at different time points. IONP cell uptake was terminated by removal of the medium and addition of ice cold solution containing 137 mM NaCl and 10 mM HEPES at PH 7.4 (295). Cells were trypsinized using 0.25% trypsin-EDTA for 5 minutes at 37°C and the suspension centrifuged. The cell pellet was re-suspended with DMEM. A trypan blue exclusion test was performed to assess cell viability. Protein concentrations were measured using a bicinchoninic acid assay (BCA Protein Assay Kit, Thermo Fisher Scientific, Waltham, MA). Iron concentrations in cells and samples were measured by Ferrozine assay (Appendix B). All experiments were done three or four times.

6.2.4. Effect of conventional hyperthermia on paracellular flux using a MDCKII *in vitro* BBB model

The effect of hyperthermia on the paracellular pathway was tested using a MDCKII *in vitro* BBB model. LY (100 µM) was added to the medium on the donor chamber of the Transwell®. The cells were incubated for 0.5, 1, 2 and 4 h at 43 °C followed by

incubation at 37 °C till 6 h. Samples (100 µL) were collected from the donor chamber at time 0 and from the receiving chamber up to 6 h. Cells were collected as described in the above section. A trypan blue exclusion test was performed to assess cell viability at the end of the experiment. LY concentrations were analyzed as described above. All experiments were performed in triplicate wells and repeated once in triplicate wells.

6.2.5. Citrate-IONP and CNA-IONP cell localization using transmission electron microscopy

bEnd.3 and MDCKII cells were seeded on 12 well plates (BD Falcon, San Jose, California) at a density of 200,000 cells/cm^2. A cell uptake experiment was performed 3 days after seeding. The cells were exposed to a cell culture medium containing 0.05 mg/mL Citrate-IONPs or 0.05 mg/mL CNA-IONPs for 2 h then quickly washed with ice cold saline 3 times. The cells were fixed in 3.5% glutaraldehyde in 0.1M cacodylate buffer, pH 7.4 for 1 h at 4 °C. Samples were dehydrated in ascending concentrations of ethanol and embedded in Eponate 12. After polymerization, blocks were sectioned at 80 nm for TEM viewing in a Philips Tecnai 12 Biotwin electron microscope (FEI, Hillsboro, Oregon).

6.2.6. The apparent permeability coefficient

The apparent permeability coefficient (P_{app}) of LY and CNA-IONPs exposed to 37ºC or 43ºC or AMF for 0.5 h followed by 30 h incubation at 37ºC was calculated using GraphPad Prism (GraphPad Software, San Diego, CA). The first 6 h flux data were used with R^2 cutoff > 0.8. The P_{app} in (cm/s) was calculated using the equation: P_{app} =

$(\Delta Q/\Delta t)/(area*C_D)$ (296). *ΔQ/Δt* is the linear appearance rate obtained from the profile of the transported amount of the substrate against time (mg/s). *area* is the surface area of the cell monolayer (4.67 cm^2 for a 6-well plate). C_D is the initial donor concentration of LY or nanoparticle (mg/mL).

6.2.7. Statistical analysis

Influx rates of LY and CNA-IONPs were calculated by linear regression using GraphPad Prism. The first 6 h data were used with R^2 cutoff > 0.8. Bartlett's was used to test if samples have equal variances. One-way ANOVA followed by Tukey's test was used to test for significant differences of Citrate-IONP and CNA-IONP cell association among control, conventional hyperthermia and AMF-induced hyperthermia conditions. One-way ANOVA followed by Tukey's test was also used to test for significant differences of apparent permeability coefficients of LY and CNA-IONP among control, conventional hyperthermia and AMF-induced hyperthermia conditions. Two-way ANOVA followed by Bonferroni multiple comparisons was used to test for significant flux differences among the treatment groups and times using GraphPad Prism. The results of the statistical analysis for one-way ANOVA and two-way ANOVA will be reported as F(df effect, df error) = F-value and P-value. All results are reported as mean ± standard deviation (SD). Statistical significance was accepted at $p < 0.05$.

6.3. Results

6.3.1. Characterization and stability of Citrate-IONPs and CNA-IONPs

AMF activation of CNA-IONPs in cell culture medium generated heat. The cell culture media temperature reached equilibrium in 10 min at 41 °C with 2.5 mg/mL CNA-IONPs (Figure 6.1A). IONP loading contents in CNAs were 25 ± 3 and 25 ± 1 wt % determined by thermal gravimetric analysis and inductively coupled plasma mass spectrometry analyses, respectively. DLS measurements showed that AMF-induced hyperthermia had no effects on the CNA-IONP size at 30 h (Figure 6.1B). Citrate-IONPs were 90 ± 10 nm in water at 200 µg/mL, but they agglomerated > 400 nm and precipitated in PBS and cell culture medium (292). Furthermore, conventional hyperthermia at 43 °C and AMF-induced hyperthermia accelerated the agglomeration of Citrate-IONPs (> 800 nm).

6.3.2. Citrate-IONPs and CNA-IONPs flux and cell association using a bEnd.3 in vitro BBB model

In order to study the flux of IONPs across the BBB, bEnd.3 cells were grown as a monolayer on Transwell® inserts (Figure 6.2A). All the flux experiments were studied 7-10 days after cell seeding on the Transwell® insert, when TEER was > 120 Ω/cm^2. The P_{app} of Lucifer yellow was 3.81 ± 0.17 X 10^{-6} cm/s, similar to a previous report (Table 6.1) (297).

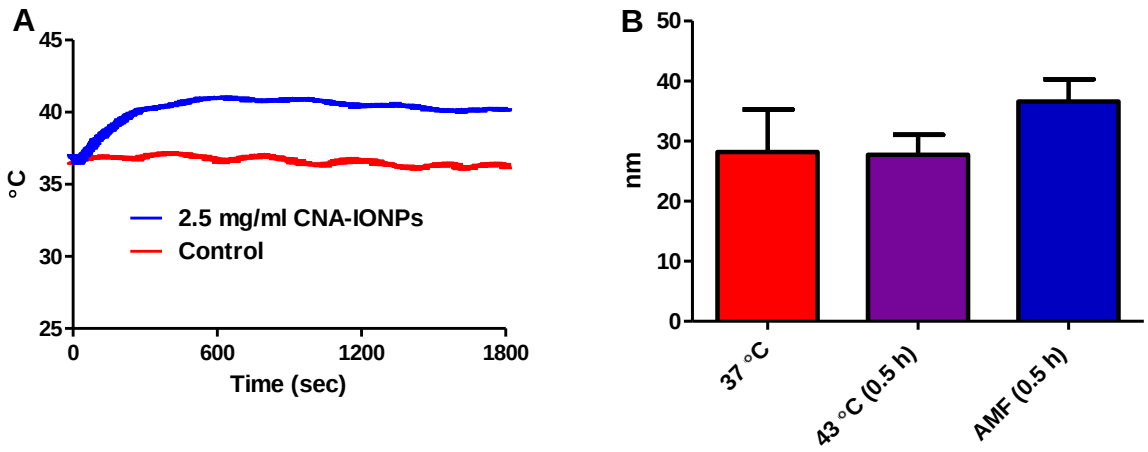

Figure 6.1. Representative heating profiles of CNA-IONPs (2.5 mg/mL) in the Transwell® cell model for fine-tuned remote heating with 0.5 h applications of AMF. Control indicates the temperature of cell culture medium containing no CNA-IONPs (37 ºC) (A). Particle stability characterization results using DLS after exposure to 37 °C for 30 h (n = 6), 43 °C (0.5 h) followed by 37 °C for 30 h (n = 6) or AMF (0.5 h) followed by 37 °C for 30 h (n = 4) (B).

Table 6.1. The apical-to-basolateral apparent permeability coefficients of Lucifer yellow and CNA-IONPs flux using bEnd.3 and MDCKII in vitro BBB models at 37°C for 6 h (n = 3), 43°C (0.5 h) followed by 37°C (n = 3) for 6 h or AMF (0.5 h) followed by 37°C for 6 h (n = 4).

P_{app}		**37 °C**	**43 °C (0.5 h)**	**AMF (0.5 h)**
bEnd.3	LY X 10^{-6} (cm/s)	3.81 ± 0.17	4.04 ± 0.14	7.25 ± 0.28*
Transwell® model	CNA-IONPs (2.5 mg/mL) X 10^{-6} (cm/s)	0.67± 0.09	0.67± 0.09	1.66 ± 0.37*
MDCKII	LY X 10^{-6} (cm/s)	0.49 ± 0.03	0.49 ± 0.049	0.59 ± 0.04*
Transwell® model	CNA-IONPs (2.5 mg/mL) X 10^{-6} (cm/s)	0.06 ± 0.01	0.056 ± 0.011	0.13 ± 0.02*

* Significantly different compared with 37 and 43 °C.

Citrate-IONPs (0.05 mg/mL) and CNA-IONPs (2.5 mg/mL) were used in the flux study according to our previous cytotoxicity study (292). The fluxes of Citrate-IONPs did not increase over 30 h and they were similar in the control group (37 °C for 30 h), conventional hyperthermia group (43 °C for 0.5 h followed by 37 °C for 30 h) and AMF-induced hyperthermia group (AMF for 0.5 h followed by 37 °C for 30 h) (Figure 6.2B). However, Citrate-IONP cell association significantly increased in the conventional hyperthermia and AMF-induced hyperthermia groups compared to control ($F(2,6) = 24$, $P < 0.0014$) (Figure 6.2C). TEM was used to observe Citrate-IONPs localization in cells. The agglomerated Citrate-IONPs (close to micrometer size) (Figure 6.3A) with their primary size around 10 nm (Figure 6.3B) were observed inside the bEnd.3 cells.

CNA-IONPs showed very different cell association and flux patterns compared with Citrate-IONPs. The flux of CNA-IONPs was significantly increased from 1 to 30 h in the AMF-induced hyperthermia group compared with the control and conventional hyperthermia groups (Figure 6.2D). The flux of CNA-IONPs was overall higher in the conventional hyperthermia group then control; however, they were not significantly different (Figure 6.2E). The P_{app} of LY and CNA-IONPs were similar in both the control and conventional hyperthermia groups. However, the P_{app} of LY ($F(2,7) = 280$, $P < 0.0001$) and CNA-IONPs ($F(2,7) = 19$, $P < 0.0016$) in the AMF-induced hyperthermia group significantly increased 90% and 148% respectively compared with control (Table 6.1). Trypan blue exclusion test results showed no observed cell death in any experiments. Meanwhile, analysis of iron concentration showed CNA-IONP cell association or cell uptake increased, but not significantly, in the AMF-induced

hyperthermia group compared with the control and conventional hyperthermia groups analyzed by iron concentrations (Figure 6.2F). CNA-IONPs cell association was at least 10 times lower compared with Citrate-IONPs (Figure 6.2F vs. 6.2C; Figure 6.3C vs. 6.3B). Less CNA-IONP cell uptake agreed with our TEM results. After analysis of three separately prepared TEM samples and two sections from each sample, CNA-IONPs were found occasionally in three samples (Figure 6.3C).

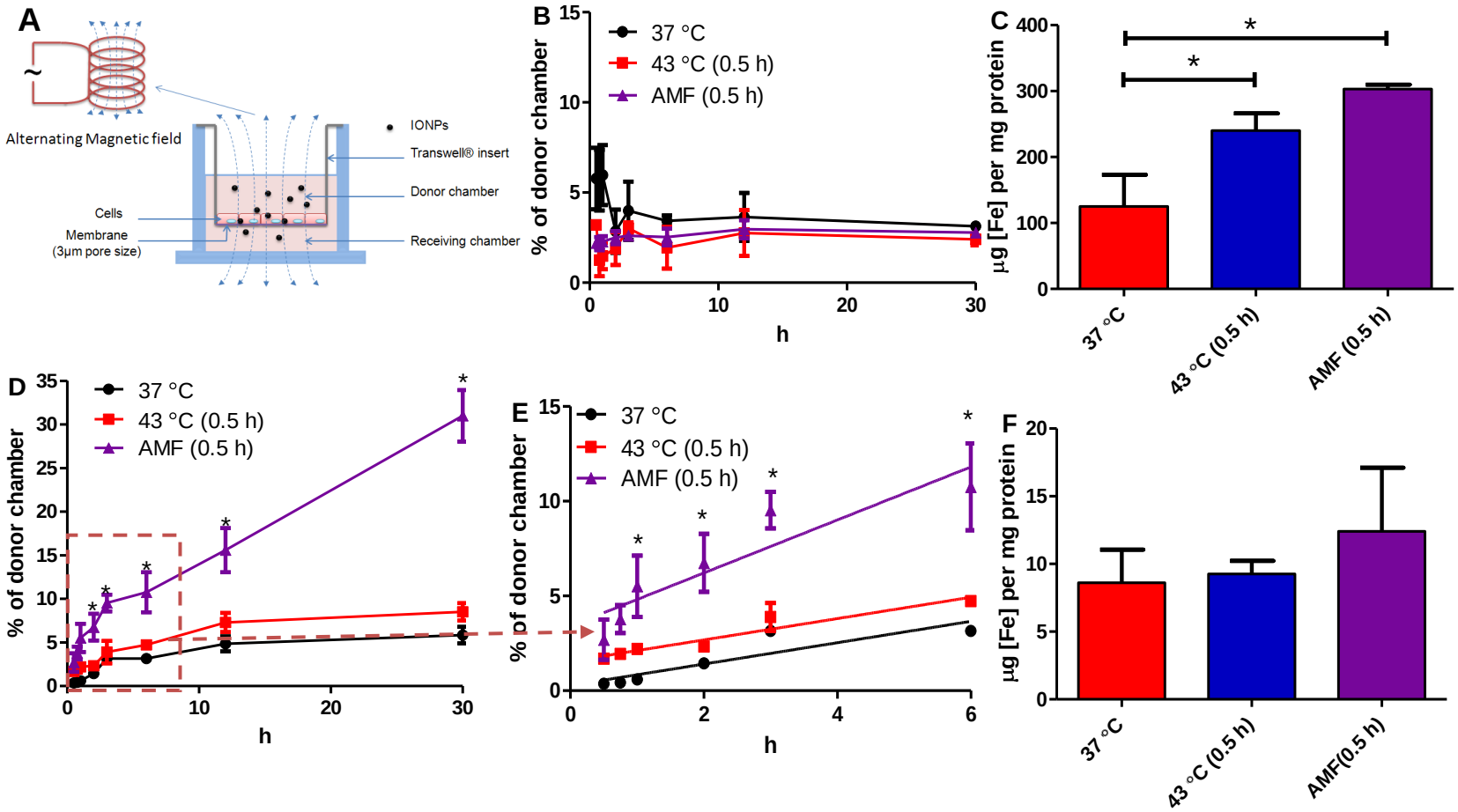
A
Alternating Magnetic field
IONPs
Transwell® insert
Donor chamber
Cells
Membrane
(3µm pore size)
Receiving chamber
B
37 °C
43 °C (0.5 h)
AMF (0.5 h)
% of donor chamber
h
C
µg [Fe] per mg protein
37 °C
43 °C (0.5 h)
AMF (0.5 h)
D
37 °C
43 °C (0.5 h)
AMF (0.5 h)
% of donor chamber
h
E
37 °C
43 °C (0.5 h)
AMF (0.5 h)
% of donor chamber
h
F
µg [Fe] per mg protein
37 °C
43 °C (0.5 h)
AMF(0.5 h)

Figure 6.2. Citrate-IONP and CNAs-IONP flux across bEnd.3 cells and cell association results. Schema of the Transwell® system and AMF used for flux studies (A). Citrate-IONPs flux across bEnd.3 cells (B) and cell association with bEnd.3 cells (C) at 37°C (n = 3) for 30 h, conventional hyperthermia at 43°C (0.5 h, n = 3) followed by 37°C for 30 h or AMF-induced hyperthermia (0.5 h, n = 3) followed by 37°C for 30 h. CNAs-IONPs flux across bEnd.3 cells (D), liner regression of the first 6 h CNAs-IONPs flux data (E) and bEnd.3 cell association (F) at 37°C (n = 3) for 30 h, conventional hyperthermia at 43°C (0.5 h, n = 3) followed by 37°C for 30 h or AMF-induced hyperthermia (0.5 h, n = 4) followed by 37°C for 30 h. * Significantly different compared to 37 °C in panel C ($F(2,6) = 24$, $P < 0.0014$). * Significantly different compared to 37 °C and conventional hyperthermia in panel D and E ($F(2,48) = 121$, $P < 0.0001$).

The LY results showed that the bEnd.3 BBB model showed high paracellular pathway flux (Table 6.1), which may mimic a 'leaky' BBB such as the blood tumor barrier (BTB). For this study, it was also crucial to use an *in vitro* model which can form tight junctions to predict how AMF-induced hyperthermia increases CNA-IONP flux *in vivo* since AMF-induced hyperthermia significantly increased the paracellular flux. After we tested CNA-IONPs trafficking across the bEnd.3 monolayer, CNA-IONPs flux was investigated using a 'tighter' BBB Transwell® model - MDCKII to gain better understanding how conventional hyperthermia and AMF-induced hyperthermia influence the paracellular pathway.

6.3.3. CNA-IONPs flux and cell association using MDCKII in vitro BBB model

MDCKII cells were grown as a monolayer on Transwell® inserts. Three to 4 days after cell seeding when resistance was > 170 Ω/cm^2 flux experiments were conducted. Lucifer yellow P_{app} was at $0.49 \pm 0.033 \times 10^{-6}$ cm/s (Table 6.1).

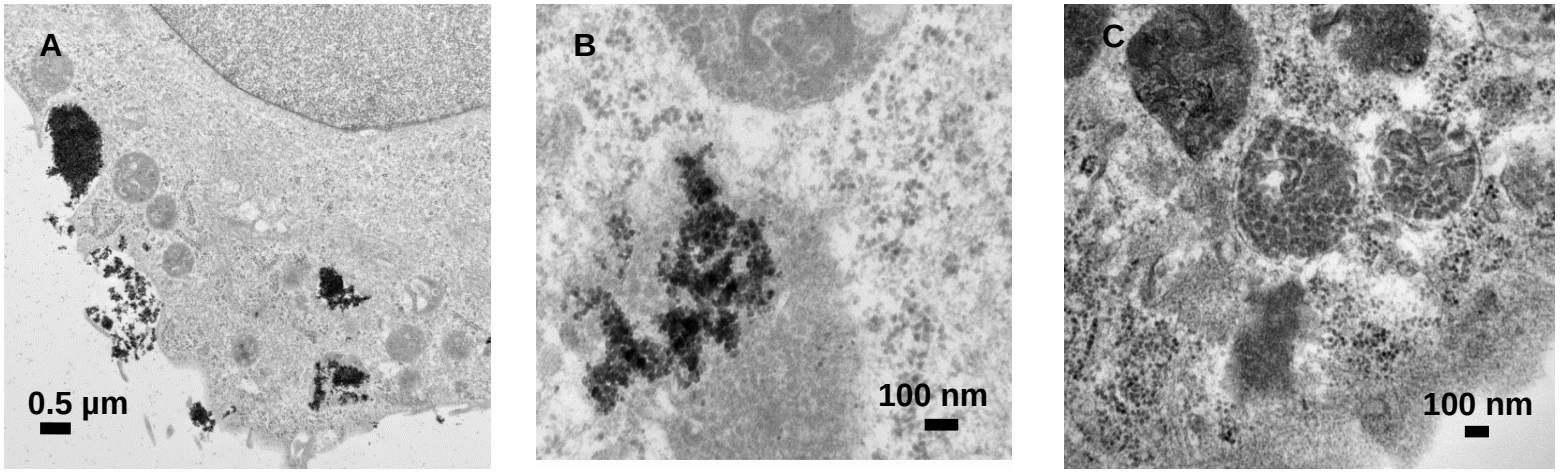

Figure 6.3. Transmission electron microscopy results of the cellular localization of the Citrate-IONPs (0.05 mg/ml) (A and B) and CNA-IONPs (0.05 mg/ml) (C) in bEnd.3 cells at 2 h.

LY significantly increased in the AMF-induced hyperthermia group from 2 to 6 h compared with the control and conventional hyperthermia groups (Figure 6.4A). CNA-IONP flux increased in the AMF-induced hyperthermia group (Figure 6.4B). The P_{app} of LY ($F(2,7) = 7$, $P < 0.019$) and CNA-IONPs ($F(2,7) = 27$, $P < 0.0005$) in the AMF group increased 23% and 123%, respectively compared with control using MDCKII Transwell® model (Table 6.1). The MDCKII cell uptake or cell association of CNA-IONPs was also significantly increased in the AMF-induced hyperthermia group compared to the control and conventional hyperthermia groups ($F(2,7) = 10$, $P < 0.0081$) (Figure 6.4C). Trypan blue exclusion test results showed no observed cell death in any experiments. In both MDCKII and bEnd.3 models, AMF-induced hyperthermia significantly increased LY and CNA-IONP flux across the BBB monolayer but conventional hyperthermia did not. Numerous studies showed that conventional hyperthermia can increase BBB permeability, heat magnitude and duration dependently (60, 298). Our results showed that conventional hyperthermia for 0.5 h did not change the MDCKII *in vitro* BBB model permeability. The following study is to test the effect of different hyperthermia durations on paracellular flux in order to have better understanding of the differences between AMF-induced hyperthermia and conventional hyperthermia.

6.3.4. Effect of conventional hyperthermia on paracellular flux using MDCKII in vitro BBB model

The P_{app} of LY was 0.46 to 0.5 X 10^{-6} cm/s for the first 6 h after 0.5, 1, and 2 h exposure at 43 °C followed by 37 °C for 6 h. However, after incubation at 43 °C for 4 h, the P_{app} of

LY significantly increased 22% (P_{app}, 0.61 ± 0.05 X 10^{-6} cm/s) compared with control and similar to the P_{app} of LY in the AMF-induced hyperthermia group (Figure 6.5). The trypan blue exclusion test results showed no observed cell death in any experiments after 4 h at 43 °C followed by 36 h at 37 °C.

6.4. Discussion

Biocompatibility and stability in biological environments, such as cell culture medium or blood, are crucial for nanoparticles to serve as good candidates as carriers across the BBB (281, 291). In this study, we investigated Citrate-IONPs flux across the BBB at normal, conventional hyperthermia and AMF-induced hyperthermia conditions. Citrate-IONPs did not show any flux across bEnd.3 cells over 30 h. Citrate-IONPs agglomerated very rapidly in cell culture medium to > 400 nm (292), which may be too large to cross the BBB through the paracellular pathway (299). Even through Citrate-IONPs agglomerated close to micrometer size *in vitro*, they were still able to be taken up by BBB cells. The TEM results suggested that Citrate-IONPs were taken up by phagocytosis, consistent with a previous report that phagocytosis could engulf particles as large as 20 µm (300). Furthermore, citrate-IONP agglomerations were close to microsize and could not be measured by DLS after conventional hyperthermia at 43 °C and AMF-induced hyperthermia for 0.5 h. Citrate-IONPs agglomeration provided one of the explanations for higher bEnd.3 cell association in the conventional hyperthermia and AMF-induced hyperthermia groups. However, no transcytosis was observed over 30 h.

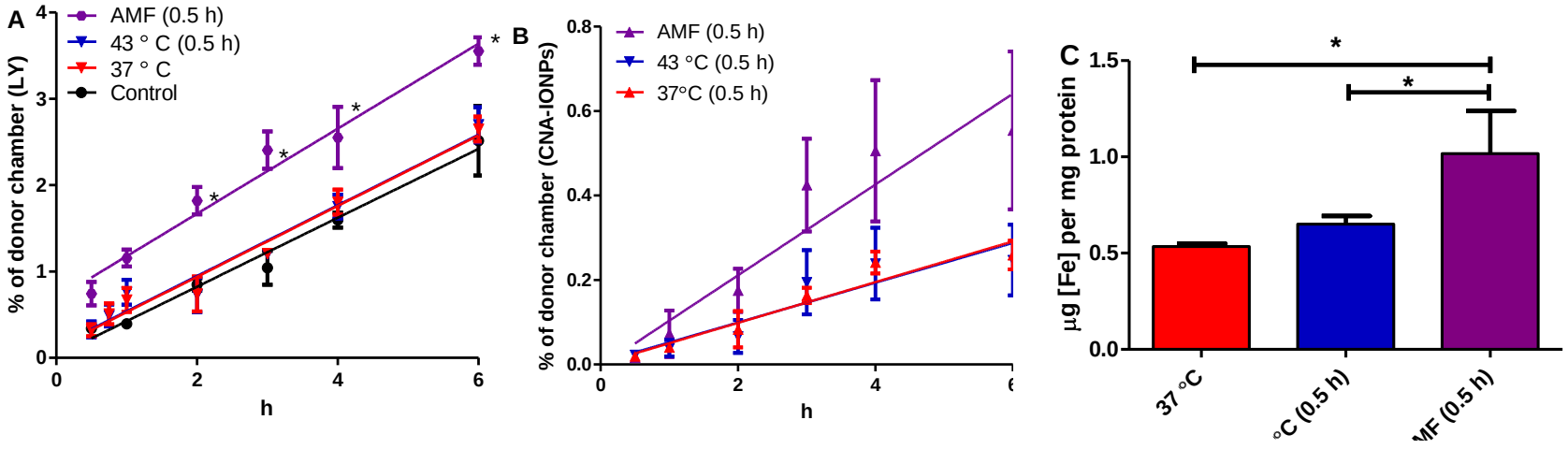

Figure 6.4. LY and CNA-IONP flux across the MDCKII cells and cell association results. LY flux (A), CNA-IONPs flux across MDCKII in vitro BBB model (B) and CNA-IONPs MDCKII cell association (C) after 37 °C (n = 3) for 6 h, conventional hyperthermia at 43 °C (0.5 h, n = 3) followed by 37 °C for 6 h or AMF-induced hyperthermia (0.5 h, n = 4)) followed by 37°C for 6 h. * Significantly different compared to control in panel A ($F(5,54) = 94$, $P < 0.001$). * Significantly different compared to AMF (0.5 h) ($F(2,7) = 10$, $P < 0.0081$).

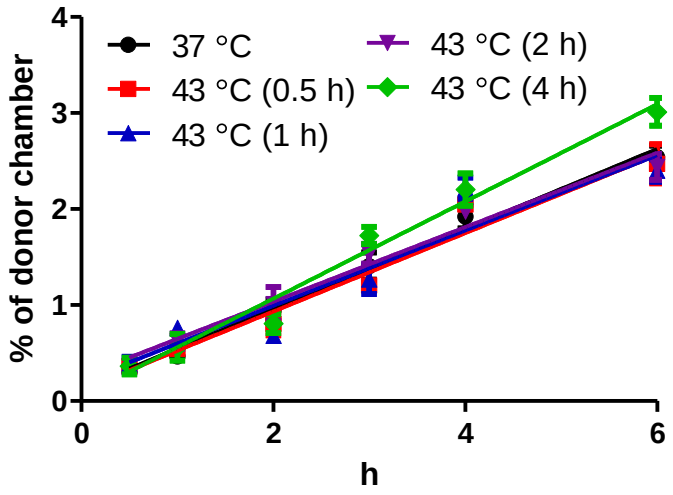

Figure 6.5. The effect of conventional hyperthermia on paracellular flux results. LY flux across MDCKII *in vitro* BBB model at 43 °C incubation for 0.5, 1, 2, and 4 h followed by 37 °C till 6 h

It's not surprising that Citrate-IONPs agglomerates did not show any flux over time across the highly regulated BBB *in vitro*. A high concentration of Citrate-IONPs in BBB cells related to toxicity, according to our previous research (292), and no transcytosis suggests they lack potential therapeutic CNS applications.

CNAs improved IONPs stability (size < 40 nm, Figure 6.1B) and biocompatibility without loss of AMF-induced hyperthermia and MRI T2 enhancement properties (292). In this study, Citrate-IONPs and CNA-IONPs showed completely different patterns of bEnd.3 cell association and flux across the BBB *in vitro*. CNA-IONP flux increased with time across bEnd.3 cells at 37 °C. However, less than 6 % of CNA-IONPs from the donor chamber crossed the bEnd.3 monolayer into receiving chambers over 30 h. Previous research demonstrated that different charged IONP fluxes were also studied using a

human brain derived BBB model. No IONPs fluxes were observed over 24 h under normal conditions (293). AMF-induced hyperthermia doubled the P_{app} of CNA-IONPs in the bEnd.3 model during the first 6 h. Thirty % of CNA-IONPs crossed the bEnd.3 monolayer at 30 h. The LY flux was also significantly increased which provides evidence that AMF-induced hyperthermia opened the paracellular pathway to increase CNA-IONP flux. The lack of observed cell death ruled out increased flux simply due to cell death. Meanwhile, the cell uptake/association of CNA-IONPs was ~ 10 times lower then Citrate-IONPs. The low cell uptake of CNA-IONPs was consistent with CNA-IONPs crossing the BBB mainly through the paracellular pathway after AMF-induced hyperthermia in the bEnd.3 *in vitro* BBB model. This is the first study showing that AMF-induced hypothermia significantly increased CNA-IONPs flux across a BBB model *in vitro* with low toxicity. AMF-induced hypothermia by IONPs is one approach to potentially increase BBB permeability and IONPs flux for diagnosis and therapy in the CNS.

The bEnd.3 cell as a BBB derived cell line suffers the problem that they (the junctions) cannot be "tight" enough to fully recapitulate the normal *in vivo* BBB. Madin-Darby canine kidney II (MDCKII) cells are known to form tight junctions very well with paracellular flux <1.5% of the donor dose per hour measured by inulin (301). Therefore, the non-cerebral cell line MDCKII was used as a surrogate *in vitro* BBB model (302) to study nanoparticle flux (303). In the present paper, we used bEnd.3 and MDCKII cell lines as two common *in vitro* BBB models to evaluate CNA-IONP uptake, cell effects and CNA-IONP flux under AMF-induced hyperthermia and conventional hyperthermia

conditions. After 0.5 h conventional hyperthermia treatment, CNA-IONP flux across the bEnd.3 monolayer was overall higher, but not significantly, compared with control (37 °C), but no differences was observed using MDCKII cells. The P_{app} of LY in the AMF groups increased 90% in the bEnd.3 model v.s. 20% in the MDCKII model compared to the control. AMF-induced hyperthermia increased the P_{app} of CNA-IONPs 148% in the bEnd.3 model and 128% in the MDCKII model. In general, a similar trend was observed with BBB permeability changes by AMF-induced hyperthermia using the two *in vitro* BBB models. However, the 'leaky' bEnd.3 Transwell® model's paracellular pathway flux was more sensitive to conventional hyperthermia and AMF-induced hyperthermia compared with MDCKII cells. Previous studies also showed a threshold at 43 °C for BBB disruption induced by conventional hyperthermia in normal brain tissue (298, 304). However, in a leaky BBB, such as the BTB, which was more sensitive to conventional hyperthermia, permeability increases at a lower temperature (305). The bEnd.3 Transwell® model can provide insight on the effect of AMF-induced hyperthermia on leaky BBB conditions such as the BTB. Even though MDCKII cells are not a blood-brain barrier derived cell line, they were shown to be a good *in vitro* model to predict the extent of brain exposure and the rate of brain uptake *in vivo* for several CNS drug candidates (306). Comparisons of these two in vitro BBB models, MDCKII cells produce a better *in vitro* model to predict whether AMF-induced hyperthermia changes paracellular flux in normal brain tissue because they form tight junctions very well. Because of the unique physicochemical properties and different cell association mechanisms of nanoparticles compared with small drug candidates, further studies were needed to investigate the

correlation between nanoparticle flux across the bEnd.3 and MDCKII Transwell® models and the BBB *in vivo*.

We also tested whether AMF-induced hyperthermia influences the cell association of CNA-IONPs using both cell lines. AMF-induced hyperthermia increased CNA-IONPs cell uptake/association in bEnd.3 cells and significantly increased cell uptake/association in MDCKII cells. Several studies showed that mild hyperthermia induced by ultrasound can enhance the intracellular uptake/association of polymeric micelles by increasing the diffusion of micelles and/or ultrasound-induced perturbation of cell membranes (307, 308). We are not aware of any report on cell uptake/association enhancement by AMF-induced hyperthermia. Furthermore, the P_{app} of CNA-IONPs increased more than the P_{app} of LY suggesting AMF-induced hyperthermia increased transcellular flux. How AMF-induced hyperthermia enhances CNA-IONP cell uptake and transcytosis needs to be explored. Compared with MDCKII cells, CNA-IONP cell uptake by bEnd.3 cells was ~10 times higher. MDCKII cells have good paracellular permeability characteristics; however, there are major differences between MDCKII epithelial and brain endothelial cells, such as expression of different transporters (309). Taken together, different models might be suitable to address different questions of BBB function. The brain endothelial cell line bEnd.3 model might be suitable to address IONPs cell uptake and non-brain derived MDCKII cells provide a good model to test BBB permeability.

The potential application of conventional hyperthermia to increase BBB permeability has been investigated for decades (58, 60). However, the difference between conventional

hyperthermia and AMF-induced hyperthermia on the BBB permeability was not studied before. Our results showed that the P_{app} of LY and CNA-IONPs significantly increased 79% and 148%, respectively, in the AMF-induced hyperthermia group compared with the conventional hyperthermia group. There was no significant difference between 37 °C and 43 °C groups, suggesting AMF-activation of CNA-IONPs increased the BBB permeability not only by simple heating but also other factors such as IONP vibration or IONP surface temperature vs. surroundings temperature. The temperature we measured was the environmental temperature in the Transwell® rather than the surface temperature of IONPs. Previous research showed that IONP surface temperature can be up to 20 °C higher relative to the surrounding regions (310). The temperature on the surface of cells may be higher than we measured using the temperature probe. Another possibility is that CNA-IONPs can bind to the cell surface and vibrate under AMF, mechanically increasing BBB permeability. Other research demonstrated that cell surface bound IONPs can mechanically activate certain cell surface receptors (311). However, further research needs to be done to investigate how CNA-IONPs associate with BBB cells and the role of temperature and mechanical effects on BBB permeability.

We further tested how different durations of conventional hyperthermia exposure at 43 °C influence paracellular pathway compared with AMF-induced hyperthermia. Our results showed that conventional hyperthermia (43 °C) did not influence the paracellular flux up to 2 h and that flux significantly increased at 43 °C after 4 h. A previous whole body hyperthermia study on rats also showed BBB permeability changes were highly dependent on heat magnitude and duration. No BBB permeability change was observed

(within 2 h) under whole body hyperthermia, but BBB permeability was increased after 4 h whole body hyperthermia (60). We did not observe any cell death even after 4 h conventional hyperthermia at 43 °C. However, whole body hyperthermia leads to heat stress *in vivo* causing numerous CNS toxicities such as edema, spontaneous electroencephalogram and neuronal damage (312). Our results also showed that the P_{app} of LY after conventional hyperthermia at 43 °C for 4 h was similar to the P_{app} of LY at AMF-induced hyperthermia for 0.5 h. AMF-induced hyperthermia can increase BBB permeability similar to conventional hyperthermia at lower temperature and shorter time without cell death *in vitro*. Previous research showed that half an hour AMF-induced hyperthermia killed head and neck cancer cells in mice without harming any normal cells (313). However, the toxicity of AMF-induced hyperthermia on the BBB *in vivo* needs to be investigated. AMF-induced hyperthermia showed potential advantage to increase BBB permeability more effectively with low toxicity compared with conventional hyperthermia, suggesting potential therapeutic application.

6.5. Conclusions

CNA-IONPs showed low flux across the BBB under normal conditions in both b.End3 and MDCKII *in vitro* BBB models. AMF-induced hyperthermia (0.5 h) enhanced CNA-IONPs flux and cell association using both b.End3 and MDCKII BBB models in the absence of cell death. However, conventional hyperthermia at 43 °C did not increase the BBB permeability up to 2 h. AMF-induced hyperthermia at 41 °C (0.5 h) enhanced BBB permeability similar to conventional hyperthermia at 43 °C for 4 h. Altogether these results suggested that AMF-induced hyperthermia enhanced the BBB association and

permeability of CNA-IONPs more effectively than conventional hyperthermia. AMF-induced hyperthermia provides an approach to deliver IONPs across the BBB with low toxicity for potential therapeutic and diagnostic applications in the CNS.

Chapter 7 Conclusions and future studies

With the rapid surge in the development of metal-based ENMs, it is critical to understand how ENMs were handled in the biological system and to identify physicochemical properties most relevant to their biological properties that best predict ENM response. This information will guide researchers to design and engineer ENMs with desirable properties to change their behavior in the biological system and avoid undesirable outcomes. The guiding hypothesis for this dissertation is that the physicochemical properties of metal-based ENMs change their pharmacokinetics, especially BBB association and flux. In this dissertation, Chapters 3 and 4 used ceria ENMs as a metal-based ENM model to study their pharmacokinetics in blood and BBB association properties. Then Chapters 5 and 6 developed an optimized multifunctional IONP for potential biomedical application in the CNS according to the results from Chapters 3 and 4.

First, we proved our first hypothesis that ceria ENMs demonstrated different pharmacokinetic profiles compared with the cerium ion. Furthermore, different sizes and shapes of ceria ENMs showed size-dependent blood concentrations and blood circulation time supporting our second hypothesis in chapter 3. Five nm ceria ENM showed significantly higher blood concentration compared with the other 3 sizes ten min after infusion. The high hydrophilicity of ENMs and small size may have contributed to slower clearance from the blood (194, 314). Ceria ENMs larger than 5 nm were very rapidly

cleared from circulating blood. Fifteen and thirty nm ceria ENMs showed different blood cell association behavior compared with other sizes, which agrees with previous studies that the critical size of ENMs plays a very important role on cell association and uptake (83, 149, 150). After ceria ENMs distributed in the blood, our next hypothesis is that ceria ENMs can associate with and flux across the BBB. The *in situ* brain perfusion technique was used to study ceria ENM flux and brain vascular cell associations. This is the first report of ceria ENM interaction with the BBB *in vivo* under conditions that control ENM chemistry. Five nm ceria ENMs associated with the capillary luminal wall rather than appearing inside the brain parenchyma. This result showed that the flux of ceria ENMs across the healthy BBB is very limited. A recent published review summarized the BBB permeability of metal and metal oxide ENMs and the results from 30 different metal-base ENM demonstrated bran entry is very challenging in general (200). Most of these studies only analyzed the whole brain concentrations of ENMs. The present study was the first study to specifically demonstrate ceria ENM distribution between the BBB and brain parenchyma. These results provide important information to design a ceria ENMs to cross the BBB for their therapeutic applications for neurodegenerative diseases and their potential toxicity on the BBB cells. Meanwhile, capillary luminal wall association provides the possibility for redistribution back to blood which lead to nontraditional pharmacokinetic profiles, as we showed in our pharmacokinetic study of different size ceria ENMs (259).

Second, we hypothesized that multifunctional CNA-IONPs will have optimized physicochemical properties to improve the stability and biocompatibility of IONPs

compared to the results from the citrate-coated ceria ENMs studies. The stability of CNA-IONPs in cell culture medium was significantly improved with a size around 30 nm compared with citrate-IONPs. Furthermore, CNAs significantly decreased the toxicity of IONPs *in vitro* with enhanced superparamagnetic properties such as MRI T2 contrast and hyperthermia abilities (196). CNA-IONPs with improved biocompatibility and stability in biological environments serve as good candidates as carriers to cross the BBB (281, 291). However, the study in chapter 4 showed that even in the absence of agglomeration, the flux of metal-based ENMs across healthy BBB was very limited (199). In chapter 6, we hypothesized that AMF-induced hyperthermia would significantly increase the paracellular and/or transcellular flux of IONPs, and influence the BBB cell association with IONPs compared with conventional hyperthermia. Our results showed that AMF-induced hyperthermia significantly increased CNA-IONP flux across the BBB, which increased the paracellular and transcellular flux without apparent toxicity. AMF-induced hyperthermia provides the potential to overcome some side effects of conventional hyperthermia on the BBB. In summary, metal-based ENMs have different pharmacokinetic behaviors because of their unique physicochemical properties compared with their constituent metal. The stability and physicochemical properties of metal-based ENMs are critical for their pharmacokinetics in blood and their biological barrier association such as the BBB. Even though metal-based ENMs without special surface modification have limited ability to cross the healthy BBB, researchers are taking advantage of metal-based ENMs' unique properties such as hyperthermia to enhance the BBB flux of IONPs with low toxicity.

The research presented in this dissertation provides a starting point for future studies. It has been shown that ENMs are rapidly coated with plasma proteins and other circulating substances, which create a corona around the ENM (254, 255). The protein coating of citrate-coated ENMs might change their pharmacokinetics in blood and cell association. We are not aware of any reports of ceria uptake into blood cells or platelets other than our prior finding suggesting a small amount of a 30 nm ceria ENM might have entered red blood cells after 1 h *in vitro* (7). A systematic research on different size ceria ENMs association with proteins in the blood and blood cells will provide potential explanations for their unique pharmacokinetic profiles in the blood. Furthermore, protein association on the surface of ENMs is a dynamic process. It is crucial to investigate the dynamic changes of the protein corona to predict the biological response changes of ENMs *in vivo*. Because of the unique properties of ENMs, such as protein corona, adhesion and phagocytic uptake compared with small molecules, new pharmacokinetic models should be developed such as a PBPK to predict the time-dependent changes of ceria ENM distribution in tissues and blood (232, 238). After blood distribution, ENM interaction with biological barriers including cell association/ dissociation, cell uptake, and transcytosis will determine their fate in biological systems. We observed the 5 nm ceria associated on the surface of the BBB cells 2 min after infusion. A better understanding of ENM interaction process with the BBB over time will provide evidence to explain the nontraditional pharmacokinetic behavior such as concentrations increasing over time after iv injection. This information will also help us to design optimized ENMs with desirable biological properties such as the increased BBB association or prolonged circulation times.

With this fundamental information on the pharmacokinetics of metal-based ENMs in hand, we developed a polymer based ENMs loaded with IONPs with improved stability and biocompatibility *in vitro* (196). More studies are needed to investigate their pharmacokinetics such as half-life and clearance *in vivo*, which are important for passive targeting for certain organs (315). More importantly, for biomedical applications, it is critical to test whether they can accumulate at target organs such as tumors, cross biological barriers such as the BBB and their potential toxicity *in vivo*. ENMs with different physicochemical properties cross the BBB through various mechanisms as discussed in 2.3.3. However, little research has been reported on the paracellular and transcellular flux of ENMs across the BBB and how the flux can be increased or decreased by surface modification or unique properties of ENMs. Our results showed that AMF-induced hyperthermia using IONPs can increase IONPs flux *in vitro*. However, this monolayer BBB *in vitro* model cannot mimic the BBB *in vivo*. An *in vivo* study will be needed to test whether AMF-induced hyperthermia can effectively open the BBB without causing major toxicity. Our results also showed that AMF-induced hyperthermia increased the BBB permeability more effectively in a 'leaky' BBB *in vitro* model. Since the BBB will become leakier because of the brain tumor, the effect of AMF-induced hyperthermia using IONPs on the blood tumor barrier permeability needs to be investigated for their potential brain tumor therapeutic or diagnostic applications.

In conclusion, this work yielded valuable information in regards to metal-based ENMs for brain delivery and ENMs in general. The pharmacokinetic study of ceria ENMs may

be relevant to most citrate-coated metal-based ENMs and provide evidence that size plays important role on ENMs' fate in biological system. This points to the importance of analyzing metal-based ENMs to identify their unique pharmacokinetics properties, which determine their potential biomedical applications. It is also possible that ceria ENM interaction with the BBB may be applied in other metal-based ENMs, which provides important information for future applications of metal-based ENMs in the CNS. CNA-IONPs demonstrated that CNAs have the potential to significantly improve the stability and biocompatibility of metal-based ENMs, which are very important for any biomedical applications. Metal-based ENMs are promising because of their unique properties compared with other ENMs. AMF-induced hyperthermia using CNA-IONPs can increase the BBB permeability, demonstrating the possibility of other metal-based ENMs generating heat for this application.

Appendices

This section contains the following additional information:

Appendix A: Abbreviations

Appendix B: Supplementary Information to chapter 6

Appendix A Abbreviations

ABC	ATP-binding cassette
AMF	Alternating magnetic field
BBB	Blood-brain barrier
CED	Convention-enhanced delivery
CNAs	Cross-linked nanoassemblies
CNS	Central nervous system
CTAB	Hexadecyltri-methylammonium bromide
DIUF	Deionized ultra filtered water
DLS	Dynamic light scattering
EPR	Enhanced permeability and retention
FCC	Face-centered cubic
Gd-DTPA	Gadolinium-diethylenetriaminepentaacetic acid
ICP-MS	Inductively coupled plasma mass spectrometry
ICV	Intra-cerebro-ventricular
IONPs	Iron oxide nanoparticles
LM	Light microscopy
EM	Electron microscopy
LRP1	Low-density lipoprotein receptor-related protein-1
LY	Lucifer yellow
MCT	Monocarboxylate transporters
MPS	Mononuclear phagocyte system
MRI	Magnetic resonance imaging
MRT	Mean residence time
NIR	Near infra-red
OCT	Optical coherence tomography
PEG-p(Asp)	Poly(ethylene glycol)-poly(aspartate)
PEPE	Polyether-copolyester
P-gp	P-glycoprotein
PSD	Particle size distribution
TEER	Transendothelial electrical resistance
TEM	Transmission electron microscopy
Tf	Transferrin
TMC	Trimethylated chitosan
TNF-α	Necrosis factor alpha
XRD	X–ray diffraction

Appendix B Supplementary Information to chapter 6

B.6.1. Method

B.6.1.1. Materials

The chemicals used to prepare the Citrate-coated IONPs (Citrate-IONPs) and cross-linked nanoassemblies loaded with superparamagnetic iron oxide nanoparticles (CNA-IONPs) have been described (292).

B.6.1.2. Preparation and characterization of Citrate-IONPs and CNA-IONPs

Citrate-IONPs and CNA-IONPs were synthesized using a previously reported method (55, 186, 292). Briefly, ferric chloride hexahydrate (Fe^{3+}) and ferrous chloride tetrahydrate (Fe^{2+}) were dissolved in deionized water (Fe^{3+} Fe^{2+} = 2:1), followed by adding ammonium hydroxide dropwise under an N_2 atmosphere at 85 ºC. Citric acid (2 equivalent) was then added to prepare Citrate-IONPs. After 1 h, the solution was placed on a magnet to collect black brown particles, which were washed repeatedly using pure ethanol (274, 275). Citrate-IONPs were dried overnight in a vacuum drying oven.

CNA-IONPs were prepared similarly by mixing ferric and ferrous salts at a 2:1 molar ratio with CNAs in deionized water. The total iron ions and the carboxyl groups of CNAs were adjusted in a molar ratio of 1:2. Ammonium hydroxide was added to this mixed solution dropwise under nitrogen atmosphere and the reaction was allowed to proceed at 85°C for 1 h. The solution was centrifuged at 3,000 g for 5 min to remove precipitates and other water-insoluble impurities. CNA-IONPs in the supernatant were filtered (0.22 µm syringe filters), dialyzed (MWCO 6 ~ 8 kDa), and collected by freeze drying. The physico-chemical properties and stability of the Citrate-IONPs and CNA-IONPs were

determined in our laboratories. All of the methods have been reported in our previous report (292).

B.6.1.3. Cell lines and culture conditions

The immortalized mouse brain endothelial cell line bEnd.3 (American Type Culture Collection, Manassas, VA) was cultured in Dulbecco's Modified Eagle Medium (DMEM, Mediatech, Manassas, VA) with 10% fetal bovine serum (FBS, Atlanta Biologicals, Lawrenceville, GA), 100 U/ml penicillin, and 100 mg/ml streptomycin (Invitrogen, Grand Island, NY) at 37ºC in a humidified incubator with 5% CO_2 and used from passages 5 through 10. Madin-Darby canine kidney II (MDCKII) cells (European Collection of Cell Cultures, Salisbury, UK) were cultured in minimum essential medium with Earle's salts (MEM, Mediatech, Manassas, VA) with 5% FBS, 100 U/ml penicillin, and 100 mg/ml streptomycin at 37 ºC in a humidified incubator with 5% CO_2 and used from passages 45 through 60.

B.6.1.4. Transwell cultures

bEnd.3 cells were seeded on Transwell® filters (polycarbonate 12 mm, pore size 3.0 µm, Corning Costar, Lowell, MA) in a density of 200,000 cells/cm^2. The flux assays were performed 7-10 days after seeding (297). MDCKII cells were seeded on Transwell® filters in a density of 200,000 cells/cm^2 and the flux assays were performed 4 days after seeding (296).

B.6.1.5. Iron concentration analyzed by Ferrozine assay

A ferrozine assay for iron was carried out to determine the iron content of the nanoparticle solutions, the cell culture media, the nanoparticle-loaded cells and the control cells, (316, 317). The cell suspension or nanoparticle solution was diluted to appropriate concentration. Fifty µL samples were mixed with 50 µL of 1.4 mM HCl and 20 µL ascorbic acid (2M), and then incubated at 70 °C for 1 hour. After the mixtures cooled to room temperature, 30 µL of the iron detection reagent (6.5 mM ferrozine, 6.5 mM neocuproine, 2.5 M ammonium acetate and 1 M ascorbic acid dissolved in water) was added to each sample. After 30 min, the solution in each tube was transferred into a well of a 96 well plate and the absorbance measured at 550 nm on a microplate reader. A standard curve was also prepared with 0, 0.1, 0.2, 0.5, 1, 2, 5 and 10 µg/mL iron and treated in the same way.

B.6.1.6. The effect of temperature and CNA-IONPs concentrations on CNA-IONPs flux using MDCKII Transwell® model

CNA-IONP and LY fluxes were also investigated with two concentrations (0.5 mg/ml and 2.5 mg/ml CNA-IONP) at 37 and 43 °C (0.5 h). Samples (100 µL) were collected from the donor chamber at time 0 and from the receiving chamber at 0.5, 0.75, 1, 2, 3, 4, and 6 h. LY concentrations was analyzed as described in the method section of this report and iron concentrations were analyzed as described above.

B.6.2. Results

CNA-IONPs fluxes were studied at 37 °C and 43 °C (0.5 h) with two concentrations (0.5 mg/ml or 2.5 mg/ml). Neither temperature or concentration increased the flux of CNA-IONPs and LY over 6 h and the total flux of CNA-IONPs was less than 0.2% of donor chamber over 6 h (Figure B.6.1A& B.6.1B). The concentration independence of CNA-IONP flux across the BBB provided evidence that CNA-IONPs cross the BBB through non-diffusion mechanism. This very limited IONPs flux across the BBB was consistent with a previous report. . They did not observe any IONPs flux over 24 h under normal conditions using a human brain derived BBB model (293).

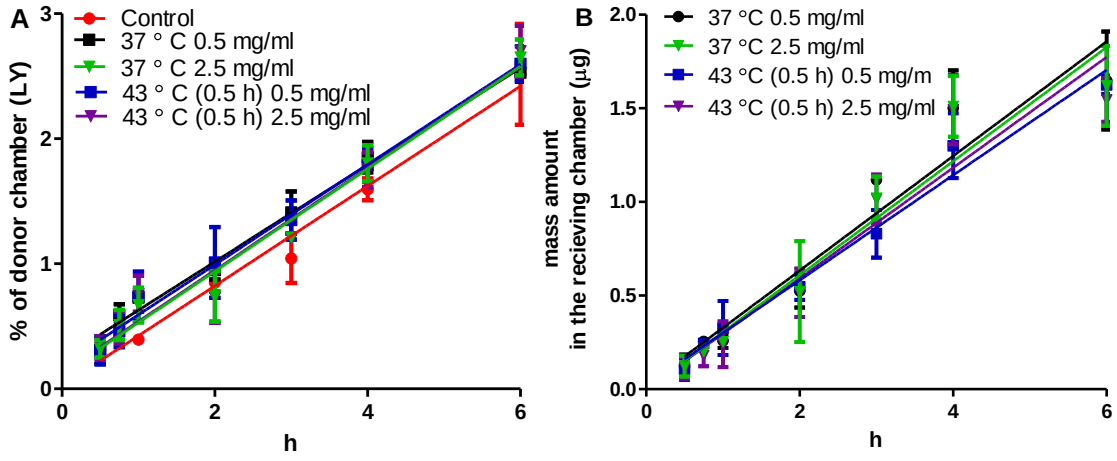

Figure B.6.1. LY (A) and CNA-IONP (B) flux across MDCKII transwell® model at two different concentrations (0.5 and 2.5 mg/mL) and temperatures (37 and 43 °C) (n = 3 in each group).

References

1. J.M. Hu, Y.F. Qian, X.F. Wang, T. Liu, and S.Y. Liu. Drug-Loaded and superparamagnetic iron oxide nanoparticle surface-embedded amphiphilic block copolymer micelles for integrated chemotherapeutic drug delivery and MR imaging. Langmuir. 28:2073-2082 (2012).
2. W.L. Jiang, H. Xie, D. Ghoorah, Y.L. Shang, H.J. Shi, F. Liu, X.L. Yang, and H.B. Xu. Conjugation of Functionalized SPIONs with Transferrin for Targeting and Imaging Brain Glial Tumors in Rat Model. PLoS One. 7: (2012).
3. J. Zeng, Q. Zhang, J. Chen, and Y. Xia. A comparison study of the catalytic properties of Au-based nanocages, nanoboxes, and nanoparticles. Nano Lett. 10:30-35 (2010).
4. Q. Huo. A perspective on bioconjugated nanoparticles and quantum dots. Colloids Surf B Biointerfaces. 59:1-10 (2007).
5. R.A. Sperlingand W.J. Parak. Surface modification, functionalization and bioconjugation of colloidal inorganic nanoparticles. Philos Transact A Math Phys Eng Sci. 368:1333-1383 (2010).
6. G. Sonavane, K. Tomoda, and K. Makino. Biodistribution of colloidal gold nanoparticles after intravenous administration: Effect of particle size. Colloids and Surfaces B-Biointerfaces. 66:274-280 (2008).
7. R.A. Yokel, R.L. Florence, J.M. Unrine, M.T. Tseng, U.M. Graham, P. Wu, E.A. Grulke, R. Sultana, S.S. Hardas, and D.A. Butterfield. Biodistribution and oxidative stress effects of a systemically-introduced commercial ceria engineered nanomaterial. Nanotoxicology. 3:234-248 (2009).
8. S.S. Hardas, D.A. Butterfield, R. Sultana, M.T. Tseng, M. Dan, R.L. Florence, J.M. Unrine, U.M. Graham, P. Wu, E.A. Grulke, and R.A. Yokel. Brain distribution and toxicological evaluation of a systemically delivered engineered nanoscale ceria. Toxicol Sci. 116:562-576 (2010).
9. A.S. Karakoti, N.A. Monteiro-Riviere, R. Aggarwal, J.P. Davis, R.J. Narayan, W.T. Self, J. McGinnis, and S. Seal. Nanoceria as antioxidant: synthesis and biomedical applications. JOM. 60:33-37 (2008).
10. R.W. Tarnuzzer, J. Colon, S. Patil, and S. Seal. Vacancy engineered ceria nanostructures for protection from radiation-induced cellular damage. Nano Letters. 5:2573-2577 (2005).
11. J. Niu, A. Azfer, L.M. Rogers, X. Wang, and P.E. Kolattukudy. Cardioprotective effects of cerium oxide nanoparticles in a transgenic murine model of cardiomyopathy. Cardiovasc Res. 73:549-559 (2007).
12. T. Xia, M. Kovochich, M. Liong, L. Madler, B. Gilbert, H. Shi, J.I. Yeh, J.I. Zink, and A.E. Nel. Comparison of the mechanism of toxicity of zinc oxide and cerium oxide nanoparticles based on dissolution and oxidative stress properties. ACS Nano. 2:2121-2134 (2008).
13. D. Schubert, R. Dargusch, J. Raitano, and S.W. Chan. Cerium and yttrium oxide nanoparticles are neuroprotective. Biochemical and Biophysical Research Communications. 342:86-91 (2006).
14. N. Singh, C.A. Cohen, and B.A. Rzigalinski. Treatment of neurodegenerative disorders with radical nanomedicine. Ann N Y Acad Sci. 1122:219-230 (2007).

15. B. D'Angelo, S. Santucci, E. Benedetti, S. Di Loreto, R.A. Phani, S. Falone, F. Amicarelli, M.P. Ceru, and A. Cimini. Cerium oxide nanoparticles trigger neuronal survival in a human Alzheimer disease model by modulating BDNF pathway Current Nanoscience. 5:167-176 (2009).
16. J. Chen, S. Patil, S. Seal, and J.F. McGinnis. Rare earth nanoparticles prevent retinal degeneration induced by intracellular peroxides. Nat Nanotechnol. 1:142-150 (2006).
17. M. Das, S. Patil, N. Bhargava, J.F. Kang, L.M. Riedel, S. Seal, and J.J. Hickman. Auto-catalytic ceria nanoparticles offer neuroprotection to adult rat spinal cord neurons. Biomaterials. 28:1918-1925 (2007).
18. E. Hodgson. A textbook of Modern Toxicology, John Wiley & Sons. Inc., 2004.
19. E.J. Park, J. Choi, Y.K. Park, and K. Park. Oxidative stress induced by cerium oxide nanoparticles in cultured BEAS-2B cells. Toxicology. 245:90-100 (2008).
20. A. Thill, O. Zeyons, O. Spalla, F. Chauvat, J. Rose, M. Auffan, and A.M. Flank. Cytotoxicity of CeO_2 nanoparticles for *Escherichia coli*. Physico-chemical insight of the cytotoxicity mechanism. Environmental Science and Technology. 40:6151-6156 (2006).
21. T.J. Brunner, P. Wick, P. Manser, P. Spohn, R.N. Grass, L.K. Limbach, A. Bruinink, and W.J. Stark. *In vitro* cytotoxicity of oxide nanoparticles: comparison to asbestos, silica, and the effect of particle solubility. Environmental Science and Technology. 40:4374-4381 (2006).
22. H.J. Eom and J. Choi. Oxidative stress of CeO2 nanoparticles via p38-Nrf-2 signaling pathway in human bronchial epithelial cell, Beas-2B. Toxicology Letters. 187:77-83 (2009).
23. W. Lin, Y.W. Huang, X.D. Zhou, and Y. Ma. Toxicity of cerium oxide nanoparticles in human lung cancer cells. Int J Toxicol. 25:451-457 (2006).
24. E.-J. Park, W.-S. Cho, J. Jeong, J.-h. Yi, K. Choi, Y. Kim, and K. Park. Induction of inflammatory responses in mice treated with cerium oxide nanoparticles by intratracheal instillation. Journal of Health Science. 56:387-396 (2010).
25. H.E. Institute. Evaluation of human health risk from cerium added to diesel fuel, *Communication 9*, Health Effects Institute, Boston, MA, 2001.
26. S.M. Hirst, A. Karakoti, S. Singh, W. Self, R. Tyler, S. Seal, and C.M. Reilly. Bio-distribution and in vivo antioxidant effects of cerium oxide nanoparticles in mice. Environ Toxicol. 28:107-118 (2013).
27. R.A. Yokel, T.C. Au, R. MacPhail, S.S. Hardas, D.A. Butterfield, R. Sultana, M. Goodman, M.T. Tseng, M. Dan, H. Haghnazar, J.M. Unrine, U.M. Graham, P. Wu, and E.A. Grulke. Distribution, elimination, and biopersistence to 90 days of a systemically introduced 30 nm ceria-engineered nanomaterial in rats. Toxicol Sci. 127:256-268 (2012).
28. J. Bernacki, A. Dobrowolska, K. Nierwinska, and A. Malecki. Physiology and pharmacological role of the blood-brain barrier. Pharmacological Reports. 60:600-622 (2008).
29. E. Barbu, E. Molnar, J. Tsibouklis, and D.C. Gorecki. The potential for nanoparticle-based drug delivery to the brain: overcoming the blood-brain barrier. Expert Opin Drug Del. 6:553-565 (2009).

30. J. Kreuter and S. Gelperina. Use of nanoparticles for cerebral cancer. Tumori. 94:271-277 (2008).
31. L. Chen, R.A. Yokel, B. Hennig, and M. Toborek. Manufactured aluminum oxide nanoparticles decrease expression of tight junction proteins in brain vasculature. Journal of Neuroimmune Pharmacology. 3:286-295 (2008).
32. X. He, H. Zhang, Y. Ma, W. Bai, Z. Zhang, K. Lu, Y. Ding, Y. Zhao, and Z. Chai. Lung deposition and extrapulmonary translocation of nano-ceria after intratracheal instillation. Nanotechnology. 21:285103 (2010).
33. J.S. Weinstein, C.G. Varallyay, E. Dosa, S. Gahramanov, B. Hamilton, W.D. Rooney, L.L. Muldoon, and E.A. Neuwelt. Superparamagnetic iron oxide nanoparticles: diagnostic magnetic resonance imaging and potential therapeutic applications in neurooncology and central nervous system inflammatory pathologies, a review. J Cerebr Blood F Met. 30:15-35 (2010).
34. M. Wankhede, A. Bouras, M. Kaluzova, and C.G. Hadjipanayis. Magnetic nanoparticles: an emerging technology for malignant brain tumor imaging and therapy. Expert Rev Clin Pharmacol. 5:173-186 (2012).
35. A.H. Lu, E.L. Salabas, and F. Schuth. Magnetic nanoparticles: synthesis, protection, functionalization, and application. Angew Chem Int Ed Engl. 46:1222-1244 (2007).
36. M. Yanase, M. Shinkai, H. Honda, T. Wakabayashi, J. Yoshida, and T. Kobayashi. Intracellular hyperthermia for cancer using magnetite cationic liposomes: Ex vivo study. Japanese Journal of Cancer Research. 88:630-632 (1997).
37. M. Mahmoudi, S. Sant, B. Wang, S. Laurent, and T. Sen. Superparamagnetic iron oxide nanoparticles (SPIONs): development, surface modification and applications in chemotherapy. Adv Drug Deliv Rev. 63:24-46 (2011).
38. S.A. Meenach, K.W. Anderson, and J.Z. Hilt. Synthesis and characterization of thermoresponsive poly(ethylene glycol)-based hydrogels and their magnetic nanocomposites. J Polym Sci Pol Chem. 48:3229-3235 (2010).
39. A.K. Gupta and M. Gupta. Synthesis and surface engineering of iron oxide nanoparticles for biomedical applications. Biomaterials. 26:3995-4021 (2005).
40. B. Novotna, P. Jendelova, M. Kapcalova, P. Rossner, K. Turnovcova, Y. Bagryantseva, M. Babic, D. Horak, and E. Sykova. Oxidative damage to biological macromolecules in human bone marrow mesenchymal stromal cells labeled with various types of iron oxide nanoparticles. Toxicol Lett. 210:53-63 (2012).
41. M. Mahmoudi, H. Hofmann, B. Rothen-Rutishauser, and A. Petri-Fink. Assessing the In Vitro and In Vivo Toxicity of Superparamagnetic Iron Oxide Nanoparticles. Chem Rev (2011).
42. A. Beduneau, Z. Ma, C.B. Grotepas, A. Kabanov, B.E. Rabinow, N. Gong, R.L. Mosley, H. Dou, M.D. Boska, and H.E. Gendelman. Facilitated monocyte-macrophage uptake and tissue distribution of superparmagnetic iron-oxide nanoparticles. PLoS One. 4:e4343 (2009).
43. S.A. Meenach, J.Z. Hilt, and K.W. Anderson. Poly(ethylene glycol)-based magnetic hydrogel nanocomposites for hyperthermia cancer therapy. Acta Biomaterialia. 6:1039-1046 (2010).

44. M. Wagner, S. Wagner, J. Schnorr, E. Schellenberger, D. Kivelitz, L. Krug, M. Dewey, M. Laule, B. Hamm, and M. Taupitz. Coronary MR angiography using citrate-coated very small superparamagnetic iron oxide particles as blood-pool contrast agent: initial experience in humans. J Magn Reson Imaging. 34:816-823 (2011).
45. M. Di Marco, C. Sadun, M. Port, I. Guilbert, P. Couvreur, and C. Dubernet. Physicochemical characterization of ultrasmall superparamagnetic iron oxide particles (USPIO) for biomedical application as MRI contrast agents. Int J Nanomed. 2:609-622 (2007).
46. M. Safi, J. Courtois, M. Seigneuret, H. Conjeaud, and J.F. Berret. The effects of aggregation and protein corona on the cellular internalization of iron oxide nanoparticles. Biomaterials. 32:9353-9363 (2011).
47. K. Andreas, R. Georgieva, M. Ladwig, S. Mueller, M. Notter, M. Sittinger, and J. Ringe. Highly efficient magnetic stem cell labeling with citrate-coated superparamagnetic iron oxide nanoparticles for MRI tracking. Biomaterials (2012).
48. D. Farrell, S.A. Majetich, and J.P. Wilcoxon. Preparation and characterization of monodisperse Fe nanoparticles. J Phys Chem B. 107:11022-11030 (2003).
49. M. Kumagai, Y. Imai, T. Nakamura, Y. Yamasaki, M. Sekino, S. Ueno, K. Hanaoka, K. Kikuchi, T. Nagano, E. Kaneko, K. Shimokado, and K. Kataoka. Iron hydroxide nanoparticles coated with poly(ethylene glycol)-poly(aspartic acid) block copolymer as novel magnetic resonance contrast agents for in vivo cancer imaging. Colloid Surface B. 56:174-181 (2007).
50. D.H. Kim, E.A. Rozhkova, T. Rajh, S.D. Bader, and V. Novosad. Synthesis of hybrid gold/iron oxide nanoparticles in block copolymer micelles for imaging, drug delivery, and magnetic hyperthermia. IEEE T Magn. 45:4821-4824 (2009).
51. L.E. Euliss, S.G. Grancharov, S. O'Brien, T.J. Deming, G.D. Stucky, C.B. Murray, and G.A. Held. Cooperative assembly of magnetic nanoparticles and block copolypeptides in aqueous media. Nano Lett. 3:1489-1493 (2003).
52. J.F. Berret, N. Schonbeck, F. Gazeau, D. El Kharrat, O. Sandre, A. Vacher, and M. Airiau. Controlled clustering of superparamagnetic nanoparticles using block copolymers: Design of new contrast agents for magnetic resonance imaging. J Am Chem Soc. 128:1755-1761 (2006).
53. B.S. Kim, J.M. Qiu, J.P. Wang, and T.A. Taton. Magnetomicelles: Composite nanostructures from magnetic nanoparticles and cross-linked amphiphilic block copolymers. Nano Lett. 5:1987-1991 (2005).
54. S. Kim, Y.Z. Shi, J.Y. Kim, K. Park, and J.X. Cheng. Overcoming the barriers in micellar drug delivery: loading efficiency, in vivo stability, and micelle-cell interaction. Expert Opin Drug Del. 7:49-62 (2010).
55. H.J. Leeand Y. Bae. Cross-linked nanoassemblies from poly(ethylene glycol)-poly(aspartate) block copolymers as stable supramolecular templates for particulate drug delivery. Biomacromolecules. 12:2686-2696 (2011).
56. D. Scott, J. Rohr, and Y. Bae. Nanoparticulate formulations of mithramycin analogs for enhanced cytotoxicity. Int J Nanomed. 6:2757-2767 (2011).

57. A. Ponta, S. Akter, and Y. Bae. Degradable cross-linked nanoassemblies as drug carriers for heat shock protein 90 inhibitor 17-N-allylamino-17-demethoxygeldanamycin. Pharmaceuticals. 4:1281-1292 (2011).
58. E.A. Kiyatkin and H.S. Sharma. Permeability of the blood-brain barrier depends on brain temperature. Neuroscience. 161:926-939 (2009).
59. W. Gong, Z. Wang, N. Liu, W. Lin, X. Wang, D. Xu, H. Liu, C. Zeng, X. Xie, X. Mei, and W. Lu. Improving efficiency of adriamycin crossing blood brain barrier by combination of thermosensitive liposomes and hyperthermia. Biol Pharm Bull. 34:1058-1064 (2011).
60. H.S. Sharma and P.J. Hoopes. Hyperthermia induced pathophysiology of the central nervous system. Int J Hyperthermia. 19:325-354 (2003).
61. B.B. Youan. Impact of nanoscience and nanotechnology on controlled drug delivery. Nanomedicine (Lond). 3:401-406 (2008).
62. V. Wagner, A. Dullaart, A.K. Bock, and A. Zweck. The emerging nanomedicine landscape. Nat Biotechnol. 24:1211-1217 (2006).
63. S. Aggarwal. What's fueling the biotech engine-2008. Nature Biotechnology. 27:987-993 (2009).
64. W.I. Choi, A. Sahu, Y.H. Kim, and G. Tae. Photothermal cancer therapy and imaging based on gold nanorods. Ann Biomed Eng. 40:534-546 (2012).
65. B. Perks. The catalytic potential of gold nanoparticles was overlooked for years, but researchers are making up for lost time, *Chemistry World*, 2010, pp. 48-50.
66. F. Michael. Experimental relations of gold (and other metals) to light. Phil Trans Roy Soc London. 147:145 -181 (1857).
67. S. Lal, S.E. Clare, and N.J. Halas. Nanoshell-enabled photothermal cancer therapy: impending clinical impact. Acc Chem Res. 41:1842-1851 (2008).
68. A.M. Gobin, M.H. Lee, N.J. Halas, W.D. James, R.A. Drezek, and J.L. West. Near-infrared resonant nanoshells for combined optical imaging and photothermal cancer therapy. Nano Lett. 7:1929-1934 (2007).
69. K.V. Katti, R. Kannan, K. Katti, V. Kattumori, R. Pandrapraganda, V. Rahing, C. Cutler, E.J. Boote, S.W. Casteel, C.J. Smith, J.D. Robertson, and S.S. Jurrison. Hybrid Gold Nanoparticles in Molecular Imaging and Radiotherapy. Czech J Phys. 56:D23-D34 (2006).
70. R. Xu, J. Ma, X. Sun, Z. Chen, X. Jiang, Z. Guo, L. Huang, Y. Li, M. Wang, C. Wang, J. Liu, X. Fan, J. Gu, X. Chen, Y. Zhang, and N. Gu. Ag nanoparticles sensitize IR-induced killing of cancer cells. Cell Res. 19:1031-1034 (2009).
71. L.K. Limbach, Y. Li, R.N. Grass, T.J. Brunner, M.A. Hintermann, M. Muller, D. Gunther, and W.J. Stark. Oxide nanoparticle uptake in human lung fibroblasts: effects of particle size, agglomeration, and diffusion at low concentrations. Environmental Science and Technology. 39:9370-9376 (2005).
72. S. Linkand M.A. El-Sayed. Spectral properties and relaxation dynamics of surface plasmon electronic oscillations in gold and silver nanodots and nanorods. J Phys Chem B. 103:8410-8426 (1999).
73. H.C. Huang, S. Barua, G. Sharma, S.K. Dey, and K. Rege. Inorganic nanoparticles for cancer imaging and therapy. J Control Release. 155:344-357 (2011).

74. J. You, G. Zhang, and C. Li. Exceptionally high payload of doxorubicin in hollow gold nanospheres for near-infrared light-triggered drug release. ACS Nano. 4:1033-1041 (2010).
75. J.H. Park, G. von Maltzahn, L.L. Ong, A. Centrone, T.A. Hatton, E. Ruoslahti, S.N. Bhatia, and M.J. Sailor. Cooperative nanoparticles for tumor detection and photothermally triggered drug delivery. Adv Mater. 22:880-885 (2010).
76. R.K. Visaria, R.J. Griffin, B.W. Williams, E.S. Ebbini, G.F. Paciotti, C.W. Song, and J.C. Bischof. Enhancement of tumor thermal therapy using gold nanoparticle-assisted tumor necrosis factor-alpha delivery. Mol Cancer Ther. 5:1014-1020 (2006).
77. M. Mikhaylova, Y.S. Jo, D.K. Kim, N. Bobrysheva, Y. Andersson, T. Eriksson, M. Osmolowsky, V. Semenov, and M. Muhammed. The effect of biocompatible coating layers on magnetic properties of superparamagnetic iron oxide nanoparticles. Hyperfine Interact. 156:257-263 (2004).
78. A.E. Nel, L. Madler, D. Velegol, T. Xia, E.M.V. Hoek, P. Somasundaran, F. Klaessig, V. Castranova, and M. Thompson. Understanding biophysicochemical interactions at the nano-bio interface. Nat Mater. 8:543-557 (2009).
79. A. Elder, S. Vidyasagar, and L. DeLouise. Physicochemical factors that affect metal and metal oxide nanoparticle passage across epithelial barriers. Wiley Interdiscip Rev Nanomed Nanobiotechnol. 1:434-450 (2009).
80. NIOSH. Strategic Plan for NIOSH Nanotechnology Research and Guidance, 2009.
81. P. Decuzzi, R. Pasqualini, W. Arap, and M. Ferrari. Intravascular Delivery of Particulate Systems: Does Geometry Really Matter? Pharm Res-Dord. 26:235-243 (2009).
82. S.M. Moghimi, A.C. Hunter, and J.C. Murray. Long-circulating and target-specific nanoparticles: Theory to practice. Pharmacol Rev. 53:283-318 (2001).
83. P. Decuzzi, S. Lee, B. Bhushan, and M. Ferrari. A theoretical model for the margination of particles within blood vessels. Annals of Biomedical Engineering. 33:179-190 (2005).
84. P. Decuzzi, B. Godin, T. Tanaka, S.Y. Lee, C. Chiappini, X. Liu, and M. Ferrari. Size and shape effects in the biodistribution of intravascularly injected particles. Journal of Controlled Release. 141:320-327 (2010).
85. M. Lundqvist, J. Stigler, G. Elia, I. Lynch, T. Cedervall, and K.A. Dawson. Nanoparticle size and surface properties determine the protein corona with possible implications for biological impacts. P Natl Acad Sci USA. 105:14265-14270 (2008).
86. M.P. Monopoli, D. Walczyk, A. Campbell, G. Elia, I. Lynch, F.B. Bombelli, and K.A. Dawson. Physical-Chemical Aspects of Protein Corona: Relevance to in Vitro and in Vivo Biological Impacts of Nanoparticles. Journal of the American Chemical Society. 133:2525-2534 (2011).
87. P.P. Karmali and D. Simberg. Interactions of nanoparticles with plasma proteins: implication on clearance and toxicity of drug delivery systems. Expert Opin Drug Del. 8:343-357 (2011).
88. I. Hamad, O. Al-Hanbali, A.C. Hunter, K.J. Rutt, T.L. Andresen, and S.M. Moghimi. Distinct Polymer Architecture Mediates Switching of Complement

Activation Pathways at the Nanosphere-Serum Interface: Implications for Stealth Nanoparticle Engineering. ACS Nano. 4:6629-6638 (2010).
89. V.P. Torchilin. Passive and active drug targeting: drug delivery to tumors as an example. Handb Exp Pharmacol:3-53 (2010).
90. F. Braet, R. Dezanger, M. Baekeland, E. Crabbe, P. Vandersmissen, and E. Wisse. Structure and Dynamics of the Fenestrae-Associated Cytoskeleton of Rat-Liver Sinusoidal Endothelial-Cells. Hepatology. 21:180-189 (1995).
91. S.M. Moghimi, C.J. Porter, I.S. Muir, L. Illum, and S.S. Davis. Non-phagocytic uptake of intravenously injected microspheres in rat spleen: influence of particle size and hydrophilic coating. Biochem Biophys Res Commun. 177:861-866 (1991).
92. S.M. Moghimi, A.C. Hunter, and J.C. Murray. Nanomedicine: current status and future prospects. Faseb Journal. 19:311-330 (2005).
93. S.K. Hobbs, W.L. Monsky, F. Yuan, W.G. Roberts, L. Griffith, V.P. Torchilin, and R.K. Jain. Regulation of transport pathways in tumor vessels: Role of tumor type and microenvironment. P Natl Acad Sci USA. 95:4607-4612 (1998).
94. D.C. Drummond, O. Meyer, K. Hong, D.B. Kirpotin, and D. Papahadjopoulos. Optimizing liposomes for delivery of chemotherapeutic agents to solid tumors. Pharmacol Rev. 51:691-743 (1999).
95. T. Lammers, V. Subr, K. Ulbrich, P. Peschke, P.E. Huber, W.E. Hennink, and G. Storm. Simultaneous delivery of doxorubicin and gemcitabine to tumors in vivo using prototypic polymeric drug carriers. Biomaterials. 30:3466-3475 (2009).
96. R. Weissleder, J.F. Heautot, B.K. Schaffer, N. Nossiff, M.I. Papisov, A. Bogdanov, Jr., and T.J. Brady. MR lymphography: study of a high-efficiency lymphotrophic agent. Radiology. 191:225-230 (1994).
97. S.M. Moghimi and B. Bonnemain. Subcutaneous and intravenous delivery of diagnostic agents to the lymphatic system: applications in lymphoscintigraphy and indirect lymphography. Adv Drug Deliv Rev. 37:295-312 (1999).
98. H.S. Choi, W. Liu, P. Misra, E. Tanaka, J.P. Zimmer, B. Itty Ipe, M.G. Bawendi, and J.V. Frangioni. Renal clearance of quantum dots. Nat Biotechnol. 25:1165-1170 (2007).
99. T.M. Riddick. Control of colloidal stability through zeta potential. Vol. 1, Livingston Publishing Co., Wynnewood, PA, 1968, pp. 320-331.
100. U. Gaur, S.K. Sahoo, T.K. De, P.C. Ghosh, A. Maitra, and P.K. Ghosh. Biodistribution of fluoresceinated dextran using novel nanoparticles evading reticuloendothelial system. Int J Pharm. 202:1-10 (2000).
101. T. Niidome, M. Yamagata, Y. Okamoto, Y. Akiyama, H. Takahashi, T. Kawano, Y. Katayama, and Y. Niidome. PEG-modified gold nanorods with a stealth character for in vivo applications. Journal of Controlled Release. 114:343-347 (2006).
102. T. Cao, T. Yang, Y. Gao, Y. Yang, H. Hu, and F. Li. Water-soluble NaYF4:Yb/Er upconversion nanophosphors: Synthesis, characteristics and application in bioimaging. Inorganic Chemistry Communications. 13:392-394 (2010).
103. G. Frasca, F. Gazeau, and C. Wilhelm. Formation of a three-dimensional multicellular assembly using magnetic patterning. Langmuir. 25:2348-2354 (2009).

104. B. Chanteau, J. Fresnais, and J.F. Berret. Electrosteric enhanced stability of functional sub-10 nm cerium and iron oxide particles in cell culture medium. Langmuir. 25:9064-9070 (2009).
105. G. Goloverda, B. Jackson, C. Kidd, and V. Kolesnichenko. Synthesis of ultrasmall magnetic iron oxide nanoparticles and study of their colloid and surface chemistry. J Magn Magn Mater. 321:1372-1376 (2009).
106. Y. Park, R.D. Whitaker, R.J. Nap, J.L. Paulsen, V. Mathiyazhagan, L.H. Doerrer, Y.Q. Song, M.D. Hurlimann, I. Szleifer, and J.Y. Wong. Stability of Superparamagnetic Iron Oxide Nanoparticles at Different pH Values: Experimental and Theoretical Analysis. Langmuir. 28:6246-6255 (2012).
107. M. Hatakeyama, H. Kishi, Y. Kita, K. Imai, K. Nishio, S. Karasawa, Y. Masaike, S. Sakamoto, A. Sandhu, A. Tanimoto, T. Gomi, E. Kohda, M. Abe, and H. Handa. A two-step ligand exchange reaction generates highly water-dispersed magnetic nanoparticles for biomedical applications. J Mater Chem. 21:5959-5966 (2011).
108. A.H. Lu, E.L. Salabas, and F. Schuth. Magnetic nanoparticles: synthesis, protection, functionalization, and application. Angew Chem Int Ed. 46:1222-1244 (2007).
109. H. Wolburg and A. Lippoldt. Tight junctions of the blood-brain barrier: development, composition and regulation. Vascular Pharmacology. 38:323-337 (2002).
110. I.A. Simpson, A. Carruthers, and S.J. Vannucci. Supply and demand in cerebral energy metabolism: the role of nutrient transporters. Journal of Cerebral Blood Flow and Metabolism. 27:1766-1791 (2007).
111. U. Bickel, T. Yoshikawa, and W.M. Pardridge. Delivery of peptides and proteins through the blood-brain barrier. Adv Drug Deliver Rev. 46:247-279 (2001).
112. R.A. Yokel. Blood-brain barrier flux of aluminum, manganese, iron and other metals suspected to contribute to metal-induced neurodegeneration. Journal of Alzheimer's Disease. 10:223-253 (2006).
113. S. Rapoport. Sites and functions of the blood-brain barrier., In Blood-brain barrier in physiology and medicine, Raven Press, New York, 1976, pp. 43-84.
114. W. Pardridge. Introduction to the Blood-Brain Barrier: Methodology, Biology and Pathology, Cambridge University Press, 1998.
115. B.V. Zlokovic. The Blood-Brain Barrier in Health and Chronic Neurodegenerative Disorders. Neuron. 57:178-201 (2008).
116. D.M. Hermann and C.L. Bassetti. Implications of ATP-binding cassette transporters for brain pharmacotherapies. Trends in Pharmacological Sciences. 28:128-134 (2007).
117. R. Gabathuler. Approaches to transport therapeutic drugs across the blood-brain barrier to treat brain diseases. Neurobiology of Disease. 37:48-57 (2010).
118. W. Pardridge. Drug Targeting to the Brain. Pharm Res-Dord. 24:1733-1744 (2007).
119. W.A. Vandergrift, S.J. Patel, J.S. Nicholas, and A.K. Varma. Convection-enhanced delivery of immunotoxins and radioisotopes for treatment of malignant gliomas. Neurosurg Focus. 20:E13 (2006).

120. L.K. Fung, M.G. Ewend, A. Sills, E.P. Sipos, R. Thompson, M. Watts, O.M. Colvin, H. Brem, and W.M. Saltzman. Pharmacokinetics of interstitial delivery of carmustine, 4-hydroperoxycyclophosphamide, and paclitaxel from a biodegradable polymer implant in the monkey brain. Cancer Res. 58:672-684 (1998).
121. D. Fortin, C. Gendron, M. Boudrias, and M.P. Garant. Enhanced chemotherapy delivery by intraarterial infusion and blood-brain barrier disruption in the treatment of cerebral metastasis. Cancer. 109:751-760 (2007).
122. C.A. Lipinski, F. Lombardo, B.W. Dominy, and P.J. Feeney. Experimental and computational approaches to estimate solubility and permeability in drug discovery and development settings. Adv Drug Deliver Rev. 64:4-17 (2012).
123. C.A. Lipinski, F. Lombardo, B.W. Dominy, and P.J. Feeney. Experimental and computational approaches to estimate solubility and permeability in drug discovery and development settings. Adv Drug Deliver Rev. 46:3-26 (2001).
124. M.O. Bradley, N.L. Webb, F.H. Anthony, P. Devanesan, P.A. Witman, S. Hemamalini, M.C. Chander, S.D. Baker, L. He, S.B. Horwitz, and C.S. Swindell. Tumor targeting by covalent conjugation of a natural fatty acid to paclitaxel. Clin Cancer Res. 7:3229-3238 (2001).
125. W.M. Pardridge. Transport of Small Molecules through the Blood-Brain-Barrier - Biology and Methodology. Adv Drug Deliver Rev. 15:5-36 (1995).
126. A.R. Jonesand E.V. Shusta. Blood-brain barrier transport of therapeutics via receptor-mediation. Pharm Res-Dord. 24:1759-1771 (2007).
127. P. Zhang, L. Hu, Q. Yin, Z. Zhang, L. Feng, and Y. Li. Transferrin-conjugated polyphosphoester hybrid micelle loading paclitaxel for brain-targeting delivery: synthesis, preparation and in vivo evaluation. J Control Release. 159:429-434 (2012).
128. S.U. Shin, P. Friden, M. Moran, T. Olson, Y.S. Kang, W.M. Pardridge, and S.L. Morrison. Transferrin-antibody fusion proteins are effective in brain targeting. Proc Natl Acad Sci U S A. 92:2820-2824 (1995).
129. J. Kreuter. Influence of the surface properties on nanoparticle-mediated transport of drugs to the brain. J Nanosci Nanotechno. 4:484-488 (2004).
130. C. Peetlaand V. Labhasetwar. Biophysical characterization of nanoparticle-endothelial model cell membrane interactions. Molecular Pharmaceutics. 5:418-429 (2008).
131. R.S. Dhanikula, T. Hammady, and P. Hildgen. On the Mechanism and Dynamics of Uptake and Permeation of Polyether-Copolyester Dendrimers Across an In Vitro Blood-Brain Barrier Model. J Pharm Sci-Us. 98:3748-3760 (2009).
132. J. Chang, Y. Jallouli, M. Kroubi, X.-b. Yuan, W. Feng, C.-s. Kang, P.-y. Pu, and D. Betbeder. Characterization of endocytosis of transferrin-coated PLGA nanoparticles by the blood-brain barrier. Int J Pharmaceut. 379:285-292 (2009).
133. C.C. Visser, S. Stevanovic, L.H. Voorwinden, P.J. Gaillard, D.J.A. Crommelin, M. Danhof, and A.G. de Boer. Validation of the transferrin receptor for drug targeting to brain capillary endothelial cells in vitro. Journal of Drug Targeting. 12:145-150 (2004).
134. J. Kreuter, P. Ramge, V. Petrov, S. Hamm, S.E. Gelperina, B. Engelhardt, R. Alyautdin, H. von Briesen, and D.J. Begley. Direct evidence that polysorbate-80-

coated poly(butylcyanoacrylate) nanoparticles deliver drugs to the CNS via specific mechanisms requiring prior binding of drug to the nanoparticles. Pharm Res-Dord. 20:409-416 (2003).
135. J.M. Koziara, P.R. Lockman, D.D. Allen, and R.J. Mumper. Paclitaxel nanoparticles for the potential treatment of brain tumors. Journal of Controlled Release. 99:259-269 (2004).
136. I. Tamai, Y. Sai, H. Kobayashi, M. Kamata, T. Wakamiya, and A. Tsuji. Structure-internalization relationship for adsorptive-mediated endocytosis of basic peptides at the blood-brain barrier. J Pharmacol Exp Ther. 280:410-415 (1997).
137. N.J. Abbott, L. Ronnback, and E. Hansson. Astrocyte-endothelial interactions at the blood-brain barrier. Nat Rev Neurosci. 7:41-53 (2006).
138. U. Knieseland H. Wolburg. Tight junctions of the blood-brain barrier. Cellular and Molecular Neurobiology 20:57-76 (2000).
139. F. Herve, N. Ghinea, and J.M. Scherrmann. CNS delivery via adsorptive transcytosis. AAPS J. 10:455-472 (2008).
140. H.L. Wong, X.Y. Wu, and R. Bendayan. Nanotechnological advances for the delivery of CNS therapeutics. Adv Drug Deliv Rev. 64:686-700 (2012).
141. L.A. Bareford and P.W. Swaan. Endocytic mechanisms for targeted drug delivery. Adv Drug Deliver Rev. 59:748-758 (2007).
142. S.D. Conner and S.L. Schmid. Regulated portals of entry into the cell. Nature. 422:37-44 (2003).
143. H. Hillaireau and P. Couvreur. Nanocarriers' entry into the cell: relevance to drug delivery. Cellular and Molecular Life Sciences. 66:2873-2896 (2009).
144. G. Sahay, D.Y. Alakhova, and A.V. Kabanov. Endocytosis of nanomedicines. Journal of Controlled Release. 145:182-195 (2010).
145. J. Rejman, V. Oberle, I.S. Zuhorn, and D. Hoekstra. Size-dependent internalization of particles via the pathways of clathrin-and caveolae-mediated endocytosis. Biochemical Journal. 377:159-169 (2004).
146. G. Tosi, A.V. Vergoni, B. Ruozi, L. Bondioli, L. Badiali, F. Rivasi, L. Costantino, F. Forni, and M.A. Vandelli. Sialic acid and glycopeptides conjugated PLGA nanoparticles for central nervous system targeting: In vivo pharmacological evidence and biodistribution. Journal of Controlled Release. 145:49-57 (2010).
147. Y. Liu, J.F. Li, K. Shao, R.Q. Huang, L.Y. Ye, J.N. Lou, and C. Jiang. A leptin derived 30-amino-acid peptide modified pegylated poly-L-lysine dendrigraft for brain targeted gene delivery. Biomaterials. 31:5246-5257 (2010).
148. O. Veiseh, C. Sun, C. Fang, N. Bhattarai, J. Gunn, F. Kievit, K. Du, B. Pullar, D. Lee, R.G. Ellenbogen, J. Olson, and M.Q. Zhang. Specific targeting of brain tumors with an optical/magnetic resonance imaging nanoprobe across the blood-brain barrier. Cancer Res. 69:6200-6207 (2009).
149. J. Jiang, G. Oberdorster, A. Elder, R. Gelein, P. Mercer, and P. Biswas. Does nanoparticle activity depend upon size and crystal phase? Nanotoxicology. 2:33-42 (2008).
150. B.D. Chithrani, A.A. Ghazani, and W.C.W. Chan. Determining the size and shape dependence of gold nanoparticle uptake into mammalian cells. Nano Letters. 6:662-668 (2006).

151. B.D. Chithrani and W.C.W. Chan. Elucidating the mechanism of cellular uptake and removal of protein-coated gold nanoparticles of different sizes and shapes. Nano Letters. 7:1542-1550 (2007).
152. L.K. Limbach, Y.C. Li, R.N. Grass, T.J. Brunner, M.A. Hintermann, M. Muller, D. Gunther, and W.J. Stark. Oxide nanoparticle uptake in human lung fibroblasts: Effects of particle size, agglomeration, and diffusion at low concentrations. Environ Sci Technol. 39:9370-9376 (2005).
153. J.O. Ferin, G. ; Penney, D. P. ; Soderholm, S. C. ; Gelein, R. ; Piper, H. C. Increased pulmonary toxicity of ultrafine particles? I, Particle clearance, translocation, morphology. Journal of aerosol science 21:381-384 (1990).
154. G. Oberdörster, A. Elder, and A. Rinderknecht. Nanoparticles and the brain: cause for concern? J Nanosci Nanotechno. 9:4996-5007 (2009).
155. M.D. Howard, M. Jay, T.D. Dziubla, and X.L. Lu. PEGylation of nanocarrier drug delivery systems: State of the art. Journal of Biomedical Nanotechnology. 4:133-148 (2008).
156. S. Ku, F. Yan, Y. Wang, Y. Sun, N. Yang, and L. Ye. The blood-brain barrier penetration and distribution of PEGylated fluorescein-doped magnetic silica nanoparticles in rat brain. Biochemical and Biophysical Research Communications. In Press, Uncorrected Proof.
157. P. Calvo, B. Gouritin, H. Chacun, D. Desmaële, J. D'Angelo, J.-P. Noel, D. Georgin, E. Fattal, J.P. Andreux, and P. Couvreur. Long-Circulating PEGylated Polycyanoacrylate Nanoparticles as New Drug Carrier for Brain Delivery. Pharm Res-Dord. 18:1157-1166 (2001).
158. Z.H. Wang, Z.Y. Wang, C.S. Sun, C.Y. Wang, T.Y. Jiang, and S.L. Wang. Trimethylated chitosan-conjugated PLGA nanoparticles for the delivery of drugs to the brain. Biomaterials. 31:908-915 (2010).
159. T. Cedervall, I. Lynch, S. Lindman, T. Berggard, E. Thulin, H. Nilsson, K.A. Dawson, and S. Linse. Understanding the nanoparticle-protein corona using methods to quantify exchange rates and affinities of proteins for nanoparticles. P Natl Acad Sci USA. 104:2050-2055 (2007).
160. A. Crowe and E.H. Morgan. Iron and transferrin uptake by brain and cerebrospinal fluid in the rat. Brain Res. 592:8-16 (1992).
161. E.H. Morgan and T. Moos. Mechanism and developmental changes in iron transport across the blood-brain barrier. Dev Neurosci. 24:106-113 (2002).
162. A. Zensi, D. Begley, C. Pontikis, C. Legros, L. Mihoreanu, S. Wagner, C. Buchel, H. von Briesen, and J. Kreuter. Albumin nanoparticles targeted with Apo E enter the CNS by transcytosis and are delivered to neurones. Journal of Controlled Release. 137:78-86 (2009).
163. D.E. Owens and N.A. Peppas. Opsonization, biodistribution, and pharmacokinetics of polymeric nanoparticles. Int J Pharmaceut. 307:93-102 (2006).
164. M. Demeule, J.C. Currie, Y. Bertrand, C. Che, T. Nguyen, A. Regina, R. Gabathuler, J.P. Castaigne, and R. Beliveau. Involvement of the low-density lipoprotein receptor-related protein in the transcytosis of the brain delivery vector Angiopep-2. Journal of Neurochemistry. 106:1534-1544 (2008).

165. M. Demeule, A. Regina, C. Che, J. Poirier, T. Nguyen, R. Gabathuler, J.P. Castaigne, and R. Beliveau. Identification and design of peptides as a new drug delivery system for the brain. J Pharmacol Exp Ther. 324:1064-1072 (2008).
166. W. Ke, K. Shao, R. Huang, L. Han, Y. Liu, J. Li, Y. Kuang, L. Ye, J. Lou, and C. Jiang. Gene delivery targeted to the brain using an Angiopep-conjugated polyethyleneglycol-modified polyamidoamine dendrimer. Biomaterials. 30:6976-6985 (2009).
167. S. Linse, C. Cabaleiro-Lago, W.F. Xue, I. Lynch, S. Lindman, E. Thulin, S.E. Radford, and K.A. Dawson. Nucleation of protein fibrillation by nanoparticles. P Natl Acad Sci USA. 104:8691-8696 (2007).
168. I. Integrated Laboratory Systems. Chemical information profile for ceric oxide [CAS No. 1306-38-3]. Supporting Nomination for Toxicological Evaluation by the National Toxicology Program. In N. National Toxicology Program, Research Triangle Park, NC (ed.), Research Triangle Park, NC., 2006, p. 21.
169. V.T. Davisand J.S. Thompson. Measurement of the electron affinity of cerium. Phys Rev Lett. 88:073003 (2002).
170. F. Esch, S. Fabris, L. Zhou, T. Montini, C. Africh, P. Fornasiero, G. Comelli, and R. Rosei. Electron localization determines defect formation on ceria substrates. Science. 309:752-755 (2005).
171. M. Fronzi, A. Soon, B. Delley, E. Traversa, and C. Stampfl. Stability and morphology of cerium oxide surfaces in an oxidizing environment: A first-principles investigation. Journal of Chemical Physics. 131: (2009).
172. J.E. Spanier, R.D. Robinson, F. Zheng, S.W. Chan, and I.P. Herman. Size-dependent properties of CeO2-y nanoparticles as studied by Raman scattering. Phys Rev B. 64: (2001).
173. A. Karakoti, S. Singh, J.M. Dowding, S. Seal, and W.T. Self. Redox-active radical scavenging nanomaterials. Chemical Society Reviews. 39:4422-4432 (2010).
174. M. Das, S. Patil, N. Bhargava, J.-F. Kang, L.M. Riedel, S. Seal, and J.J. Hickman. Auto-catalytic ceria nanoparticles offer neuroprotection to adult rat spinal cord neurons. Biomaterials. 28:1918-1925 (2007).
175. A. Corma, P. Atienzar, H. Garcia, and J.Y. Chane-Ching. Hierarchically mesostructured doped CeO2 with potential for solar-cell use. Nat Mater. 3:394-397 (2004).
176. E.G. Heckert, S. Seal, and W.T. Self. Fenton-like reaction catalyzed by the rare earth inner transition metal cerium. Environ Sci Technol. 42:5014-5019 (2008).
177. X. He, H. Zhang, Y. Ma, W. Bai, Z. Zhang, K. Lu, Y. Ding, Y. Zhao, and Z. Chai. Lung deposition and extrapulmonary translocation of nano-ceria after intratracheal instillation Nanotechnology. 21:285103/285101-285103/285108 (2010).
178. S.M. Hirst, A. Karakoti, S. Singh, W. Self, R. Tyler, S. Seal, and C.M. Reilly. Bio-distribution and *in vivo* antioxidant effects of cerium oxide nanoparticles in mice. Environ Toxicol:1-12 (2011).
179. R.A. Yokel, M.T. Tseng, M. Dan, J.M. Unrine, U.M. Graham, P. Wu, and E.A. Grulke. Biodistribution, biopersistence and associated toxicity of ceria engineered nanomaterial Nanomedicine: Nanotechnology, Biology and Medicine (Submitted).

180. Z.J. Deng, G. Mortimer, T. Schiller, A. Musumeci, D. Martin, and R.F. Minchin. Differential plasma protein binding to metal oxide nanoparticles. Nanotechnology. 20: (2009).
181. P.R. Salacinski, C. McLean, J.E. Sykes, V.V. Clement-Jones, and P.J. Lowry. Iodination of proteins, glycoproteins, and peptides using a solid-phase oxidizing agent, 1, 3, 4, 6-tetrachloro-3α, 6α-diphenyl glycoluril (Iodogen). Analytical biochemistry. 117:136-146 (1981).
182. J. Wang, M.F. Rahman, H.M. Duhart, G.D. Newport, T.A. Patterson, R.C. Murdock, S.M. Hussain, J.J. Schlager, and S.F. Ali. Expression changes of dopaminergic system-related genes in PC12 cells induced by manganese, silver, or copper nanoparticles. Neurotoxicology. 30:926-933 (2009).
183. D. Walczyk, F.B. Bombelli, M.P. Monopoli, I. Lynch, and K.A. Dawson. What the Cell "Sees" in Bionanoscience. Journal of the American Chemical Society. 132:5761-5768 (2010).
184. N. Mandzy, E. Grulke, and T. Druffel. Breakage of TiO2 agglomerates in electrostatically stabilized aqueous dispersions. Powder Technology. 160:121-126 (2005).
185. N.S. Satarkar, D. Biswal, and J.Z. Hilt. Hydrogel nanocomposites: a review of applications as remote controlled biomaterials. Soft Matter. 6:2364-2371 (2010).
186. R.A. Frimpongand J.Z. Hilt. Magnetic nanoparticles in biomedicine: synthesis, functionalization and applications. Nanomedicine (Lond). 5:1401-1414 (2010).
187. D.L. Thorek, A.K. Chen, J. Czupryna, and A. Tsourkas. Superparamagnetic iron oxide nanoparticle probes for molecular imaging. Ann Biomed Eng. 34:23-38 (2006).
188. L. Geraets, A.G. Oomen, J.D. Schroeter, V.A. Coleman, and F.R. Cassee. Tissue distribution of inhaled micro- and nano-sized cerium oxide particles in rats: results from a 28-day exposure study. Toxicol Sci. 127:463-473 (2012).
189. R.A. Yokel, M.T. Tseng, M. Dan, J.M. Unrine, U.M. Graham, P. Wu, and E.A. Grulke. Biodistribution and biopersistence of ceria engineered nanomaterials: size dependence. Nanomedicine. 9:398-407 (2013).
190. R. Cavaliere, E.C. Ciocatto, B.C. Giovanella, C. Heidelberger, R.O. Johnson, M. Margottini, B. Mondovi, G. Moricca, and A. Rossi-Fanelli. Selective heat sensitivity of cancer cells. Biochemical and clinical studies. Cancer. 20:1351-1381 (1967).
191. K.M. Krishnan. Biomedical nanomagnetics: a spin through possibilities in imaging, diagnostics, and therapy. IEEE T Magn. 46:2523-2558 (2010).
192. A.C. Silva, T.R. Oliveira, J.B. Mamani, S.M.F. Malheiros, L. Malavolta, L.F. Pavon, T.T. Sibov, E. Amaro, A. Tannus, E.L.G. Vidoto, M.J. Martins, R.S. Santos, and L.F. Gamarra. Application of hyperthermia induced by superparamagnetic iron oxide nanoparticles in glioma treatment. International Journal of Nanomedicine. 6:591-603 (2011).
193. Z.R. Stephen, F.M. Kievit, and M. Zhang. Magnetite nanoparticles for medical MR imaging. Mater Today. 14:330-338 (2011).
194. M. Semmler-Behnke, W.G. Kreyling, J. Lipka, S. Fertsch, A. Wenk, S. Takenaka, G. Schmid, and W. Brandau. Biodistribution of 1.4- and 18-nm gold particles in rats. Small. 4:2108-2111 (2008).

195. H.J. Weinmann, R.C. Brasch, W.R. Press, and G.E. Wesbey. Characteristics of gadolinium-DTPA complex: a potential NMR contrast agent. AJR Am J Roentgenol. 142:619-624 (1984).
196. M. Dan, D.F. Scott, P.A. Hardy, R.J. Wydra, J.Z. Hilt, R.A. Yokel, and Y. Bae. Block copolymer cross-linked nanoassemblies improve particle stability and biocompatibility of superparamagnetic iron oxide nanoparticles. Pharm Res. 30:552-561 (2013).
197. A. Ito, M. Shinkai, H. Honda, K. Yoshikawa, S. Saga, T. Wakabayashi, J. Yoshida, and T. Kobayashi. Heat shock protein 70 expression induces antitumor immunity during intracellular hyperthermia using magnetite nanoparticles. Cancer Immunology Immunotherapy. 52:80-88 (2003).
198. A. Ito, M. Shinkai, H. Honda, and T. Kobayashi. Heat-inducible TNF-alpha gene therapy combined with hyperthermia using magnetic nanoparticles as a novel tumor-targeted therapy. Cancer Gene Therapy. 8:649-654 (2001).
199. M. Dan, M.T. Tseng, P. Wu, J.M. Unrine, E.A. Grulke, and R.A. Yokel. Brain microvascular endothelial cell association and distribution of a 5 nm ceria engineered nanomaterial. Int J Nanomedicine. 7:4023-4036 (2012).
200. R. Yokel, E. Grulke, and R. Macphail. Metal-based nanoparticle interactions with the nervous system: the challenge of brain entry and the risk of retention in the organism. Wiley Interdiscip Rev Nanomed Nanobiotechnol (2013).
201. V.M. Runge. Notes on "Characteristics of gadolinium-DTPA complex: a potential NMR contrast agent". AJR Am J Roentgenol. 190:1433-1434 (2008).
202. B. Wang, W.Y. Feng, M. Wang, J.W. Shi, F. Zhang, H. Ouyang, Y.L. Zhao, Z.F. Chai, Y.Y. Huang, Y.N. Xie, H.F. Wang, and J. Wang. Transport of intranasally instilled fine Fe2O3 particles into the brain: Micro-distribution, chemical states, and histopathological observation. Biological Trace Element Research. 118:233-243 (2007).
203. B.B. Weksler, E.A. Subileau, N. Perriere, P. Charneau, K. Holloway, M. Leveque, H. Tricoire-Leignel, A. Nicotra, S. Bourdoulous, P. Turowski, D.K. Male, F. Roux, J. Greenwood, I.A. Romero, and P.O. Couraud. Blood-brain barrier-specific properties of a human adult brain endothelial cell line. FASEB J. 19:1872-1874 (2005).
204. J. Lodhia, G. Mandarano, N. Ferris, P. Eu, and S. Cowell. Development and use of iron oxide nanoparticles (Part 1): Synthesis of iron oxide nanoparticles for MRI. Biomed Imaging Interv J. 6:e12 (2010).
205. M. Lattuada and T.A. Hatton. Functionalization of monodisperse magnetic nanoparticles. Langmuir. 23:2158-2168 (2007).
206. R. Guo, Y. Song, G.L. Wang, and R.W. Murray. Does core size matter in the kinetics of ligand exchanges of monolayer-protected Au clusters? J Am Chem Soc. 127:2752-2757 (2005).
207. G.H. Woehrle, L.O. Brown, and J.E. Hutchison. Thiol-functionalized, 1.5-nm gold nanoparticles through ligand exchange reactions: Scope and mechanism of ligand exchange. J Am Chem Soc. 127:2172-2183 (2005).
208. J. Papademetriou, C. Garnacho, D. Serrano, T. Bhowmick, E.H. Schuchman, and S. Muro. Comparative binding, endocytosis, and biodistribution of antibodies and

antibody-coated carriers for targeted delivery of lysosomal enzymes to ICAM-1 versus transferrin receptor. J Inherit Metab Dis. 36:467-477 (2013).
209. J.E. Riviere. Pharmacokinetics of nanomaterials: an overview of carbon nanotubes, fullerenes and quantum dots. Wiley Interdiscip Rev Nanomed Nanobiotechnol. 1:26-34 (2009).
210. R. Hardman. A toxicologic review of quantum dots: Toxicity depends on physicochemical and environmental factors. Environmental Health Perspectives. 114:165-172 (2006).
211. E.V. Batrakova and A.V. Kabanov. Pluronic block copolymers: evolution of drug delivery concept from inert nanocarriers to biological response modifiers. J Control Release. 130:98-106 (2008).
212. J.R. Kanwar, G. Mahidhara, and R.K. Kanwar. Recent advances in nanoneurology for drug delivery to the brain. Current Nanoscience 5:441-448 (2009).
213. T. Masui, H. Hirai, N. Imanaka, G. Adachi, T. Sakata, and H. Mori. Synthesis of cerium oxide nanoparticles by hydrothermal crystallization with citric acid. Journal of Materials Science Letters. 21:489-491 (2002).
214. C. Pan, D. Zhang, and L. Shi. CTAB assisted hydrothermal synthesis, controlled conversion and CO oxidation properties of CeO2 nanoplates, nanotubes, and nanorods. Journal of Solid State Chemistry. 181:1298-1306 (2008).
215. H.-X. Mai, L.-D. Sun, Y.-W. Zhang, R. Si, W. Feng, H.-P. Zhang, H.-C. Liu, and C.-H. Yan. Shape-selective synthesis and oxygen storage behavior of ceria nanopolyhedra, nanorods, and nanocubes. Journal of Physical Chemistry B 109:24380-24385 (2005).
216. Q. Wu, F. Zhang, P. Xiao, H. Tao, X. Wang, Z. Hu, and Y. Lu. Great influence of anions for controllable synthesis of CeO_2 nanostructures: From nanorods to nanocubes. Journal of Physical Chemistry C. 112:17076-17080 (2008).
217. F. Zhang, Q. Jin, and S.-W. Chan. Ceria nanoparticles: Size, size distribution, and shape. Journal of Applied Physics. 95:4319-4326 (2004).
218. K. Bjondahl. Differences in liver weight, mortality in cerium-treated mice and 144Ce levels in blood, liver, urine and faeces at various intervals after treatment with nafenopin and pregnenolone 16-alpha-carbonitrile (PCN). Medical Biology. 54:454-460 (1976).
219. Y.I. Moskalev. [Experiments on distribution of Ce 144]. Med Radiol (Mosk). 4:52-58 (1959).
220. K. Takada and M. Fujita. Effects of DTPA on the excretion and tissue distribution of 144Ce administered subcutaneously, intramuscularly and intravenously in rats. J Radiat Res (Tokyo). 14:187-197 (1973).
221. B.A. Rzigalinski, I. Danelison, E.T. Strawn, C.A. Cohen, and C. Liang. Nanoparticles for cell engineering - A radical concept. In C.S.S.R. Kumar (ed.), Nanotechnologies for the Life Sciences, Vol. 9 Tissue, Cell and Organ Engineering, Wiley-VCH, Hoboken, New Jersey, 2006, pp. 361-387.
222. B.A. Rzigalinski, K. Meehan, R.M. Davis, Y. Xu, W.C. Miles, and C.A. Cohen. Radical nanomedicine. Nanomedicine (Lond). 1:399-412 (2006).
223. S.M. Hirst, A.S. Karakoti, R.D. Tyler, N. Sriranganathan, S. Seal, and C.M. Reilly. Anti-inflammatory Properties of Cerium Oxide Nanoparticles. Small. 5:2848-2856 (2009).

224. S.S. Hardas, D.A. Butterfield, R. Sultana, M.T. Tseng, M. Dan, R.L. Florence, J.M. Unrine, U.M. Graham, P. Wu, E.A. Grulke, and R.A. Yokel. Brain distribution and toxicological evaluation of a systemically delivered engineered nanoscale ceria. Toxicological Sciences 116:562-576 (2010).
225. Y. Nakamura, Y. Tsumura, Y. Tonogai, T. Shibata, and Y. Ito. Differences in behavior among the chlorides of seven rare earth elements administered intravenously to rats. Fundam Appl Toxicol. 37:106-116 (1997).
226. M. Geiser, B. Rothen-Rutishauser, N. Kapp, S. Schurch, W. Kreyling, H. Schulz, M. Semmler, V. Im Hof, J. Heyder, and P. Gehr. Ultrafine particles cross cellular membranes by nonphagocytic mechanisms in lungs and in cultured cells. Environ Health Perspect. 113:1555-1560 (2005).
227. B.M. Rothen-Rutishauser, S. Schurch, B. Haenni, N. Kapp, and P. Gehr. Interaction of fine particles and nanoparticles with red blood cells visualized with advanced microscopic techniques. Environ Sci Technol. 40:4353-4359 (2006).
228. J. Wang, G. Zhou, C. Chen, H. Yu, T. Wang, Y. Ma, G. Jia, Y. Gao, B. Li, J. Sun, Y. Li, F. Jiao, Y. Zhao, and Z. Chai. Acute toxicity and biodistribution of different sized titanium dioxide particles in mice after oral administration. Toxicol Lett. 168:176-185 (2007).
229. R.S. Yang, L.W. Chang, J.P. Wu, M.H. Tsai, H.J. Wang, Y.C. Kuo, T.K. Yeh, C.S. Yang, and P. Lin. Persistent tissue kinetics and redistribution of nanoparticles, quantum dot 705, in mice: ICP-MS quantitative assessment. Environ Health Perspect. 115:1339-1343 (2007).
230. W.T. Al-Jamal, K.T. Al-Jamal, A. Cakebread, J.M. Halket, and K. Kostarelos. Blood circulation and tissue biodistribution of lipid--quantum dot (L-QD) hybrid vesicles intravenously administered in mice. Bioconjug Chem. 20:1696-1702 (2009).
231. H.C. Fischer, L. Liu, K.S. Pang, and W.C.W. Chan. Pharmacokinetics of nanoscale quantum dots: in vivo distribution, sequestration, and clearance in the rat Advanced Functional Materials. 16:1299-1305 (2006).
232. M. Li, K.T. Al-Jamal, K. Kostarelos, and J. Reineke. Physiologically based pharmacokinetic modeling of nanoparticles. ACS Nano. 4:6303-6317 (2010).
233. S.H. Brewer, W.R. Glomm, M.C. Johnson, M.K. Knag, and S. Franzen. Probing BSA binding to citrate-coated gold nanoparticles and surfaces. Langmuir. 21:9303-9307 (2005).
234. R.F. Uren and C.A. Hoefnagel. Lymphoscintigraphy. In J.F. Thompson, D.L. Morton, and B.B.R. Kroon (eds.), Textbook of melanoma, Martin Dunitz, New York, 2004, pp. 339-364.
235. S. Kim, Y.T. Lim, E.G. Soltesz, A.M. De Grand, J. Lee, A. Nakayama, J.A. Parker, T. Mihaljevic, R.G. Laurence, D.M. Dor, L.H. Cohn, M.G. Bawendi, and J.V. Frangioni. Near-infrared fluorescent type II quantum dots for sentinel lymph node mapping. Nat Biotechnol. 22:93-97 (2004).
236. M.R.T.N. Tozer. Clinical pharmacokinetics and pharmacodynamics-comcepts and applications, Wolters Kluwer, 2009.
237. J.J. DiStefano, 3rd. Noncompartmental vs. compartmental analysis: some bases for choice. Am J Physiol. 243:R1-6 (1982).

238. R.S. Yang, L.W. Chang, C.S. Yang, and P. Lin. Pharmacokinetics and physiologically-based pharmacokinetic modeling of nanoparticles. J Nanosci Nanotechnol. 10:8482-8490 (2010).
239. S.D. Liand L. Huang. Pharmacokinetics and biodistribution of nanoparticles. Mol Pharm. 5:496-504 (2008).
240. J.F. Nyland and E.K. Silbergeld. A nanobiological approach to nanotoxicology. Hum Exp Toxicol. 28:393-400 (2009).
241. H.A. Lee, T.L. Leavens, S.E. Mason, N.A. Monteiro-Riviere, and J.E. Riviere. Comparison of quantum dot biodistribution with a blood-flow-limited physiologically based pharmacokinetic model. Nano Lett. 9:794-799 (2009).
242. M. Dan, P. Wu, E.A. Grulke, U.M. Graham, J.M. Unrine, and R.A. Yokel. Ceria engineered nanomaterial distribution in and clearance from blood: Size matters. Nanomedicine. 7:95-110 (2012).
243. T. Xia, M. Kovochich, M. Liong, L. Madler, B. Gilbert, H. Shi, J.I. Yeh, J.I. Zink, and A.E. Nel. Comparison of the mechanism of toxicity of zinc oxide and cerium oxide nanoparticles based on dissolution and oxidative stress properties. ACS Nano. 2:2121-2134 (2008).
244. J. Choi, V. Reipa, V.M. Hitchins, P.L. Goering, and R.A. Malinauskas. Physicochemical characterization and in vitro hemolysis evaluation of silver nanoparticles Toxicological Sciences. 123:133-143 (2011).
245. J.L. Viota, K. Rudzk, Á. Trueba, I. Torres-Aleman, and Á.V. Delgado. Electrophoretic characterization of insulin frowth Factor (IGF-1) functionalized magnetic nanoparticles. Langmuir. 27:6426-6432 (2011).
246. R.A. Bronen and G. Sze. Magnetic-resonance-imaging contracst agents - theory and application to the central - nervous - system. Journal of Neurosurgery. 73:820-839 (1990).
247. J.S. Crossgrove, D.D. Allen, B.L. Bukaveckas, S.S. Rhineheimer, and R.A. Yokel. Manganese distribution across the blood-brain barrier. I. Evidence for carrier-mediated influx of managanese citrate as well as manganese and manganese transferrin. NeuroToxicology. 24:3-13. (2003).
248. J.S. Crossgrove and R.A. Yokel. Manganese distribution across the blood-brain barrier III. The divalent metal transporter-1 is not the major mechanism mediating brain manganese uptake. Neurotoxicology. 25:451-460 (2004).
249. J.S. Crossgrove and R.A. Yokel. Manganese distribution across the blood-brain barrier. IV. Evidence for brain influx through store-operated calcium channels. NeuroToxicology. 26:297-307 (2005).
250. Q.R. Smith. Brain perfusion systems for studies of drug uptake and metabolism in the central nervous system. Pharmaceutical Biotechnology. 8:285-307 (1996).
251. D. Triguero, J. Buciak, and W.M. Pardridge. Capillary depletion method for quantification of blood-brain barrier transport of circulating peptides and plasma proteins. Journal of Neurochemistry. 54:1882-1888 (1990).
252. Y. Takasato, S.I. Rapoport, and Q.R. Smith. An in situ brain perfusion technique to study cerebrovascular transport in the rat. American Journal of Physiology. 247:H484-H493 (1984).

253. C.C.a.D.G. Levitt. Capillary permeability to small solutes. In Handbook of Physiology. The Cardiovascular System. Microcirculation., Am. Physiol. Soc., Bethesda, MD, 1984.
254. D.E. Owens and N.A. Peppas. Opsonization, biodistribution, and pharmacokinetics of polymeric nanoparticles. Int J Pharm. 307:93-102 (2006).
255. Z.J. Deng, G. Mortimer, T. Schiller, A. Musumeci, D. Martin, and R.F. Minchin. Differential plasma protein binding to metal oxide nanoparticles. Nanotechnology. 20:455101/455101-455101/455109 (2009).
256. W.H. De Jong, W.I. Hagens, P. Krystek, M.C. Burger, A.J. Sips, and R.E. Geertsma. Particle size-dependent organ distribution of gold nanoparticles after intravenous administration. Biomaterials. 29:1912-1919 (2008).
257. L. Garza-Ocanas, D.A. Ferrer, J. Burt, L.A. Diaz-Torres, M. Ramirez Cabrera, V.T. Rodriguez, R. Lujan Rangel, D. Romanovicz, and M. Jose-Yacaman. Biodistribution and long-term fate of silver nanoparticles functionalized with bovine serum albumin in rats. Metallomics. 2:204-210 (2010).
258. J.M. Koziara, P.R. Lockman, D.D. Allen, and R.J. Mumper. In situ blood-brain barrier transport of nanoparticles. Pharm Res-Dord. 20:1772-1778 (2003).
259. M. Dan, P. Wu, E.A. Grulke, U.M. Graham, J.M. Unrine, and R.A. Yokel. Ceria-engineered nanomaterial distribution in, and clearance from, blood: size matters. Nanomedicine (Lond). 7:95-110 (2012).
260. C. Wilhelm, F. Gazeau, J. Roger, J.N. Pons, and J.C. Bacri. Interaction of anionic superparamagnetic nanoparticles with cells: Kinetic analyses of membrane adsorption and subsequent internalization. Langmuir. 18:8148-8155 (2002).
261. R.E. Serda, J. Gu, J.K. Burks, K. Ferrari, C. Ferrari, and M. Ferrari. Quantitative Mechanics of Endothelial Phagocytosis of Silicon Microparticles. Cytometry Part A. 75A:752-760 (2009).
262. S. Tanabe, Y. Shimohigashi, Y. Nakayama, T. Makino, T. Fujita, T. Nose, G. Tsujimoto, T. Yokokura, M. Naito, T. Tsuruo, and T. Terasaki. In vivo and in vitro evidence of blood-brain barrier transport of a novel cationic arginine-vasopressin fragment 4-9 analog. J Pharmacol Exp Ther. 290:561-568 (1999).
263. Y.S. Kang and W.M. Pardridge. Brain delivery of biotin bound to a conjugate of neutral avidin and cationized human albumin. Pharm Res. 11:1257-1264 (1994).
264. N. Strazielle and J.F. Ghersi-Egea. Choroid plexus in the central nervous system: biology and physiopathology. J Neuropathol Exp Neurol. 59:561-574 (2000).
265. Z. Redzic. Molecular biology of the blood-brain and the blood-cerebrospinal fluid barriers: similarities and differences. Fluids Barriers CNS. 8:3 (2011).
266. W. Zheng. Toxicology of choroid plexus: Special reference to metal-induced neurotoxicities. Microscopy Research and Technique. 52:89-103 (2001).
267. J.K. Räty, T. Liimatainen, T. Wirth, K.J. Airenne, T.O. Ihalainen, T. Huhtala, E. Hamerlynck, M. Vihinen-Ranta, A. Närvänen, S. Ylä-Herttuala, and J.M. Hakumäki. Magnetic resonance imaging of viral particle biodistribution in vivo. Gene Therapy. 13:1440-1446 (2006).
268. S. Salmaso, J.S. Pappalardo, R.R. Sawant, T. Musacchio, K. Rockwell, P. Caliceti, and V.P. Torchilin. Targeting glioma cells in vitro with ascorbate-conjugated pharmaceutical nanocarriers. Bioconjug Chem. 20:2348-2355 (2009).

269. T. Kobayashi. Cancer hyperthermia using magnetic nanoparticles. Biotechnol J. 6:1342-1347 (2011).
270. C. Rumenapp, B. Gleich, and A. Haase. Magnetic nanoparticles in magnetic resonance imaging and diagnostics. Pharm Res. 29:1165-1179 (2012).
271. R.R. Qiao, C.H. Yang, and M.Y. Gao. Superparamagnetic iron oxide nanoparticles: from preparations to in vivo MRI applications. J Mater Chem. 19:6274-6293 (2009).
272. M. Wagner, S. Wagner, J. Schnorr, E. Schellenberger, D. Kivelitz, L. Krug, M. Dewey, M. Laule, B. Hamm, and M. Taupitz. Coronary MR Angiography Using Citrate-Coated Very Small Superparamagnetic Iron Oxide Particles as Blood-Pool Contrast Agent: Initial Experience in Humans. J Magn Reson Imaging. 34:816-823 (2011).
273. B. Chanteau, J. Fresnais, and J.F. Berret. Electrosteric enhanced stability of functional sub-10 nm cerium and iron oxide particles in cell culture medium. Langmuir. 25:9064-9070 (2009).
274. S.A. Meenach, J.Z. Hilt, and K.W. Anderson. Poly(ethylene glycol)-based magnetic hydrogel nanocomposites for hyperthermia cancer therapy. Acta Biomater. 6:1039-1046 (2010).
275. R.A. Frimpong, J. Dou, M. Pechan, and J.Z. Hilt. Enhancing remote controlled heating characteristics in hydrophilic magnetite nanoparticles via facile co-precipitation. J Magn Magn Mater. 322:326-331 (2010).
276. J. O'Brien, I. Wilson, T. Orton, and F. Pognan. Investigation of the Alamar Blue (resazurin) fluorescent dye for the assessment of mammalian cell cytotoxicity. Eur J Biochem. 267:5421-5426 (2000).
277. M.L. Forrest, J.A. Yanez, C.M. Remsberg, Y. Ohgami, G.S. Kwon, and N.M. Davies. Paclitaxel prodrugs with sustained release and high solubility in poly(ethylene glycol)-b-poly(epsilon-caprolactone) micelle nanocarriers: pharmacokinetic disposition, tolerability, and cytotoxicity. Pharm Res. 25:194-206 (2008).
278. R. Tantra, J. Tompkins, and P. Quincey. Characterisation of the de-agglomeration effects of bovine serum albumin on nanoparticles in aqueous suspension. Colloid Surface B. 75:275-281 (2010).
279. Z.E. Allouni, M.R. Cimpan, P.J. Hol, T. Skodvin, and N.R. Gjerdet. Agglomeration and sedimentation of TiO2 nanoparticles in cell culture medium. Colloid Surface B. 68:83-87 (2009).
280. L. Foucaud, M.R. Wilson, D.M. Brown, and V. Stone. Measurement of reactive species production by nanoparticles prepared in biologically relevant media. Toxicol Lett. 174:1-9 (2007).
281. T. Neuberger, B. Schöpf, H. Hofmann, M. Hofmann, and B. von Rechenberg. Superparamagnetic nanoparticles for biomedical applications: Possibilities and limitations of a new drug delivery system. J Magn Magn Mater. 293:483-496 (2005).
282. L.C. Varanda, M. Jafelicci, P. Tartaj, K. O' Grady, T. Gonzalez-Carreno, M.P. Morales, T. Munoz, and C.J. Serna. Structural and magnetic transformation of monodispersed iron oxide particles in a reducing atmosphere. J Appl Phys. 92:2079-2085 (2002).

283. Z.J. Deng, G. Mortimer, T. Schiller, A. Musumeci, D. Martin, and R.F. Minchin. Differential plasma protein binding to metal oxide nanoparticles. Nanotechnology. 20:455101-455109 (2009).
284. A.J. Cole, A.E. David, J. Wang, C.J. Galbán, H.L. Hill, and V.C. Yang. Polyethylene glycol modified, cross-linked starch-coated iron oxide nanoparticles for enhanced magnetic tumor targeting. Biomaterials. 32:2183-2193 (2011).
285. M.I. Khan, A. Mohammad, G. Patil, S.A. Naqvi, L.K. Chauhan, and I. Ahmad. Induction of ROS, mitochondrial damage and autophagy in lung epithelial cancer cells by iron oxide nanoparticles. Biomaterials. 33:1477-1488 (2012).
286. C.C. Berry, S. Wells, S. Charles, and A.S. Curtis. Dextran and albumin derivatised iron oxide nanoparticles: influence on fibroblasts in vitro. Biomaterials. 24:4551-4557 (2003).
287. S.J. Soenen and M. De Cuyper. Assessing iron oxide nanoparticle toxicity in vitro: current status and future prospects. Nanomedicine. 5:1261-1275 (2010).
288. M. Yanase, M. Shinkai, H. Honda, T. Wakabayashi, J. Yoshida, and T. Kobayashi. Intracellular hyperthermia for cancer using magnetite cationic liposomes: Ex vivo study. Jpn J Cancer Res. 88:630-632 (1997).
289. A.C. Silva, T.R. Oliveira, J.B. Mamani, S.M.F. Malheiros, L. Malavolta, L.F. Pavon, T.T. Sibov, E. Amaro, A. Tannus, E.L.G. Vidoto, M.J. Martins, R.S. Santos, and L.F. Gamarra. Application of hyperthermia induced by superparamagnetic iron oxide nanoparticles in glioma treatment. Int J Nanomed. 6:591-603 (2011).
290. A. Agarwal, N. Lariya, G. Saraogi, N. Dubey, H. Agrawal, and G.P. Agrawal. Nanoparticles as Novel Carrier for Brain Delivery: A Review. Current Pharmaceutical Design. 15:917-925 (2009).
291. S. Bhaskar, F. Tian, T. Stoeger, W. Kreyling, J.M. de la Fuente, V. Grazu, P. Borm, G. Estrada, V. Ntziachristos, and D. Razansky. Multifunctional Nanocarriers for diagnostics, drug delivery and targeted treatment across blood-brain barrier: perspectives on tracking and neuroimaging. Part Fibre Toxicol. 7:3 (2010).
292. M. Dan, D.F. Scott, P.A. Hardy, R.J. Wydra, J.Z. Hilt, R.A. Yokel, and Y. Bae. Block Copolymer Cross-Linked Nanoassemblies Improve Particle Stability and Biocompatibility of Superparamagnetic Iron Oxide Nanoparticles. Pharm Res (2012).
293. B.H. Kenzaoui, C.C. Bernasconi, H. Hofmann, and L. Juillerat-Jeanneret. Evaluation of uptake and transport of ultrasmall superparamagnetic iron oxide nanoparticles by human brain-derived endothelial cells. Nanomedicine. 7:39-53 (2012).
294. Y.H. Zhou, W.R. Harris, and R.A. Yokel. The influence of citrate, maltolate and fluoride on the gastrointestinal absorption of aluminum at a drinking water-relevant concentration: A Al-26 and C-14 study. Journal of Inorganic Biochemistry. 102:798-808 (2008).
295. Y.Z. Zhouand R.A. Yokel. The chemical species of aluminum influences its paracellular flux across and uptake into Caco-2 cells, a model of gastrointestinal absorption. Toxicol Sci. 87:15-26 (2005).

296. D. Nozinic, A. Milic, L. Mikac, J. Ralic, J. Padovan, and R. Antolovic. Assessment of macrolide transport using PAMPA, Caco-2 and MDCKII-hMDR1 assays. Croat Chem Acta. 83:323-331 (2010).
297. R.C. Brown, A.P. Morris, and R.G. O'Neil. Tight junction protein expression and barrier properties of immortalized mouse brain microvessel endothelial cells. Brain Res. 1130:17-30 (2007).
298. M. Nakagawa, K. Matsumoto, H. Higashi, T. Furuta, and T. Ohmoto. Acute effects of interstitial hyperthermia on normal monkey brain--magnetic resonance imaging appearance and effects on blood-brain barrier. Neurol Med Chir (Tokyo). 34:668-675 (1994).
299. S. Krol. Challenges in drug delivery to the brain: Nature is against us. Journal of Controlled Release:145-155 (2012).
300. R.N. Germain. An innately interesting decade of research in immunology. Nature Medicine. 10:1307-1320 (2004).
301. A.E. van Herwaarden, E. Wagenaar, B. Karnekamp, G. Merino, J.W. Jonker, and A.H. Schinkel. Breast cancer resistance protein (Bcrp1/Abcg2) reduces systemic exposure of the dietary carcinogens aflatoxin B1, IQ and Trp-P-1 but also mediates their secretion into breast milk. Carcinogenesis. 27:123-130 (2006).
302. E. Hellinger, S. Veszelka, A.E. Toth, F. Walter, A. Kittel, M.L. Bakk, K. Tihanyi, V. Hada, S. Nakagawa, T.D. Duy, M. Niwa, M.A. Deli, and M. Vastag. Comparison of brain capillary endothelial cell-based and epithelial (MDCK-MDR1, Caco-2, and VB-Caco-2) cell-based surrogate blood-brain barrier penetration models. Eur J Pharm Biopharm. 82:340-351 (2012).
303. F. Fazlollahi, S. Angelow, N.R. Yacobi, R. Marchelletta, A.S. Yu, S.F. Hamm-Alvarez, Z. Borok, K.J. Kim, and E.D. Crandall. Polystyrene nanoparticle trafficking across MDCK-II. Nanomedicine. 7:588-594 (2011).
304. E. Moriyama, M. Salcman, and R.D. Broadwell. Blood-Brain-Barrier Alteration after Microwave-Induced Hyperthermia Is Purely a Thermal Effect .1. Temperature and Power Measurements. Surg Neurol. 35:177-182 (1991).
305. T. Uzuka, H. Takahashi, and R. Tanaka. Interstitial hyperthermia with intra-arterial injection of adriamycin for malignant glioma. Neurol Med-Chir. 46:19-23 (2006).
306. Q. Wang, J.D. Rager, K. Weinstein, P.S. Kardos, G.L. Dobson, J.B. Li, and I.J. Hidalgo. Evaluation of the MDR-MDCK cell line as a permeability screen for the blood-brain barrier. Int J Pharmaceut. 288:349-359 (2005).
307. N. Rapoport. Ultrasound-mediated micellar drug delivery. Int J Hyperther. 28:374-385 (2012).
308. Z. Gao, H.D. Fain, and N. Rapoport. Ultrasound-enhanced tumor targeting of polymeric micellar drug carriers. Mol Pharm. 1:317-330 (2004).
309. I. Wilhelm, C. Fazakas, and I.A. Krizbai. In vitro models of the blood-brain barrier. Acta Neurobiol Exp. 71:113-128 (2011).
310. H. Huang, S. Delikanli, H. Zeng, D.M. Ferkey, and A. Pralle. Remote control of ion channels and neurons through magnetic-field heating of nanoparticles. Nat Nanotechnol. 5:602-606 (2010).

311. R.J. Mannix, S. Kumar, F. Cassiola, M. Montoya-Zavala, E. Feinstein, M. Prentiss, and D.E. Ingber. Nanomagnetic actuation of receptor-mediated signal transduction. Nat Nanotechnol. 3:36-40 (2008).
312. H.S. Sharma, A. Sharma, H. Mossler, and D.F. Muresanu. Neuroprotective effects of cerebrolysin, a combination of different active fragments of neurotrophic factors and peptides on the whole body hyperthermia-induced neurotoxicity: modulatory roles of co-morbidity factors and nanoparticle intoxication. Int Rev Neurobiol. 102:249-276 (2012).
313. H.S. Sharma and A. Sharma. Nanowired drug delivery for neuroprotection in central nervous system injuries: modulation by environmental temperature, intoxication of nanoparticles, and comorbidity factors. Wiley Interdiscip Rev Nanomed Nanobiotechnol. 4:184-203 (2012).
314. U. Gaur, S.K. Sahoo, T.K. De, P.C. Ghosh, A. Maitra, and P.K. Ghosh. Biodistribution of fluoresceinated dextran using novel nanoparticles evading reticuloendothelial system. Int J Pharmaceut. 202:1-10 (2000).
315. J.M. Rabanel, V. Aoun, I. Elkin, M. Mokhtar, and P. Hildgen. Drug-Loaded Nanocarriers: Passive Targeting and Crossing of Biological Barriers. Curr Med Chem. 19:3070-3102 (2012).
316. M.T. Basel, S. Balivada, H. Wang, T.B. Shrestha, G.M. Seo, M. Pyle, G. Abayaweera, R. Dani, O.B. Koper, M. Tamura, V. Chikan, S.H. Bossmann, and D.L. Troyer. Cell-delivered magnetic nanoparticles caused hyperthermia-mediated increased survival in a murine pancreatic cancer model. Int J Nanomedicine. 7:297-306 (2012).
317. J. Riemer, H.H. Hoepken, H. Czerwinska, S.R. Robinson, and R. Dringen. Colorimetric ferrozine-based assay for the quantitation of iron in cultured cells. Anal Biochem. 331:370-375 (2004).

VITA

MO DAN

Birthplace: Baoji, China

EDUCATION

2008 - present	Ph.D. candidate in Pharmaceutical Sciences, College of Pharmacy, University of Kentucky, Lexington, KY
2008 - 2010	M.S. in Toxicology, Graduate Center for Toxicology, University of Kentucky, Lexington, KY
2005 - 2008	M.S. in Pharmaceutics, College of Pharmacy, Shanghai Jiao Tong University, Shanghai, China
2001 - 2005	B.S. in Pharmacy, College of Pharmacy, Sun Yat-Sen University, Guangzhou, China

PROFESSIONAL EXPERIENCES

2008 – 2013	Research Assistant – College of Pharmacy, University of Kentucky
2005 – 2008	Research Assistant – College of Pharmacy, ShangUniversity of Kentucky
2005 – 2006	Undergraduate Research – College of Pharmacy, Sun Yat-Sen University,

HONORS AND AWARDS

- **National Cancer Institute - Cancer Nanotechnology Training Center** Predoctoral Fellowship, 2011-2013.
- Medical Device Speciality Section Awards for the 52nd Annual Meeting of the Society of Toxicology, 2013.
- Peter G. Glavinos, Jr., Ph.D. Fall Graduate Student Travel Award, 2012.
- **Globalization of Pharmaceutics Education Network (GPEN) Meeting 2012 student award,** Melbourne, Australia **(GPEN-sponsored student presenter),** 2012**.**
- **Society of Toxicology student travel award** for the 51st Annual Meeting of the Society of Toxicology, 2012.

- **Student symposium award** for the 13th International Neurotoxicology Association Meeting and the 11th International Symposium on Neurobehavioral Methods and Effects in Occupational and Environmental Health (NEUREOH), Xi'an, China, 2011.
- **Karri Casner Environmental Sciences Fellowship** for the 49th Annual Meeting of the Society of Toxicology, 2010.
- **Outstanding Graduate Award,** Sun Yat-Sen University (top 5%), 2005.
- **Excellent Party Member,** Sun Yat-Sen University (Only student from the School of Pharmacy to receive the award), 2005.
- **Excellent student scholarship,** Sun Yat-Sen University (top 5%), 2001-2005.
- **Excellent League Member** of Sun Yat-Sen University, 2003-2004.
- **Excellent student leader** of Sun Yat-Sen University, 2002-2003.

PUBLICATIONS

1. Scott D, Baebout Y, Wydra R, **Dan M**, Yokel R, Hilt J, Bae Y. Block Copolymer Self-assembled and Cross-linked Nanoassemblies for Combination Delivery of Iron Oxide and Doxorubicin. Accepted.
2. **Dan M**, Scott D, Hardy P, Wydra R, Yokel R, Hilt J, Bae Y. Block copolymer cross-linked nanoassemblies improve particle stability and biocompatibility of superparamagnetic iron oxide nanoparticles. Pharmaceutical Research. 2013, 30(2): 552-61.
3. Yokel RA, Tseng MT, **Dan M**, Unrine JM, Uschi M. Graham UM, Wu P, Grulke EA. Biodistribution and biopersistence of ceria engineered nanomaterials: Size dependence. Nanomedicine: Nanotechnology, Biology, and Medicine. 2013, 9(3), 398-407.
4. **Dan M,** Tseng M, Wu P, Unrine JM, Grulke EA, Yokel RA. Brain microvascular endothelial cell association and distribution of a 5 nm ceria engineered nanomaterial. International Journal of Nanomedicine, 2012, 7, 4023-4036.
5. **Dan M**, Wu P, Grulke EA, Graham UM, Unrine JM, Yokel RA. Ceria engineered nanomaterial distribution in and clearance from blood: Size matters. Nanomedicine, 2012, 7(1), 95-110.
6. Hardas SS, Sultana R, Warrier G, **Dan M**, Florence RL, Wu P, Grulke EA, Tseng MT, Unrine JM, Graham UM, Yokel RA, Butterfield DA. Rat brain pro-oxidant effects of peripherally administered 5 nm ceria 30 days after exposure. Neurotoxicology. 2012, 28(7).
7. Yokel RA, Au TC, MacPhail R, Hardas SS, Butterfield DA, Sultana R, Goodman M, Tseng MT, **Dan M**, Haghnazar H, Unrine JM, Uschi M. Graham UM, Wu P, Grulke EA. Distribution, elimination and biopersistence to 90 days of a systemically-introduced 30 nm ceria engineered nanomaterial in rats. Toxicological Sciences, 2012, 127 (1), 256-268.
8. Hardas SS, Butterfield DA, Sultana R, Tseng MT, **Dan M**, Florence RL, Unrine JM, Graham UM, Wu P, Grulke EA, Yokel RA. Brain distribution and hippocampal oxidative stress effects of a systemically-introduced 5 nm ceria engineered nanomaterial. Toxicological Sciences, 2010, 116 (2): 562-576.
9. Chu X, Zhao T, Zhang Y, Zhao A, Zhou M, Zheng X, **Dan M**, Jia W. Determination of 13 free fatty acids in pheretima using ultra-performance LC-ESI-MS. Chromatographia, 2009, 69(7): 645-652.

10. He L, Shen P, Fu Q, Li J, **Dan M**, Wang X, Jia W. Nephro-protective effect of Kangqianling decoction on chronic renal failure rats. Journal of Ethnopharmacology, 2009, 122(2): 367-373.
11. **Dan M**, Su M, Gao X, Zhao T, Zhao A, Xie G, Qiu Y, Zhou M, Liu Z, Jia W. Metabolite profiling of Panax notoginseng using UPLC-ESI-MS. Phytochemistry, 2008, 69(11):2237-44.
12. **Dan M**, Xie G, Gao X, Long X, Su M, Zhao A, Zhao T, Zhou M, Qiu Y, Jia W. A rapid ultra performance liquid chromatography- electrospray ionization mass spectrometry method for the analysis of saponins in the adventitious roots of Panax notoginseng. Phytochemical Analysis, 2009, 20(1):68-76.
13. Gao X, **Dan M**, Zhao A, Xie G, Jia W. Simultaneous determination of nine saponins in flower buds of Panax notoginseng using high performance liquid chromatography. Biomed Chromatogr, 2008, 22(3): 244-9.
14. Zhang Y, **Dan M,** Wu J, Yang H, Huang H, Qi Y, Wei S, Okuyama T,Nakajima K. Study on the chromatographic fingerprinting of Schisandra chinensis (Turcz.) Baill. by LC coupled with principal component analysis. Chromatographia, 2008, 68(2): 101- 104.
15. Wang X, Zhao T, Gao X, **Dan M**, Zhou M, Jia W. Simultaneous determination of 17 ginsenosides in rat urine by ultraperformance liquid chromatography - mass spectrometry with solid-phase extraction. Analytica Chimica Acta, 2007, 594(2): 265-273.
16. **Dan M**, Gao XF, Xie GX, Liu Z, Zhao AH, Jia W. Application of metabolomics in the research of plant metabolites. Zhongguo Zhong Yao Za Zhi. 2007, 32(22):2337

PRESENTATIONS

3/13 **Dan, M.**, Dickerson, M.T., Hardy, P.A., Bae, Y., Yokel, R.A. Superparamagnetic iron oxide loaded cross-linked nanoassemblies improve tumor accumulation and magnetic resonance imaging *in vivo.* Presented at the 52ed Annual Meeting of the Society of Toxicology, March 11-14, San Antonio. Abstract Number/Poster Board number: 522 Poster Board -340

11/12 **Dan, M.**, Dziubla, T.D., Bae, Y., Scott, D.F., Hilt, J.Z., Yokel, R.A. Hyperthermia and anti-PECAM-1 surface modification increase Fe_3O_4 nanoparticle flux across the blood brain barrier *in vitro* and *in vivo*. Presented at Globalization of Pharmaceutics Education Network Meeting 2012, Nov 28- Dec 01, Melbourne, Australia. **Selected GPEN-sponsored presenter.**

10/12 **Dan, M.**, Cochran, D.B., Dziubla, T.D., Yokel, R.A. Study of Anti-PECAM-1 iron oxide nanoparticle flux across the blood brain barrier *in vitro* and *in vivo*. Presented at 2012 American Association of Pharmaceutical Scientist Annual Meeting and Exposition, Oct 14-18, Chicago.

09/12 **Dan, M.**, Dziubla, T.D., Bae, Y., Scott, D.F., Hilt, J.Z., Yokel, R.A. Hyperthermia and anti-PECAM-1 surface modification increase Fe3O4 nanoparticle flux across blood brain barrier cells. Presented at the 6th International Conference on Nanotoxicology, Sep 4-7, Beijing, China.

07/12 **Dan, M.**, Bae, Y., Dziubla, T.D., Scott, D.F., Hilt, J.Z., Yokel, R.A. The effect of Fe_3O_4 nanoparticle-induced hyperthermia on the blood brain-barrier association and permeability. Presented at 39th Annual Meeting & Exposition of the Controlled Release Society, July 15-18, Québec City, Québec, Canada.

05/12 **Dan, M.**, Bae, Y., Dziubla, T.D., Scott, D.F., Hilt, J.Z., Yokel, R.A. Hyperthermia increase Fe_3O_4 nanoparticle flux across blood brain barrier cells. Presented at Markey Cancer Research Day, May 16, Lexington, KY, USA.

03/12 **Dan, M.**, Tseng, M.T., Wu, P., Unrine, J.M., Grulke, E.A., Yokel, R. A. Brain entry rate and capillary endothelial cell association of ceria engineered nanoparticles. Presented at the 51th Annual Meeting of the Society of Toxicology, March 11-15, San Francisco. Abstract Number/Poster Board number: 321 Poster Board -450

06/11 **Dan, M.**, Wu, P., Tseng, M.T., Graham, U.M., Florence, R.L., Unrine, J.M., Grulke, E.A., Yokel, R. A. Pharmacokinetics of ceria engineered nanomaterials after intravenous administration: effect of particle size. Presented at the 43th annual Pharmaceutics Graduate Student Research Meeting, June 23-25, Madison, Wisconsin.

06/11 Dan, M., Wu, P., Unrine, J.M., Grulke, E.A., Yokel, R. A. Ceria engineered nanoparticle association with the blood-brain barrier using in situ bran perfusion. Presented at a joint conference of the 13th International Neurotoxicology Association Meeting and the 11th International Symposium on Neurobehavioral Methods and Effects in Occupational and Environmental Health, June 5-10, Xi'an, China.

03/11 **Dan, M.**, Wu, P., Tseng, M.T., Graham, U.M., Florence, R.L., Unrine, J.M., Grulke, E.A., Yokel, R. A. Biodistribution and persistence of four sizes of ceria engineered nanomaterials after intravenous administration. Presented at the 50th Annual Meeting of the Society of Toxicology, March 6-10, Washington D.C. Abstract Number/Poster Board number: 2065 Poster Board -715.

03/10 **Dan, M.**, Tseng, M.T., Florence, R.L., Tiu, G., Unrine, J.M., Graham, U.M., Sultana, R., Hardas, S.S., Helm, M., Butterfield, D.A., Wu, P., Grulke, E.A., Yokel, R. A. Short- and long-term biodistribution and oxidative stress effects of a systemically-introduced 5 nm ceria engineered nanomaterial. Presented at the 49th Annual Meeting of the Society of Toxicology, March 7-11, Salt Lake City, UT.
Abstract Number/Poster Board number: 277 Poster Board -633

Mo Dan

Author's signature

06/14/2013

Date